

Mechanical losses in materials for future cryogenic gravitational wave detectors

Dissertation

**zur Erlangung des akademischen Grades
doctor rerum naturalium (Dr. rer. nat.)**

vorgelegt dem Rat der Physikalisch-Astronomischen Fakultät
der Friedrich-Schiller-Universität Jena

von Diplom-Physikerin Anja Schröter (geb. Zimmer)
geboren am 25. Juni 1976 in Berlin

1. Gutachter: Prof. Dr. Paul Seidel, Friedrich-Schiller-Universität Jena
2. Gutachter: Prof. Dr. Friedhelm Bechstedt, Friedrich-Schiller-Universität Jena
3. Gutachter: Prof. Dr. James Hough, University of Glasgow

Tag der letzten Rigorosumsprüfung: 24.01.2008

Tag der öffentlichen Verteidigung: 31.01.2008

Contents

Glossary	1
Introduction	3
1 The detection of gravitational waves	6
1.1 Gravitational waves and their sources	6
1.2 Types of gravitational wave detectors	6
1.3 Noise sources of interferometric gravitational wave detectors	9
1.3.1 Seismic noise	9
1.3.2 Photon shot noise	10
1.3.3 Thermal noise	10
2 Thermal noise	11
2.1 Fluctuation-Dissipation Theorem	11
2.2 Thermal noise of a single damped harmonic oscillator	12
2.3 Thermal noise of coupled damped harmonic oscillators	14
2.4 Direct method for calculation of thermal noise: Levin's approach	14
2.5 Thermoelastic noise	16
3 Mechanical losses	17
3.1 Elasticity, Anelasticity, and the Standard Anelastic Solid	17
3.1.1 Quasi-Static Response Functions	18
3.1.2 The primary dynamic response functions	20
3.1.3 Maxwell model	22
3.1.4 Kelvin-Voigt model	22
3.1.5 Standard Anelastic Solid	23
3.2 Anisotropic elasticity and anelasticity	27
3.2.1 Symmetrized stresses and strains	29
3.3 Internal losses in an 'ideal' solid	32

3.3.1	Thermoelastic losses	32
3.3.2	Losses due to interactions of phonons	33
3.4	Internal losses in a 'real' solid	37
3.4.1	Point defect related relaxations	37
3.5	Overview of external losses	45
3.6	Estimation of losses far below the resonant frequencies	46
4	Cryogenic Resonant Acoustic spectroscopy of bulk materials (CRA spectroscopy)	48
4.1	Overview of experimental setup and measuring principle	48
4.2	Parameters of the measuring system	54
5	Modelling of mechanical losses	55
5.1	Fused silica	55
5.2	Crystalline quartz	60
5.3	Crystalline calcium fluoride	73
5.4	Crystalline silicon	77
6	Impact of results on thermal noise reduction	85
7	Conclusions and further prospects	88
	Bibliography	92
	Zusammenfassung	I
	Appendix	V
	Acknowledgements	XIX
	Ehrenwörtliche Erklärung	XXI
	Lebenslauf	XXII

Glossary

α	thermal expansion coefficient
α_n	effective mass coefficient
β	half-width of the Gaussian distribution at the point where Ψ falls to $1/e$ of its maximum value
c	velocity of light
c_{ij}	components of second-order elastic stiffness constants tensor
C	specific heat capacity
C_p	mole fraction of defects in orientation p
Δ	relaxation strength
ϵ_{ij}	components of strain tensor
E	Young's modulus
E_a	activation energy
\mathcal{E}	energy density at maximum deformation
E_{max}	maximum strain energy
ESR	electron spin resonance
f	frequency
f_0	resonant frequency
ϕ	mechanical loss
FEA	finite element analysis
γ_k^j	Grüneisen number
\vec{G}	reciprocal lattice vector of the crystal
h	amplitude of a gravitational wave respectively relative strain
\hbar	Planck's constant divided by 2π
HO	harmonic oscillator
ICP-MS	Inductively Coupled Plasma Mass Spectrometry
ICP-OES	Inductively Coupled Plasma Optical Emission Spectrometry
IGWD	interferometric gravitational wave detector
IR	irreducible representation
J	modulus of compliance
J_R	relaxed compliance of elasticity
J_U	unrelaxed compliance of elasticity
k	spring constant
K	isothermal bulk modulus
k_B	Boltzmann constant
κ	thermal conductivity

L	arm length of an interferometer
λ	acoustic wave length
λ_{laser}	laser wave length
$\lambda_{ij}^{(p)}$	strain per mole fraction of defects that have the same orientation p
m	mass
M	modulus of elasticity
M_R	relaxed modulus of elasticity
M_U	unrelaxed modulus of elasticity
ν	Poisson's ratio
ν_{pq}	probability per second for a dipole to change from orientation p to q
N_p	number of defects in orientation p
n_t	number of indepdt λ tensors
P_{in}	laser input power
P_{diss}	average power dissipated in a test mass during one cycle under the action of an oscillatory pressure
Ψ	distribution function of relaxation times
Q	mechanical quality factor
Q_{bg}^{-1}	background loss
ρ	density of the material
r_0	radius of the laser beam spot where the intensity has decreased to $1/e$
s_{ij}	components of second-order elastic compliance constants tensor
S_x	power spectral density of the thermal displacement x
σ_{ij}	components of stress tensor
SAS	standard anelastic solid
T	temperature
τ	relaxation time
τ_0	relaxation constant, elementary reciprocal jump frequency
τ_d	ring-down time
Θ_D	Debye temperature
v_l	longitudinal phonon velocity
v_t	transverse phonon velocity
V	volume
V_0	molecular volume
x	displacement
Y	mechanical admittance

Introduction

The direct detection of gravitational waves is one of the biggest challenges to experimental sensitivity today. The prediction of perturbations of space-time propagating with the speed of light, called gravitational waves, by Albert Einstein [1] as a consequence of his general relativity theory has been confirmed only indirectly up to now. The energy loss of the binary pulsar PSR 1913+16 observed as a decreasing orbital period agreed with the calculated energy of an emission of gravitational waves giving an indirect evidence that gravitational waves do exist [2–4]. A direct evidence would not only be a confirmation of the existence of gravitational waves, but also of the theory of general relativity. However, even if this evidence is adduced a bundle of questions arises - questions about the properties and the origin of the universe. A new kind of astronomy based on gravitational waves could bring new insights additional to that gained by electromagnetic waves. Gravitational waves only weakly interact with matter and such could give unperturbed information. This advantage is on the other hand a handicap for their detection. Gravitational wave detectors have to be extremely sensitive. In the current configuration they are able to detect gravitational waves which would induce a relative length change of up to 10^{-22} on the earth [5]. As events producing such strong gravitational waves like black hole binary coalescence in the neighbourhood of the earth are very rare, the detection probability is also very low. To increase the probability and mainly to look deeper into the universe the sensitivity of the gravitational wave detectors has to be further enhanced. Today gravitational wave detectors based on two detection principles are operating: detectors working as resonant masses with resonant frequencies at most probable frequencies of gravitational waves and detectors designed as optical interferometers for observing the effective length changes induced by gravitational waves.

The focus of this work lies on detectors based on the interferometric detection principle which are able to detect gravitational waves in a broader frequency band of about 10 Hz to a few kHz [6]. Three main noise sources limit the sensitivity of these interferometric gravitational wave detectors (IGWDs). Besides seismic noise in the lower frequency region and photon shot noise in the upper range, the thermal noise of the optical components mirrors and beam splitter causes a loss in sensitivity in the mid-frequency range. The thermal noise can be mainly influenced by two physical values - temperature and mechanical loss of the solid at that temperature and given frequency. The current working IGWDs are operated at room temperature. Up to the beginning of this work, the reduction of thermal noise has been mainly tackled by

optimizing the mechanical losses respectively the mechanical quality factors of the optical components. Note, that the quality factors Q are the reciprocals of the losses at resonant frequencies. During the last years, the reduction of thermal noise by this method stagnated due to several reasons. One reason is that the mechanical loss of fused silica, the customarily used mirror substrate material, has been reduced by upgrading the purity of the material and enhancing the surface quality up to a point where its potential limit seems to be reached. At this point the second main parameter influencing the thermal noise gains importance - the temperature. The whole thermal noise level could be lowered by withdrawing thermal energy by cooling the optical components. First steps have been taken in this direction. A prototype of a cryogenic interferometric gravitational wave detector is the CLIO [7] in Japan. As mechanical losses are in general dependent on temperature, materials with low losses at cryogenic temperatures are required for these future detectors. At the beginning of this work first considerations have been taken concerning the material selection. Measurements, however, were very rare.

In 2003 we started with the study of mechanical losses of potential materials for cryogenic IGWDs within our project 'Cryogenic Q -factor measurements of interferometer components' (subproject C4 of the SFB / Transregio 7 'Gravitational Wave Astronomy'). The understanding of the loss processes in the materials is essential for an effective and controlled lowering of the thermal noise. This requires systematic loss measurements and their interpretation. The extensive and complex task demanded the close collaboration of the involved researchers. The focus of the work of Ronny Nawrodt [8] was to establish and characterize a high sensitivity measuring system for materials with high mechanical quality factors. With this new method of mechanical spectroscopy, cryogenic resonant acoustic (CRA) spectroscopy of bulk materials, Q factors can be determined in the temperature range from 5 K to 325 K.

The main aim of my work and hence of this thesis was to analyze the measured data and to acquire a description of mechanical losses in solids for the modelling and interpretation of our experimental results. Based on the gained insights an advice concerning the material selection and operating temperature for future cryogenic IGWDs should be given.

The thesis is structured as follows. The first chapter gives an introduction into the field of gravitational wave detection. The main noise sources of IGWDs are described. Details on thermal noise, types of thermal noise, how to calculate it and its relation to mechanical losses in solids are given in chapter two. A main part of the thesis is the description of mechanical losses in solids in the third chapter. In chapter four an approach for the extrapolation of the mechanical losses to the IGWD detection frequency band from the systematic Q measurements is presented. Further, our method

of mechanical spectroscopy, CRA spectroscopy, is introduced, including parameters of the high precision experimental setup. Chapter five is again a main part of the thesis. The acquired insights on mechanical losses in solids are applied to the measured data on different materials. Statements on the selection of material and operating temperature regarding the reduction of thermal noise in future cryogenic IGWDs are made in chapter six. Finally, chapter 7 gives the conclusions and further prospects gained from this work.

1 The detection of gravitational waves

1.1 Gravitational waves and their sources

One of the most challenging questions for human beings is exploring the origin and properties of the universe. Electromagnetic radiation is used to gain information from astronomical distances in many space observatories all over the world. A further kind of waves - gravitational waves - could give new insight into the universe, for instance exploring the nature of the dark matter.

They have been predicted by Einstein according to the General Theory of Relativity [1]. He proposed them to be of quadrupole origin, travelling with the speed of light. Gravitational waves merely weakly interact with matter. On the one hand this property makes them interesting for astronomy, giving unperturbed information, even back to the Big Bang. On the other hand it implies severe difficulties in detection. The amplitudes of gravitational waves even generated by masses of astronomical dimensions are very small. The estimated strength of the signal on the earth, which corresponds to a relative length change, even for the nearest heavy events (supernova in the Milky Way) is about 10^{-19} [9]. Neighbour galaxies (Virgo cluster) are expected to produce signal strengths of 10^{-21} to 10^{-20} for neutron stars or black holes during gravitational collapse [10]. Other sources of gravitational waves are the coalescence of compact binaries (consisting of neutron stars and black holes), an instability-driven spin-down of neutron stars, accreting neutron stars, lumpy pulsars, and events in the early universe forming a stochastic background of gravitational waves [10, 11].

In spite of their tiny effect, an indirect evidence of the existence of gravitational waves has been given by Hulse and Taylor in observing the binary pulsar PSR 1913+16 [2, 3]. The energy loss detected in form of the decrease of the orbital period agreed very well with that predicted to be due to the emission of gravitational waves [4]. Thus, the indirect evidence was possible due to an accumulation of the gravitational waves' effects over time.

The direct detection of gravitational waves still is an ongoing challenge.

1.2 Types of gravitational wave detectors

On earth, two types of gravitational wave detectors are used: resonant mass detectors and interferometric ones. In the 1960s Weber started his pioneering work in

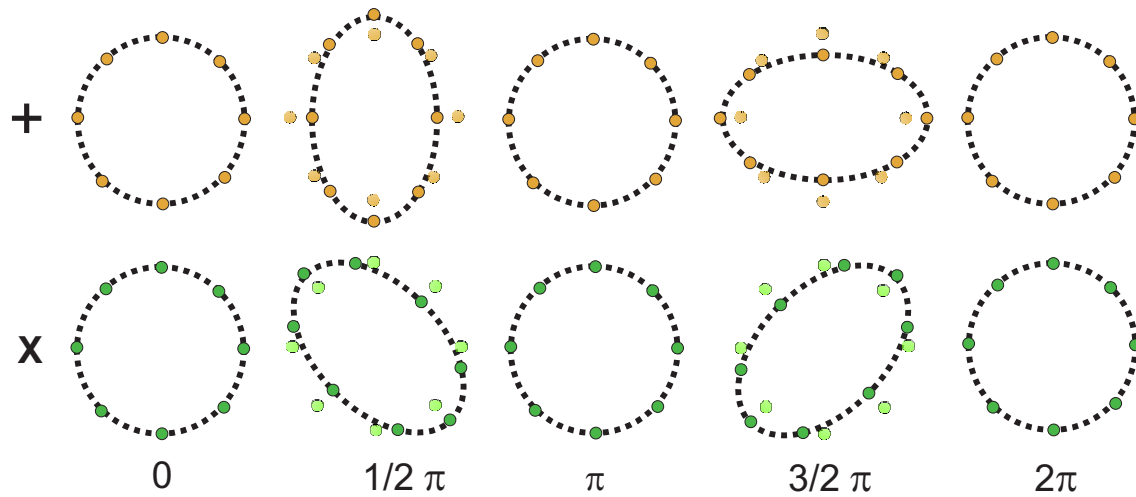


Fig. 1.1: The effect of the two polarization states (+ and x) of a gravitational wave on a ring of free test masses. The propagation direction of the wave is perpendicular to the page.

constructing and operating resonant bar detectors at room temperature [12]. These were huge aluminium cylinders with resonances at about 1.6 kHz. Expected passing gravitational waves of the same frequency should excite them to resonant vibrations. In 1968 Weber started to report coincidences between different detectors thought to be caused by gravitational waves [13, 14]. His results were doubted due to the facts that they could not be reproduced by similar setups of other groups and that the sensitivity of the initial detectors of the order of 10^{-15} over millisecond timescales was far lower than that needed to observe the expected strongest signal strengths of gravitational waves [6]. In the following years several improved resonant mass detectors have been built [15, 16], in cylindrical as well as in spherical form, e. g., ALLEGRO [17], AURIGA [18], EXPLORER [19], MiniGRAIL [20], NAUTILUS [21], and NIOBE [22]. One enhancement consists in the cooling of the detectors reducing their thermal noise (for details on thermal noise see subsection 1.3.3 and chapter 2). However, the disadvantage of a very narrow detection band still remains. An extension of the frequency range to at least 1 kHz to 4 kHz could be achieved by a new concept, the Dual mass detector [23].

For a broad frequency band detection a second principle of detection is applied. Interferometers are able to detect changes in their arm lengths with high sensitivity. The influence of an arriving gravitational wave on the interferometer is demonstrated on the example of a ring of freely falling test masses in space shown in Fig. 1.1. The ring is deformed according to the two possible gravitational wave polarisations which are turned 45° to one another. Two of the test masses can be thought of as the end mirrors of the interferometer with the beam splitter in the centre. An arriving gravitational wave of amplitude h has the effect of a change of the interferometer arm lengths L of

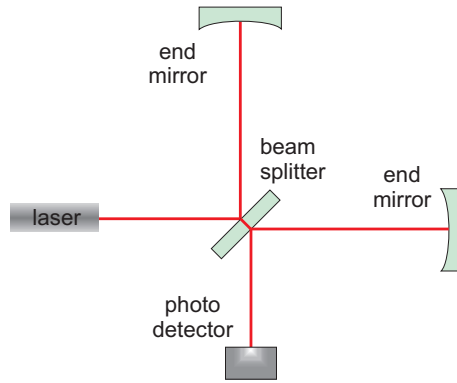


Fig. 1.2: Schematic of a gravitational wave detector based on a Michelson interferometer.

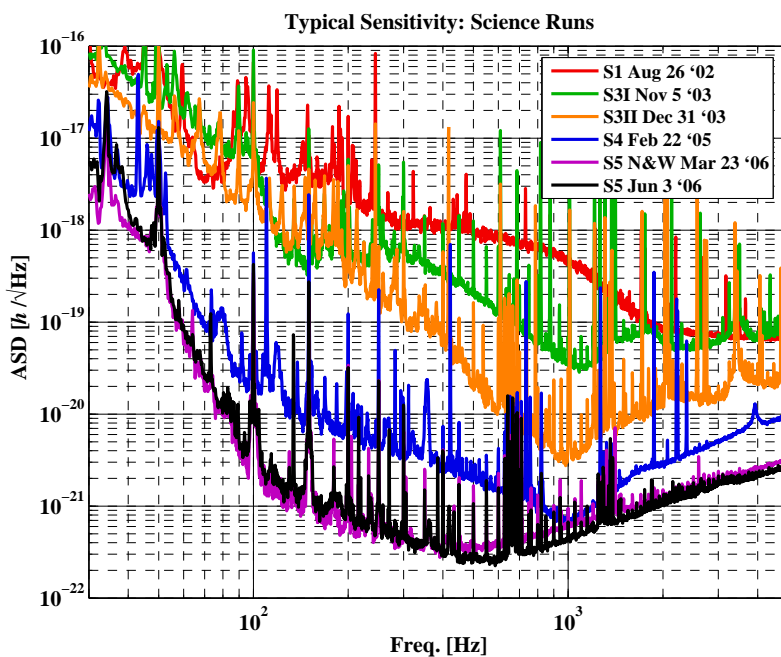


Fig. 1.3: Improvement of typical sensitivity of GEO600 during science runs [28].

ΔL for each arm, but in the opposite direction (Fig. 1.1). Thus the total relative strain is

$$h = \frac{2 \Delta L}{L}. \quad (1.1)$$

A schematic of an interferometer based on a Michelson design is shown in Fig. 1.2. Currently working interferometric gravitational wave detectors (IGWDs) on earth are GEO600 [24], LIGO [25], TAMA300 [26] and VIRGO [27]. Their detection frequency band spans from about 10 Hz to a few kHz. Exemplarily, the improvement of the sensitivity of GEO600 is shown in Fig. 1.3. A comparison with Fig. 1.4 reveals that GEO600 has nearly reached its design sensitivity limit. The 'Large Scale Cryogenic Gravitational Wave Telescope' (LCGT) is the future project of a Japanese gravitational wave group. A cryogenic prototype, CLIO [7], has been already built. In space, a detector working also based on the interferometric principle is planned - LISA [29].

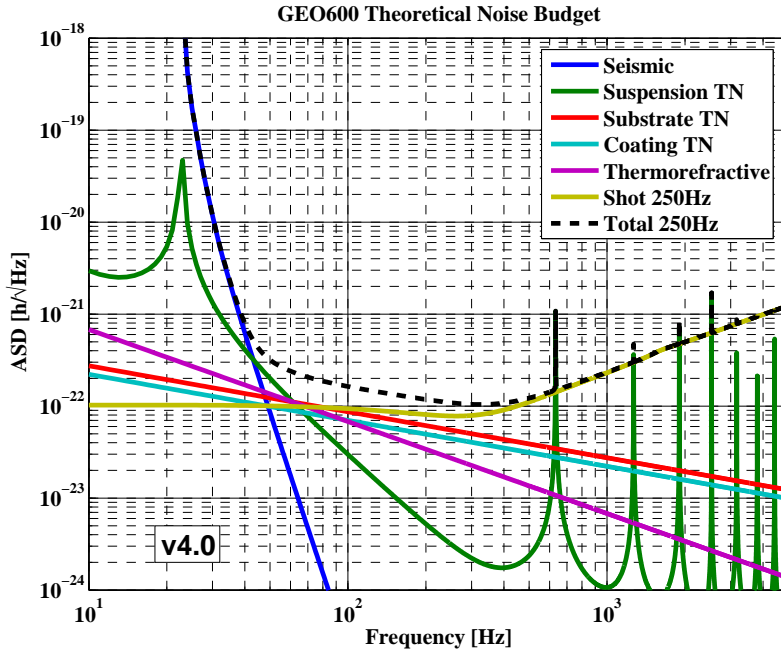


Fig. 1.4: GEO600 theoretical noise budget in current configuration for 250 Hz signal detuning [28].

One of its advantages compared to the ground-based detectors is the absence of seismic noise which permits the detection of gravitational waves of low frequency. This work will further focus on the improvement of interferometric detectors.

1.3 Noise sources of interferometric gravitational wave detectors

An overview of main noise sources in ground-based IGWDs is given in the following. Fig. 1.4 shows the different contributions using the example of GEO600.

1.3.1 Seismic noise

The main noise source in the low frequency range of the gravitational wave detection band - currently setting a lower limit to about 10 Hz - is of seismic nature. Its origin are manifold processes caused by civilisation (e.g., traffic) as well as nature (e.g., movements of the earth and of water in oceans). Choosing a quiet place for the detector is one measure to reduce the seismic noise. In the detector itself the test masses have to be isolated from the environment. In GEO600 this is, for instance, achieved by using triple pendulums with very low resonant frequencies.

1.3.2 Photon shot noise

In the upper range of the detection band photon shot noise dominates. Statistical fluctuations in the number of photons detected at the output of the interferometer are not distinguishable from a length change due to a gravitational wave. A reduction of the shot noise is gained by improving the input power P of the laser according to [30]

$$\text{detectable strain} / \sqrt{\text{Hz}} \quad h_{ps\text{ noise}} = \frac{1}{L} \sqrt{\frac{\lambda_{laser} \hbar c}{2\pi P_{in}}}, \quad (1.2)$$

where λ_{laser} is the wave length of the laser with input power P_{in} , \hbar is Planck's constant divided by 2π , and c the velocity of light.

Assuming the current used laser wave length of 1064 nm and an interferometer arm length of 1 km, an input power of 5 kW is required in order to reach a sensitivity of $10^{-21} / \sqrt{\text{Hz}}$.

1.3.3 Thermal noise

Between the dominating contributions of seismic and photon shot noise the detection sensitivity is limited by thermal noise. Different types of thermal noise can be distinguished:

- Thermorefractive noise: The refraction indices of the mirror coatings are changed by thermal fluctuations, resulting in phase noise of the laser beam.
- Thermoelastic noise: Statistical fluctuations of the temperature are transformed by the thermal expansion into mechanical motion.
- Brownian noise: The system contains $\frac{1}{2}k_B T$ (k_B : Boltzmann constant) thermal energy per degree of freedom at a given temperature T according to the Equipartition Theorem. This results in fluctuations of the surfaces of the test masses and suspensions.

The mechanical motion of the system test mass and suspension leads to a change of the arm lengths of the interferometer and therefore cannot be distinguished from a gravitational wave signal. In the following chapters of this work the focus lies on the analysis of this main noise source in the mid-frequency region of the interferometric detectors to present well-directed methods to significantly reduce it.

2 Thermal noise

In the following the expression 'thermal noise' is used for the Brownian part unless otherwise stated.

In a mechanical system, like the system mirror plus suspension, the Equipartition Theorem predicts a mean value of $\frac{1}{2}k_B T$ thermal energy stored in each degree of freedom. Degrees of freedom are translatory and rotatory motions of the atoms in the system. Thus, it is clear that the thermal noise of the test masses can be influenced by temperature. Another important parameter of thermal noise is the mechanical loss of the system at the particular temperature and frequency. The aim of the present work is a systematic analysis of the mechanical losses of the materials of the optical components since it is essential for a directed reduction of thermal noise besides a sufficient lowering of suspension losses. In this chapter possible ways of calculating thermal noise are derived. At first the relation of thermal noise and mechanical losses by the Fluctuation-Dissipation Theorem is elucidated.

2.1 Fluctuation-Dissipation Theorem

The Fluctuation-Dissipation Theorem (FDT) describes the relation between the noise (fluctuations) in a system and its energy losses (dissipation) [31, 32]. It is general in nature and can be applied to different kinds of systems (electronic system: Johnson–Nyquist noise). For a mechanical system the power spectral density of the thermal displacement x at a temperature T and frequency f - simply called *thermal noise* - is given by

$$S_x(f) = \frac{4k_B T}{(2\pi f)^2} \Re [Y(f)] \quad \text{in } m^2/Hz. \quad (2.1)$$

$\Re [Y(f)]$ is the real part of the mechanical admittance. In the IGWDs only the thermal displacement of the optical components in direction of the interferometer arm is relevant for thermal noise. Therefore, the problem is treated in one dimension and in the following, all vectorial quantities are represented by their components in direction of the interferometer arm unless not otherwise stated.

In the frequency domain the admittance of a mechanical system gives the resulting velocity v after applying a force F

$$Y(f)F(f) = v(f). \quad (2.2)$$

Hence, to gain the admittance for the calculation of thermal noise the force and velocity of the mirrors in the frequency domain are required. An approach to model the thermal noise of the mirrors in direction of the interferometer arms is to describe them as coupled one-dimensional harmonic oscillators (HO).

2.2 Thermal noise of a single damped harmonic oscillator

Starting with *one* one-dimensional HO with spring constant k , the spring experiences in the dissipationless (elastic) case a restoring force according to Hooke's Law

$$F_{spr}^{el} = -k x. \quad (2.3)$$

A dissipating (anelastic) and therefore damped HO possesses an additional imaginary term of the spring constant

$$F_{spr}^{anel} = -k [1 + i \tan(\phi(f))] x. \quad (2.4)$$

ϕ is the mechanical loss angle or factor and represents the phase shift between the applied force and the displacement x of the system. In general, ϕ depends on frequency as well as temperature. Since merely materials with low losses are considered, ϕ is small ($\phi \ll 1$). Therefore the tangent of the loss angle can be approximated by the angle itself.

$$F_{spr}^{anel} = -k [1 + i \phi(f)] x. \quad (2.5)$$

The equation of motion of a HO of mass m with internal friction is then

$$F(f) = -m(2\pi f)^2 x(f) + k [1 + i \phi(f)] x(f). \quad (2.6)$$

$F(f)$ is the internal thermal force. $x(f)$ is substituted by $v(f)/(i 2\pi f)$, assuming $x(f) \propto \exp(i 2\pi f t)$

$$F(f) = (i 2\pi f m - i k/(2\pi f) [1 + i \phi(f)]) v(f). \quad (2.7)$$

With equation (2.2) the following relation is derived

$$Y(f) = \frac{v(f)}{(i 2\pi f m - i k/(2\pi f) [1 + i \phi(f)]) v(f)} \quad (2.8)$$

$$= \frac{\frac{k}{2\pi f} \phi(f) - i(2\pi f m - \frac{k}{2\pi f})}{(\frac{k}{2\pi f} \phi(f))^2 + (2\pi f m - \frac{k}{2\pi f})^2}. \quad (2.9)$$

Using the substitution $k = m(2\pi f_0)^2$, the admittance is given by

$$Y(f) = \frac{\frac{m(2\pi f_0)^2}{2\pi f} \phi(f) - i(2\pi f m - \frac{m(2\pi f_0)^2}{2\pi f})}{(\frac{m(2\pi f_0)^2}{2\pi f} \phi(f))^2 + (2\pi f m - \frac{m(2\pi f_0)^2}{2\pi f})^2}. \quad (2.10)$$

Inserting Eq. (2.10) into the FDT Eq. (2.1) yields

$$S_x(f) = \frac{4k_B T}{(2\pi f)^2} \frac{\frac{m(2\pi f_0)^2}{2\pi f} \phi(f)}{(\frac{m(2\pi f_0)^2}{2\pi f} \phi(f))^2 + (2\pi f m - \frac{m(2\pi f_0)^2}{2\pi f})^2} \quad (2.11)$$

$$= \frac{4k_B T}{(2\pi)^3 f m} \frac{\phi(f) f_0^2}{[(\phi(f))^2 f_0^4 + (f_0^2 - f^2)^2]}. \quad (2.12)$$

In this context, $\phi(f)$ is the frequency dependent loss at a given temperature T . The expression for the thermal noise of a one-dimensional damped HO is simplified for the frequency range above the resonance, the resonance itself, and the range below resonance.

For $f \gg f_0$ and $\phi(f) \ll 1$ the thermal noise is proportional to ϕ

$$S_x(f) \approx \frac{4k_B T f_0^2}{(2\pi)^3 m} \frac{\phi(f)}{f^5}. \quad (2.13)$$

At the resonance, $f = f_0$ and $\phi(f_0) \ll 1$, the power spectral density of the thermal displacement is inversely proportional to the mechanical loss

$$S_x(f) \approx \frac{4k_B T}{(2\pi)^3 m f_0^3} \frac{1}{\phi(f_0)}. \quad (2.14)$$

In the frequency range below resonance, $f \ll f_0$ and $\phi(f) \ll 1$, the thermal noise is proportional to the mechanical losses

$$S_x(f) \approx \frac{4k_B T}{(2\pi)^3 m f_0^2} \frac{\phi(f)}{f}. \quad (2.15)$$

Thus, it is obvious that a thermal noise reduction in the detection frequency band of the IGWDs, which is located below the resonances of the mirrors, can be achieved by a reduction of mechanical losses at that frequencies. A further lowering can be attained by cooling apart from increasing the resonant frequency. Since mechanical losses are in general dependent on frequency and temperature, materials with low

mechanical losses at cryogenic temperatures are required.

2.3 Thermal noise of coupled damped harmonic oscillators

The mirrors can be modelled by coupled damped harmonic oscillators. In fact, for homogeneous losses the response of the system can be modeled as a superposition of normal modes. To gain the thermal noise in the region below the resonances of the mirrors the contributions due to the existence of n modes are summed up

$$S_x(f) = \sum_n \frac{4k_B T \phi_n(f)}{(2\pi)^3 \alpha_n m f_n^2 f}. \quad (2.16)$$

ϕ_n is the loss factor associated with the n^{th} internal mode at temperature T . $\alpha_n m$ is the effective mass of the same mode. α_n specifies the coupling between the mechanical mode and the optical mode of the laser. It depends on the mass of the mirror, the resonant frequency f_n and the laser beam width [33, 34]. This method reaches its limit when dealing with inhomogeneously distributed losses, e. g. for the composite mirrors, consisting of a substrate and thin optical layers. Then, the modes are correlated and the sum is not correct. A mirror consists of a substrate and an optical coating consisting of different materials. Therefore, inhomogeneous losses apparently occur. A direct calculation of the thermal noise offers a way out of this problem. One method is that of Levin [35] which is discussed in the following section.

2.4 Direct method for calculation of thermal noise: Levin's approach

In Levin's approach [35] a time varying force with absolute value $F(t)$ is applied on the test mass' surface. The resulting pressure possesses a spatial profile $f(\vec{r})$, depending on the position vectors of the surface \vec{r} with origin of the coordinate system in the centre of the circular area

$$p(\vec{r}, t) = F(t) f(\vec{r}). \quad (2.17)$$

Note, that the profile is that of the laser beam of the interferometric detector. Currently, Gaussian profiles are used

$$f(\vec{r}) = \frac{\exp(-r^2/r_0^2)}{\pi r_0^2}, \quad (2.18)$$

where r_0 is the radius of the laser beam spot where the intensity has decreased to $1/e$.
With a cosinusoidal varying force

$$F(t) = F_0 \cos(2\pi t) \quad (2.19)$$

with amplitude F_0 , the real part of the admittance is

$$\Re [Y(f)] = \frac{2P_{diss}}{F_0^2}, \quad (2.20)$$

where P_{diss} is the average power dissipated in the test mass during one cycle under the action of the oscillatory pressure [35].

Applying the FDT (Eq. (2.1)) the thermal noise is

$$S_x(f) = \frac{2k_B T P_{diss}}{\pi^2 f^2 F_0^2}. \quad (2.21)$$

For parts of the test masses with homogeneous dissipation P_{diss} can be calculated by

$$P_{diss} = 2\pi f E_{max} \phi(f, T) \quad (2.22)$$

using the particular loss factor and the maximum strain energy E_{max} in the considered volume. E_{max} can be numerously calculated using the finite element analysis (FEA) based software ANSYS [36]. The contributions of different parts with homogeneous losses of the inhomogeneous solid - like substrate and coating of a mirror - may then be simply summed up. This method almost corresponds to the integration over the volume V of the test mass

$$P_{diss} = 2\pi f \int_V \mathfrak{E}(\vec{r}) \phi(\vec{r}, f, T) dV, \quad (2.23)$$

where \mathfrak{E} is the energy density at maximum deformation. However, possible losses at the interfaces of different materials are not included. A far more important remaining problem is the determination of the mechanical loss factor of the test masses in the detection frequency band of the IGWDS at cryogenic temperatures. Therefore, the main part of this thesis treats the modelling of mechanical losses in chapter 3 and its application to several low-loss materials in chapter 5.

2.5 Thermoelastic noise

Besides Brownian thermal noise another kind of thermal noise, thermoelastic noise, is present in the test masses of the IGWDs. Local thermal fluctuations in a solid which are permanently present lead to mechanical fluctuations (changes of the volume) mediated by the thermal expansion coefficient α . The so induced motion of the mirror surfaces and suspensions causes a length change of the interferometer arms and thus simulates a gravitational wave signal. Thermoelastic losses do not occur for pure shear waves, since there is no change in volume. Braginsky et al. [37] calculated the thermoelastic noise of an infinite test mass in the adiabatic limit under assumption of a Gaussian laser beam with a diameter small compared to the diameter of the mirror for an isotropic material

$$S_x(f) = \frac{\sqrt{2} k_B T^2 \alpha^2 (1 + \nu)^2 \kappa}{\pi^{5/2} \rho^2 C^2 r_0^3 f^2}, \quad (2.24)$$

where ν is Poisson's ratio, κ is the thermal conductivity, ρ is the density, and C is the specific heat capacity. Later Liu and Thorne introduced a correction factor for a finite test mass [38]. In general, i. e., for anisotropic solids the thermoelastic noise at all frequencies can be calculated using Levin's approach (section 2.4). The required thermoelastic losses are yielded by solving the stress equation of motion and the heat flow conservation equation, coupled by the thermoelastic constitutive equations, using ANSYS [39].

A reduction of thermoelastic noise in the IGWDs is aimed for by using other than Gaussian laser profiles [40–43].

3 Mechanical losses

As has been seen in chapter 2, besides cooling the mirrors of the IGWDs, a systematic analysis of their mechanical losses is essential for a directed reduction of thermal noise in the detection frequency range. This thesis focuses on the mechanical losses in potential low-loss materials for mirror substrates. The results of the measurements of these losses, using the experimental method described in chapter 4, require a suitable interpretation. The total measured losses are a superposition of external and internal losses. Both consist of contributions due to different loss processes. The aim of the present chapter is to acquire mechanical loss models specific for the description of the losses. The loss data measured are then analysed with these models in chapter 5. Materials under consideration, like crystalline quartz, calcium fluoride, and silicon, belong to the trigonal and cubic crystal systems. Therefore, the examples given are restricted to these two crystal systems.

3.1 Elasticity, Anelasticity, and the Standard Anelastic Solid

The following description of elasticity, anelasticity, and the Standard Anelastic Solid (SAS) follows that given by Nowick and Berry [44].

On the way to a description of anelasticity, it is convenient to start with the behaviour of an *ideal elastic solid*. At first, only simple modes of deformation, such as pure shear, uniaxial deformation, and hydrostatic deformation, are considered to ease comprehension. Therefore, the second-order tensors stress, represented by the matrix (σ_{ij}) , and strain, represented by (ϵ_{ij}) , are substituted by the scalars σ , and ϵ . Hooke's law gives their relation

$$\sigma = M \epsilon, \quad (3.1)$$

$$\text{respectively } \epsilon = J \sigma, \quad (3.2)$$

$$\text{with } M = 1/J, \quad (3.3)$$

where M is the modulus of elasticity (often and also here called the modulus) and its reciprocal J is named the modulus of compliance (or simply compliance). The moduli corresponding to the mentioned simple modes of deformation are the shear modulus, Young's modulus, or the bulk modulus, respectively. In general, especially concerning

	Linear	Unique equilibrium relationship (complete recoverability)	Instantaneous
Ideal elasticity	Yes	Yes	Yes
Nonlinear elasticity	No	Yes	Yes
Instantaneous plasticity	No	No	Yes
Linear viscoelasticity	Yes	No	No
Anelasticity	Yes	Yes	No

Tab. 3.1: Different types of mechanical behaviour.

anisotropic materials, the second-order tensors stress and strain are related by the elastic stiffness constants (c_{ijkl}), respectively the elastic compliance constants (s_{ijkl}), which are fourth-order tensors. A detailed description is given in section 3.2.

The ideal elastic behaviour described by Eqs. (3.2) and (3.3) is defined by three conditions

- the response is linear,
- a unique equilibrium value exists for each strain response corresponding to a particular level of applied stress (or vice versa) which implies a complete recoverability of the response upon release of the applied stress or strain,
- this equilibrium response is achieved instantaneously.

Depending on which of (or combinations of) the conditions listed above are kept, different mechanical behaviours emerge, arranged in Tab. 3.1. Thus, the difference from ideal elasticity to anelasticity is that for anelasticity the equilibrium response is achieved after the passage of sufficient time. This process of reaching a new equilibrium is termed anelastic relaxation and the time needed, relaxation time. Note, that anelasticity indeed includes a partly instantaneous response. Only a fraction of the response is nonelastic.

3.1.1 Quasi-Static Response Functions

An experiment in which either an applied stress or strain is held constant for any desired period of time is termed quasi-static. Under such conditions, anelastic materials exhibit phenomena of creep, the elastic aftereffect, and stress relaxation.

3.1.1.1 Creep and elastic aftereffect

In the creep experiment, a stress σ_0 is applied abruptly to the sample and held constant, while the strain ϵ is observed as a function of time (Fig. 3.1). From the re-

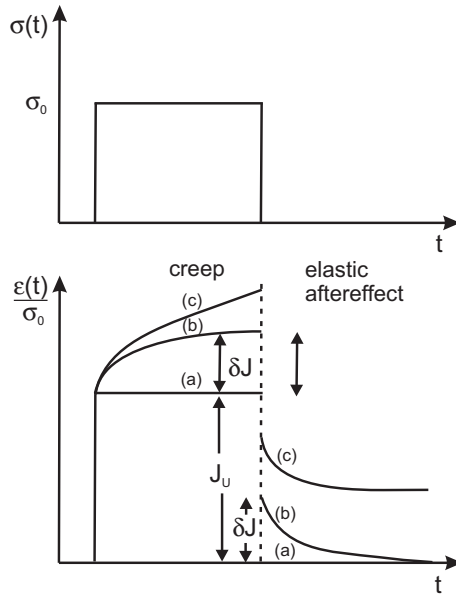


Fig. 3.1: Creep and elastic aftereffect for (a) ideal elastic solid, (b) anelastic solid, and (c) linear viscoelastic solid.

quirement of linearity, it is clear that $\epsilon(t)/\sigma_0$ is independent of σ_0 . Accordingly, the response function is

$$J(t) = \epsilon(t)/\sigma_0, \quad t \geq 0. \quad (3.4)$$

$J_U \equiv J(0)$ is called the unrelaxed compliance. The equilibrium value of $J(t)$ is called the relaxed compliance $J_R \equiv J(\infty)$. The difference between the relaxed and the unrelaxed compliance is the relaxation of the compliance $\delta J \equiv J_R - J_U$. If the stress σ_0 is abruptly released after a creep experiment, the instantaneous (elastic) response is in general followed by a time dependent decay of strain (Fig. 3.1). This effect is called the 'elastic aftereffect' or 'creep recovery'.

3.1.1.2 Stress relaxation

In a stress relaxation experiment, a constant strain ϵ_0 is imposed on the solid, while the stress σ is observed as a function of time. The stress relaxation function is given by

$$M(t) = \sigma(t)/\epsilon_0, \quad t \geq 0. \quad (3.5)$$

By analogy to the case of creep, $M_U \equiv M(0)$ is the unrelaxed modulus, $M_R \equiv M(\infty)$ is the relaxed modulus, and $\delta M \equiv M_U - M_R$ is the relaxation of the modulus. From the existence of a unique equilibrium relation between stress and strain, it follows that the relaxed modulus is the reciprocal of the relaxed compliance

$$M_R = 1/J_R. \quad (3.6)$$

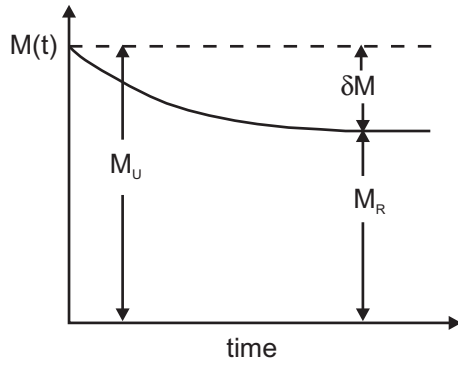


Fig. 3.2: Stress relaxation of an anelastic solid.

The unrelaxed modulus and compliance are also reciprocals of each other as on a short time scale, the material behaves as if it were ideally elastic and therefore Eqs. (3.2) and (3.3) apply with constants M_U and J_U

$$M_U = 1/J_U. \quad (3.7)$$

It should be noted that δM is not the reciprocal of δJ . In fact,

$$\delta M = \delta J / (J_U J_R). \quad (3.8)$$

The relaxation strength is a dimensionless quantity defined by

$$\Delta \equiv \delta M / M_R = \delta J / J_U. \quad (3.9)$$

3.1.2 The primary dynamic response functions

Dynamic experiments are appropriate to gain information about the anelastic behaviour of the material at much shorter time scales. A stress (or strain) periodic in time is applied to the system to determine the phase lag of the strain behind the stress (or vice versa). In the complex notation, which is most convenient for describing periodic processes, the stress is given by

$$\sigma = \sigma_0 \exp(i 2\pi f t), \quad (3.10)$$

where σ_0 is the stress amplitude and f the vibration frequency. Due to the linearity of the stress-strain relation, the strain with strain amplitude ϵ_0 is periodic with the same frequency, but lags behind the stress by the loss angle ϕ

$$\epsilon = \epsilon_0 \exp(i [2\pi f t - \phi]), \quad (3.11)$$

The ratio ϵ/σ is a complex quantity, called complex compliance

$$J^*(f) \equiv \epsilon/\sigma = |J|(f) \exp(-i\phi(f)), \quad (3.12)$$

with the absolute dynamic compliance

$$|J|(f) = \epsilon_0/\sigma_0. \quad (3.13)$$

An alternative description is to write the strain in the form

$$\epsilon = (\epsilon_1 - i\epsilon_2) \exp(-i2\pi f t), \quad (3.14)$$

where ϵ_1 is the amplitude of the component of ϵ in phase with the stress and ϵ_2 the amplitude of the component which is 90° out of phase. Dividing Eq. 3.14 through σ results in

$$J^*(f) = J_1(f) - iJ_2(f), \quad (3.15)$$

where $J_1 \equiv \epsilon_1/\sigma_0$ is the real part (the 'storage compliance') and $J_2 \equiv \epsilon_2/\sigma_0$ the imaginary part (the 'loss compliance'). The response functions are linked by the following relations

$$|J|^2 = J_1^2 + J_2^2 \quad (3.16)$$

$$\tan(\phi) = J_2/J_1 \quad (3.17)$$

Relations for the complex modulus $M^*(f)$ are gained by substituting 'J' by 'M'.

The energy stored E_{max} and the energy dissipated during a cycle of vibration ΔE can now be calculated by using the storage compliance, respectively modulus, and the loss compliance, respectively modulus.

$$E_{max} = \int_{2\pi f t=0}^{\pi/2} \sigma d\epsilon = \frac{1}{2} J_1 \sigma_0^2 = \frac{1}{2} M_1 \epsilon_0^2 \quad (3.18)$$

$$\Delta E = \oint \sigma d\epsilon = \pi J_2 \sigma_0^2 = \pi M_2 \epsilon_0^2 \quad (3.19)$$

The ratio of dissipated to stored energy is related to the loss angle ϕ by

$$\Delta E/E_{max} = 2\pi J_2/J_1 = 2\pi M_2/M_1 = 2\pi \tan(\phi) \quad (3.20)$$

At this point, the 'superposition principle' of Boltzmann should be noted: If a series of stresses are applied to a material at different times, each contributes to the deforma-

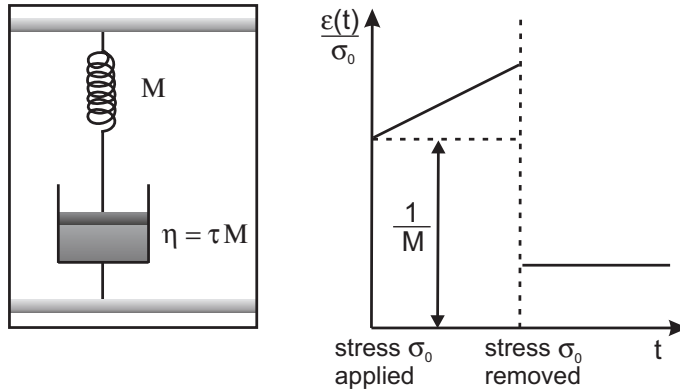


Fig. 3.3: Left: Maxwell model; right: behaviour of the Maxwell model on loading and unloading.

tion as if it alone was acting. Thus, different loss effects merely sum up.

3.1.3 Maxwell model

The Maxwell model consists of a spring, represented by a modulus M , and a dashpot with viscosity $\eta = M\tau$ connected in series (Fig. 3.3). The response to a sudden applied stress is an instantaneous strain of the spring, followed by linear viscous creep of the dashpot. The application of a constant strain gives rise to an instantaneous stress in the spring since the dashpot does not react immediately. Continuously, the stress decreases until zero as the dashpot proceeds to flow. Thus, the Maxwell model is capable of describing complete stress relaxation.

In a series combination of two elements, 1 (spring) and 2 (dashpot), the stresses σ_1 and σ_2 are equal while the strains ϵ_1 and ϵ_2 are additive. The stress and the total strain are thus given by

$$\sigma = \sigma_1 = \sigma_2, \quad \epsilon = \epsilon_1 + \epsilon_2. \quad (3.21)$$

With $\sigma_1 = M\epsilon_1$ and $\sigma_2 = M\tau\dot{\epsilon}_2$ the appropriate stress-strain equation is

$$\tau\dot{\sigma} + \sigma = \tau M\dot{\epsilon}. \quad (3.22)$$

The Maxwell model is not suitable for the description of an anelastic material, since it displays steady viscous creep, rather than the recoverable creep characteristic of anelasticity. A model which possesses this property is the Kelvin-Voigt model.

3.1.4 Kelvin-Voigt model

The Kelvin-Voigt model describes the behaviour of spring and dashpot connected in parallel (Fig. 3.4). Here, it is convenient to represent the spring by its compliance J while the viscosity of the dashpot is $\eta = \tau/J$. A stress applied has to be first entirely sustained by the dashpot as it reacts only continuously with time. During its flow, the

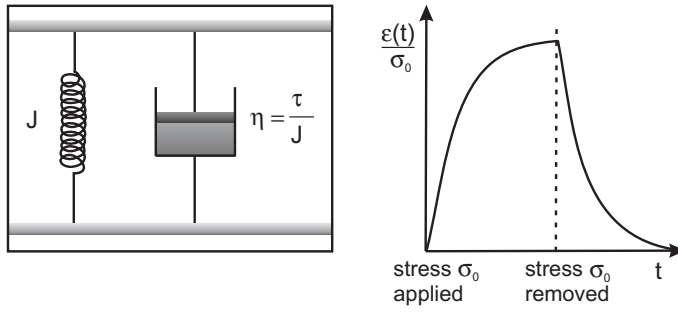


Fig. 3.4: Left: Kelvin-Voigt model; right: behaviour of the Kelvin-Voigt model on loading and unloading.

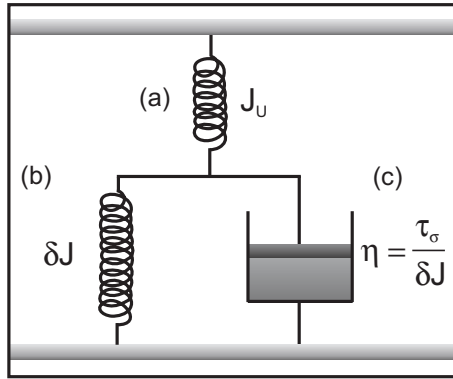


Fig. 3.5: Standard Anelastic Solid containing a Kelvin-Voigt unit.

stress is transferred to the spring. If the stress is completely sustained by the spring, the dashpot ceases to flow. Upon release of the stress, the spring remains extended until the dashpot has crept back to its initial position.

In a parallel combination of two elements, 1 (spring) and 2 (dashpot), the strains ϵ_1 and ϵ_2 are equal, while the stresses σ_1 and σ_2 are additive. The strain and total stress are thus given by

$$\epsilon = \epsilon_1 = \epsilon_2, \quad \sigma = \sigma_1 + \sigma_2. \quad (3.23)$$

Using $\epsilon_1 = J \sigma_1$ for the spring and $\dot{\epsilon}_2 = J \sigma_2 / \tau$ for the dashpot, the stress-strain relationship is described by

$$J \sigma = \epsilon + \tau \dot{\epsilon}. \quad (3.24)$$

Since the Kelvin-Voigt model does not allow for an instantaneous deformation, the elastic part of anelasticity lacks. As this property was correctly given by the Maxwell model, a combination of these two models could allow an appropriate description of anelasticity.

3.1.5 Standard Anelastic Solid

Depending on which model is chosen as the basis for the description of anelasticity, the Kelvin-Voigt or the Maxwell model, one of two equivalent models for the Standard Anelastic Solid (SAS) is achieved (Figs. 3.5 and 3.6). Starting with a Kelvin-Voigt unit (see subsection 3.1.4) a spring has to be attached in series to adjust the lack of

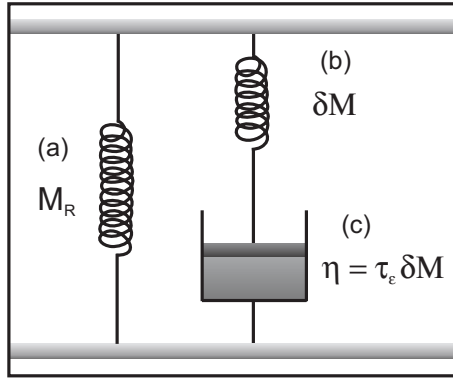


Fig. 3.6: Standard Anelastic Solid containing a Maxwell unit.

instantaneous elastic response. The qualitative features of this model (Fig. 3.5) are as follows. Upon application of stress, the spring (a) deforms immediately while, due to the dashpot, the Kelvin-Voigt unit remains undeformed. As time elapses, the dashpot (c) yields until the stress upon the Kelvin-Voigt unit is transferred entirely to the spring (b) and the stress on the dashpot vanishes. At this point there will be no further change in the system with time. This creep behaviour shows all of the characteristics of an anelastic material, in which the strain per unit stress goes from an instantaneous value J_U to a final value J_R . Clearly, from the model, the compliance of element (a) must be J_U while the combined compliance of elements (a) and (b) must be J_R . Therefore, if the compliance of element (b) is called δJ , J_R is given by $J_U + \delta J$ (as could be seen in 3.1.1.1). Finally, paralleling the procedure followed in the case of the Kelvin-Voigt model, the viscosity of the dashpot is set equal to a time constant divided by the compliance of the parallel spring. τ_σ is the relaxation time at constant stress. At that time $J(t)$ will have increased to all but $1/e$ of its total change δJ .

This model also is capable of describing stress relaxation, since it is possible to hold a strain. Initially, only element (a) will be extended, but the dashpot will then start to flow until the stress σ_c upon it is zero.

The stress-strain equations of this model are gained by starting from the relations $\epsilon_a = J_U \sigma_a$, $\epsilon_b = \delta J \sigma_b$, and $\dot{\epsilon}_c = \delta J \sigma_c / \tau_\sigma$, for elements (a), (b), and (c), respectively. By using Eqs. (3.21) and (3.23) it follows

$$\epsilon = \epsilon_a + \epsilon_b, \quad \epsilon_b = \epsilon_c \quad (3.25)$$

$$\sigma = \sigma_a = J_U^{-1} \epsilon_a = \sigma_b + \sigma_c = \delta J^{-1} (\epsilon_b + \tau_\sigma \dot{\epsilon}_c). \quad (3.26)$$

Eliminating ϵ_a , ϵ_b , ϵ_c , σ_a , σ_b , and σ_c , the differential stress-strain equation is derived

$$J_R \sigma + \tau_\sigma J_U \dot{\sigma} = \epsilon + \tau_\sigma \dot{\epsilon} \quad \text{where} \quad J_R = J_U + \delta J. \quad (3.27)$$

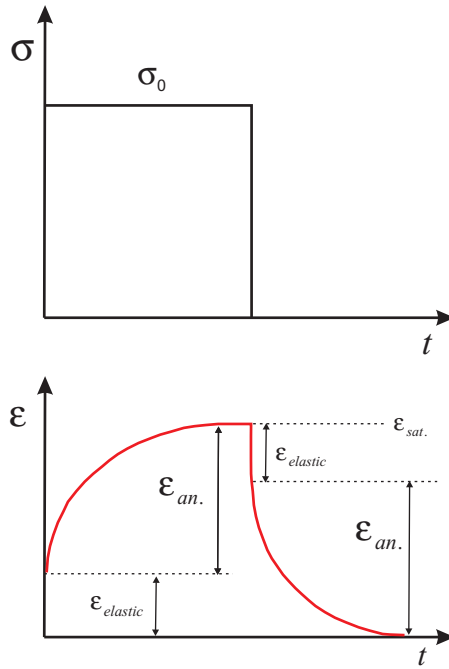


Fig. 3.7: Behaviour of the SAS model on loading and unloading.

The equation involves three independent parameters since the model contains three elements. Therefore, the SAS model is also called 'three parameter model'.

Analogously, the differential stress-strain equation for the SAS model based on a Maxwell unit is derived which is superior for the description of stress relaxation behaviour

$$\sigma + \tau_\epsilon \dot{\sigma} = M_R \epsilon + M_U \tau_\epsilon \dot{\epsilon}, \quad (3.28)$$

where the relaxation time at constant strain τ_ϵ determines the time to $1/e$ of completion of the stress relaxation process.

Fig. 3.7 shows the behaviour of the SAS model on loading and unloading.

Dynamic response functions of the SAS analogue to section 3.1.2 are obtained by substituting Eqs. (3.10) and (3.11) into the differential Eq. (3.27)

$$J_1(f) = J_U + \frac{\delta J}{1 + (2\pi f \tau_\sigma)^2} \quad (3.29)$$

$$J_2(f) = \delta J \frac{2\pi f \tau_\sigma}{1 + (2\pi f \tau_\sigma)^2}. \quad (3.30)$$

The relations are called Debye equations since they were first derived by Debye for the case of dielectric relaxation phenomena [45]. Analogous equations are derived for the modulus (see also Fig. 3.8)

$$M_1(f) = M_U - \frac{\delta M}{1 + (2\pi f \tau_\epsilon)^2} = M_R + \delta M \frac{(2\pi f \tau_\epsilon)^2}{1 + (2\pi f \tau_\epsilon)^2} \quad (3.31)$$

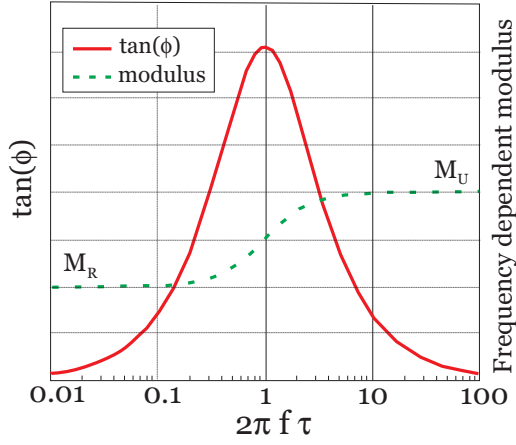


Fig. 3.8: SAS model: Debye peak, dynamic modulus.

$$M_2(f) = \delta M \frac{2\pi f \tau_\epsilon}{1 + (2\pi f \tau_\epsilon)^2}. \quad (3.32)$$

According to Eq. 3.17 the tangent of the loss angle is given by

$$\tan(\phi) = \frac{J_2}{J_1} = \delta J \frac{2\pi f \tau_\sigma}{J_R + J_U(2\pi f \tau_\sigma)^2} \quad (3.33)$$

This expression can be simplified by replacing τ_σ with $\bar{\tau}$, which is defined as the geometric mean of τ_σ and τ_ϵ ,

$$\bar{\tau} \equiv (\tau_\sigma \tau_\epsilon)^{1/2} = \tau_\sigma (J_U/J_R)^{1/2} = \tau_\sigma / (1 + \Delta)^{1/2} = \tau_\epsilon (1 + \Delta)^{1/2}. \quad (3.34)$$

The result is

$$\tan(\phi) = \frac{\delta J}{(J_U J_R)^{1/2}} \frac{2\pi f \bar{\tau}}{1 + (2\pi f \bar{\tau})^2} = \frac{\Delta}{(1 + \Delta)^{1/2}} \frac{2\pi f \bar{\tau}}{1 + (2\pi f \bar{\tau})^2}. \quad (3.35)$$

This function is called a *Debye peak* (see also Fig. 3.8). Its maximum occurs when $2\pi f \bar{\tau} = 1$

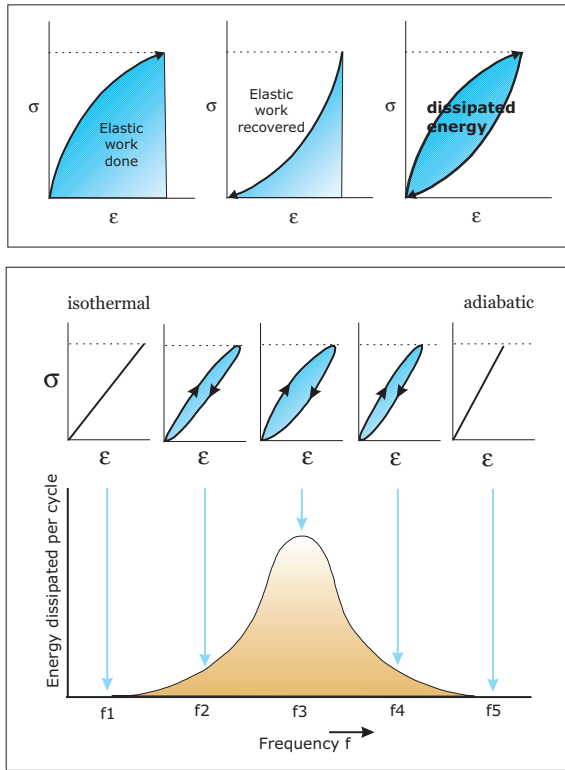
$$\tan(\phi_{\max}) = \Delta/2(1 + \Delta)^{1/2}. \quad (3.36)$$

For gravitational wave detection only low-loss materials are considered. For low losses ($\Delta \ll 1$, $\phi \ll 1$, $\tau_\sigma = \tau_\epsilon = \tau$) Eq. 3.35 can be simplified to

$$\tan(\phi) = \Delta \frac{2\pi f \tau}{1 + (2\pi f \tau)^2} \quad (3.37)$$

Then, also the tangent of the mechanical loss angle can be approximated by the loss angle itself

$$\phi = \Delta \frac{2\pi f \tau}{1 + (2\pi f \tau)^2} \quad (3.38)$$



Dissipation per cycle in dependence on frequency

Fig. 3.9: Dissipation per cycle in dependence on frequency.

and

$$\phi_{max} = \Delta/2. \quad (3.39)$$

Fig. 3.9 shows the dissipation per cycle caused by mechanical losses in dependence on frequency.

3.2 Anisotropic elasticity and anelasticity

In the preceding sections stress and strain have been treated as though they were scalar quantities. For (some modes of deformation of) an isotropic solid this is an appropriate description. However, for anisotropic materials, like crystals, dependences of the properties on the directions exist. In fact, stress and strain are symmetric second-order tensors. They are related by the elastic stiffness constants c_{ijkl} , respectively the elastic compliance constants s_{ijkl} , which are fourth-order tensors, in the generalised form of Hooke's law

$$\sigma_{ij} = c_{ijkl}\epsilon_{kl}, \quad (3.40)$$

$$\epsilon_{ij} = s_{ijkl}\sigma_{kl}. \quad (3.41)$$

Note, that the elastic constants are called 'constants' although they depend on frequency, and temperature. Stresses and strains are symmetric. The 6 independent components of stresses and strains, respectively, can be written as 6-dimensional vectors in Voigt notation [46, 47] with the components

$$\begin{aligned}\sigma_{11} &= \sigma_1, & \sigma_{22} &= \sigma_2, & \sigma_{33} &= \sigma_3, \\ \sigma_{23} &= \sigma_{32} = \sigma_4, & \sigma_{31} &= \sigma_{13} = \sigma_5, & \sigma_{12} &= \sigma_{21} = \sigma_6,\end{aligned}\quad (3.42)$$

and

$$\begin{aligned}\epsilon_{11} &= \epsilon_1, & \epsilon_{22} &= \epsilon_2, & \epsilon_{33} &= \epsilon_3, \\ \epsilon_{23} = \epsilon_{32} &= 1/2 \epsilon_4, & \epsilon_{31} = \epsilon_{13} &= 1/2 \epsilon_5, & \epsilon_{12} = \epsilon_{21} &= 1/2 \epsilon_6.\end{aligned}\quad (3.43)$$

Pairs of indices are replaced by a single index according to

$$11 \rightarrow 1 \quad 22 \rightarrow 2 \quad 33 \rightarrow 3 \quad 23, 32 \rightarrow 4 \quad 31, 13 \rightarrow 5 \quad 12, 21 \rightarrow 6 \quad (3.44)$$

At the same time factors of 2 and 4 are introduced for the elastic compliance constants

$$s_{ijkl} = s_{mn}, \text{ when } m \text{ and } n \text{ are } 1, 2, \text{ or } 3, \quad (3.45)$$

$$2s_{ijkl} = s_{mn}, \text{ when either } m \text{ or } n \text{ are } 4, 5, \text{ or } 6, \quad (3.46)$$

$$4s_{ijkl} = s_{mn}, \text{ when both } m \text{ and } n \text{ are } 4, 5, \text{ or } 6. \quad (3.47)$$

$$(3.48)$$

Thus, thanks to symmetry properties of stresses and strains the 81 elastic constants are reduced to 36. Moreover, the existence of a unique strain energy potential reduces them further to 21. In the simplified form Hooke's law is given by

$$\sigma_i = c_{ij}\epsilon_j, \quad (3.49)$$

$$\epsilon_i = s_{ij}\sigma_j. \quad (3.50)$$

The matrices of the elastic coefficients (c_{ij}) and (s_{ij}) change with the orientation of the coordinate axes for stress and strain in respect to the axes of crystal symmetry. A simple form is obtained when the standard orientation is chosen [47]. In the following these characteristic constants are used. The number of elastic constants is for most crystal systems further reduced due to symmetry reasons. In the cubic system there are 3 independent constants while in the trigonal system 6 constants exist. Matrices of the elastic stiffness and compliance constants as well as their relations are given for

Crystal system	Symmetry designation	Stress	Compliance	Strain
Cubic	A	$\sigma_1 + \sigma_2 + \sigma_3$	$\rightarrow s_{11} + 2s_{12}$	$\rightarrow \epsilon_1 + \epsilon_2 + \epsilon_3$
Trigonal	A	$\frac{1}{\sqrt{2}}(\sigma_1 + \sigma_2)$	$\rightarrow s_{11} + s_{12}$	$\rightarrow \frac{1}{\sqrt{2}}(\epsilon_1 + \epsilon_2)$
			\searrow	\nearrow
			$\sqrt{2}s_{13}$	
		\nearrow	\searrow	
		σ_3	$\rightarrow s_{33}$	$\rightarrow \epsilon_3$

Tab. 3.2: Symmetrized stresses, strains and compliances of type I [44]. The arrows indicate the relationships.

Crystal system	Symmetry designation	Stress	Compliance	Strain
Cubic	E	$2\sigma_1 - \sigma_2 - \sigma_3$	$\rightarrow s_{11} - s_{12}$	$\rightarrow 2\epsilon_1 - \epsilon_2 - \epsilon_3$
		$\sigma_2 - \sigma_3$	$\rightarrow s_{11} - s_{12}$	$\rightarrow \epsilon_2 - \epsilon_3$
		σ_4	$\rightarrow s_{44}$	$\rightarrow \epsilon_4$
		σ_5	$\rightarrow s_{44}$	$\rightarrow \epsilon_5$
		σ_6	$\rightarrow s_{44}$	$\rightarrow \epsilon_6$
Trigonal (higher symmetry classes)	E	σ_4	$\rightarrow s_{44}$	$\rightarrow \epsilon_4$
			\searrow	\nearrow
			$\sqrt{2}s_{14}$	
		\nearrow	\searrow	
		$\frac{1}{\sqrt{2}}(\sigma_1 - \sigma_2)$	$\rightarrow s_{11} - s_{12}$	$\rightarrow \frac{1}{\sqrt{2}}(\epsilon_1 - \epsilon_2)$
	$\rightarrow s_{44}$	$\rightarrow \epsilon_5$		
	\searrow	\nearrow		
		$\sqrt{2}s_{14}$		
	\nearrow	\searrow		
	$\frac{1}{\sqrt{2}}\sigma_6$	$\rightarrow s_{11} - s_{12}$	$\rightarrow \frac{1}{\sqrt{2}}\epsilon_6$	

Tab. 3.3: Symmetrized stresses, strains and compliances of type II [44]. The arrows indicate the relationships.

the cubic and trigonal system in the Appendix (Eqs. (A.7), (A.8), (A.9), (A.12), and (A.20)).

3.2.1 Symmetrized stresses and strains

A further simplification of Hooke's law can be obtained by using symmetrized stresses and strains. For each crystal system there are six independent linear combinations of the usual components of stress respectively strain which possess certain fundamental symmetry properties associated with that of the crystal, obtained by means of group theory [48]. For the cubic and trigonal case they are listed in Tab. 3.2 and 3.3, as well as the symmetrized compliances. The symmetrized stresses and strains are separated

according to the different ways in which they transform under the symmetry operations of the crystal. The kinds of transformations are associated with the irreducible representations (IRs) of the point group to which the crystal belongs, designated by the Mulliken symbols 'A', 'B', 'E', or 'T' [49]. Since a symmetry operation produces a linear transformation of coordinates, it will, in general, generate a linear combination of all six components of stress (or strain) by applying one. However, the symmetrized quantities show much simpler transformation behaviour. The symmetry designations are treated separately for the study of anelasticity. 'A' is referred to as 'totally symmetric'. The linear combinations associated with this IR are unchanged by carrying out any of the symmetry operations of the crystal. They are classified to be of type I while the remaining symmetrized components are referred to as type II. A strain of type I applied to a crystal does not change its symmetry while a crystal subjected to a type II strain is lowered in symmetry. The stresses and strains of type II are of a pure shear type. The symmetrized stresses and strains listed under 'B' simply transform into plus or minus themselves (B_1 or B_2). The IRs named 'E' are doubly degenerate. The symmetrized quantities occur in pairs. In general, one of them is taken into a linear combination of both under a symmetry operation. 'T' appears only for cubic crystals and refers to a triply degenerate symmetry designation.

If more than one symmetrized stress or pair of stresses occurs for a symmetry designation, the particular symmetry designation is said to be 'repeated'. Only in this case coupling between the symmetrized stresses or strains occur. Otherwise, they are decoupled which implies a great *simplification* in the description of anelastic behaviour. An example is given for the trigonal case. There are two symmetrized stresses and strains of type I

$$\left[(\epsilon_1 + \epsilon_2)/\sqrt{2} \right] = (s_{11} + s_{12}) \left[(\sigma_1 + \sigma_2)/\sqrt{2} \right] + \sqrt{2}s_{13}\sigma_3, \quad (3.51)$$

$$\epsilon_3 = \sqrt{2}s_{13} \left[(\sigma_1 + \sigma_2)/\sqrt{2} \right] + s_{33}\sigma_3. \quad (3.52)$$

The relevance of using symmetrized stresses and strains for the simplification of Hooke's law is summarized:

1. A symmetrized stress and a symmetrized strain which belong to different symmetry designations cannot be coupled to each other, i.e., the compliance constant relating such a stress and strain must be zero.
2. For a degenerate designation the corresponding stresses and strains of a given set are related by the same compliance constant while those which do not correspond are not coupled to each other.

From a practical viewpoint, however, it is difficult to apply these theoretically simple stress systems to an actual sample since it is hard to excite just one of the symmetrized stresses. Therefore, practical moduli like Young's modulus (E) and the torsional modulus (G) are used. For a crystal arbitrarily oriented in an experiment, these practical moduli involve all or several of the symmetrized compliances. Indeed, some practical moduli are related to just one symmetrized constant, or contain no more than one symmetrized constant of type I and one of type II. Experiments associated with those moduli are of special importance for studies of anelasticity.

Important practical moduli for the cubic and trigonal system are given in the following [44].

Cubic crystals:

$$E_{<100>}^{-1} = s_{11} = 1/3 [(s_{11} + 2s_{12}) + 2(s_{11} - s_{12})] \quad (3.53)$$

$$E_{<111>}^{-1} = 1/3 [(s_{11} + 2s_{12}) + s_{44}] \quad (3.54)$$

$$G_{<100>}^{-1} = s_{44} \quad (3.55)$$

$$(v_t^2 \rho)_{<100>} = c_{11} = 1/3 [(c_{11} + 2c_{12}) + 2(c_{11} - c_{12})] \quad (3.56)$$

$$(v_t^2 \rho)_{<100>} = (v_t^2 \rho)_{[110]}^{[001]} = c_{44} \quad (3.57)$$

$$(v_t^2 \rho)_{[110]}^{[1\bar{1}0]} = 1/2(c_{11} - c_{12}) \quad (3.58)$$

$$(v_t^2 \rho)_{<111>} = 1/3 [(c_{11} + 2c_{12}) + 4c_{44}] \quad (3.59)$$

Trigonal crystals:

$$E_{[001]}^{-1} = s_{33} \quad (3.60)$$

$$E_{[hk0]}^{-1} = s_{11} = 1/2 [(s_{11} + s_{12}) + (s_{11} - s_{12})] \quad (3.61)$$

$$G_{[001]}^{-1} = s_{44} \quad (3.62)$$

$$(v_t^2 \rho)_{[001]} = c_{33} \quad (3.63)$$

$$(v_t^2 \rho)_{[001]} = c_{44} \quad (3.64)$$

$$(v_t^2 \rho)_{[100]} = c_{11} = 1/2 [(c_{11} + c_{12}) + (c_{11} - c_{12})] \quad (3.65)$$

In the case of anelasticity, these moduli change. For instance, Young's modulus for the cubic system changes like

$$\delta E^{-1} = \delta s_{11} - 2 [\delta(s_{11} - s_{12}) - 1/2 \delta s_{44}] \Gamma. \quad (3.66)$$

Γ is given by

$$\Gamma = \gamma_1^2 \gamma_2^2 + \gamma_2^2 \gamma_3^2 + \gamma_3^2 \gamma_1^2 \quad (3.67)$$

where γ_1 , γ_2 , and γ_3 are the direction cosines between the direction of deformation and the three crystal axes. For the cubic case, Γ varies from zero for deformation in a $\langle 100 \rangle$ direction to a maximum value of $1/3$ for a $\langle 111 \rangle$ direction.

3.3 Internal losses in an 'ideal' solid

Assuming an 'ideal' solid without any defects present the bad news is that even this perfect solid shows mechanical losses. The important point for gravitational wave detection respectively thermal noise reduction is that it is not enough to improve the quality of the material regarding defects. Also, a minimum of these losses associated with the material itself has to be located.

In general, mechanical losses in an 'ideal' solid are caused by the coupling of temperature changes to mechanical motion, therefore named thermoelastic losses, and the interaction of acoustic waves with thermal phonons and free (conduction) electrons of the solid. The latter mechanism is not described in this thesis as only non-metallic materials are considered as potential materials for cryogenic gravitational wave detectors because of their lower losses.

The reason for the thermoelastic losses as well as the phonon induced losses is the anharmonicity of the crystal lattice leading to interactions of phonons. A major difference in both processes is the magnitude of the relaxation time. Thermoelastic relaxation times determined by thermal conduction are much longer than times for the relaxation of the phonon distribution. This statement is equal to that a temperature can be defined locally in a sample even if the whole piece is not in thermal equilibrium.

3.3.1 Thermoelastic losses

Thermoelastic losses occur due to a non-evanescent thermal expansion coefficient. The thermal expansion coefficient connects changes in temperature with changes in length. If parts of the solids are deformed by an acoustic wave their temperature changes. Compressed parts heat up, while expanded parts cool down. The arising temperature gradient is equalised by a heat flow accompanied by a conversion of oscillation energy into thermal energy. Note, that pure shear waves do not cause thermoelastic damping as they leave the volume unchanged.

The thermoelastic loss for a bar adiabatically vibrating in a longitudinal mode is given

by [50]

$$\phi_{te} = \kappa T \alpha^2 \rho 2\pi f / (9C^2). \quad (3.68)$$

Although this equation was derived for an isotropic medium it holds in order of magnitude also for an anisotropic crystal.

An equivalent description is given by [51]

$$\phi_{te} = \frac{E\alpha^2 T}{C} \frac{2\pi f \tau}{1 + (2\pi f \tau)^2}, \quad (3.69)$$

with the relaxation time

$$\tau = \frac{L^2}{D_{th}(n\pi v_s)^2}, \quad (3.70)$$

where $D_{th} = \kappa/C$ is the thermal diffusivity of the material, L is the length of the cylindrical bar, v_s is the speed of sound and n is the index of the mode. This relaxation time is the characteristic time needed for the diffusion of heat between regions of maximum compression and extension which are separated by a half wavelength $\lambda/2 = L/n$.

For flexural vibration modes of a thin disc of thickness h the losses are approximated by [52]

$$\phi_{te} = A_n \frac{1 + \nu}{1 - \nu} \frac{E\alpha^2 T}{C} \frac{2\pi f \tau}{1 + (2\pi f \tau)^2}, \quad (3.71)$$

where $A_n \leq 1$ is a dimensionless numerical constant characteristic of the n th flexural mode and $A_n = 1$ corresponds to plane bending. The relaxation time is independent of the mode number n for small n [51]

$$\tau = \frac{h^2}{\pi^2 D_{th}}. \quad (3.72)$$

For further details see [53, 54]. The relaxation time respectively the mechanical loss of thermoelastic processes is dependent on the geometry of the sample. Thermoelastic damping plays a major role in the loss processes of metals and, because of the small dimensions, in the coatings of the mirrors of the IGWDs. Due to the latter reason it also gets much attention in the work on Micro- and Nanoelectromechanical Systems (MEMS and NEMS) [55–57].

3.3.2 Losses due to interactions of phonons

The dissipation due to phonon-phonon interactions also occurs even in a perfect crystal. It is a result from the anharmonic properties of the crystal. With a purely harmonic potential the effects of different phonons would merely superpose. The interac-

tion mechanisms differ depending on whether the relaxation time τ respectively the mean lifetime of the phonons between two scattering processes is smaller or greater than the oscillation period ($2\pi f \tau < 1$ or $2\pi f \tau > 1$). In the first case, the thermal phonons of the crystal experience a slowly varying medium of elastic constants generated by the passing elastic wave. In the latter, the wave length of the acoustic wave as well as the mean free path of thermal phonons is of the same magnitude. Both kinds of phonons, acoustic and thermal, interact individually controlled by selection rules. The process occurring at higher temperatures where the wave length of the acoustic wave is far greater than the mean free path of the thermal phonons was suggested by Akhieser [58]. The strains induced by the passing acoustic wave change the frequencies of the various lattice vibrational modes. A useful assumption is that all thermal phonons belonging to the same branch k of the dispersion curve have the same Grüneisen number γ_k^j . The branch is defined by the polarization and propagation direction. The changes in frequency are then given by

$$(\Delta f/f)_k = -\gamma_k^j \epsilon_j. \quad (3.73)$$

Thus, the equilibrium distribution of the thermal phonons is disturbed. In equilibrium, the number of thermal phonons N in a mode m of frequency f_m is determined by the temperature T as described by the Planck distribution law which is a special case of the Bose-Einstein distribution law with zero chemical potential

$$N_m = [\exp(hf_m/(k_B T)) - 1]^{-1}. \quad (3.74)$$

The form of the distribution is not changed for the branches, assuming an accordingly changed temperature, as all frequencies of one branch are changed by the same fractional amount, but the number of phonons is perturbed from the equilibrium distribution. The assigned change in temperature can be positive or negative corresponding to the sign of the Grüneisen number according to

$$(\Delta T/T)_k = -\gamma_k^j \epsilon_j. \quad (3.75)$$

In a formal way, the relaxation of the phonon distribution towards a new equilibrium may then be described as a heat flow between the branches. In fact, the redistribution occurs by interactions among the thermal phonons. The time needed to establish a new state of equilibrium is the relaxation time τ . An often used approximation for the relaxation time is [44]

$$\tau_{th} = 3\kappa/(v_s^2 C), \quad (3.76)$$

where v_s is the Debye-averaged sound velocity

$$3/v_s^3 = 2/v_t^3 + 1/v_l^3, \quad (3.77)$$

v_t being the mean transverse phonon velocity (slow and fast transverse waves exist), and v_l the longitudinal phonon velocity. Actually, this equation holds for an isotropic solid. For anisotropic crystals there are methods available for determining a suitable average velocity [59].

Eq. (3.76) describes a time related to processes of thermal conductivity. Unlike in relaxation processes thermal resistivity is determined only by Umklapp processes (U-processes) [44]. The probability of U-processes decreases very rapidly with decreasing temperature (as $\exp[-\text{constant}/(k_B T)]$). Therefore, at low temperatures ($T \ll \Theta_D$, with Debye temperature Θ_D) Normal processes (N-processes) mainly occur and Eq. (3.76) no longer holds. The relaxation strength of the Akhieser damping is determined according to Eq. (3.35) by a change of the modulus. For a longitudinal wave the change in elastic constant is approximated using a mean square average Grüneisen number $\overline{\gamma^2}$ [60, 61]

$$\delta c_{11} = CT\overline{\gamma^2}. \quad (3.78)$$

However, $\overline{\gamma^2}$ serves as a semi-empirical constant and should not be mixed up with the square of the ordinary Grüneisen constant. Since the various branches of the phonon spectrum are excited in different temperature ranges $\overline{\gamma^2}$ should be temperature dependent. A more complete expression for the elastic constants c_{ii} therefore summarized over the contributions of the different branches k

$$\delta c_{ii} = T \sum_k C_k (\gamma_k^i)^2. \quad (3.79)$$

where C_k is the specific heat capacity associated with the k^{th} branch. Assuming low losses, the mechanical loss itself is given by loss itself, for low losses:

$$\phi = \frac{\delta c_{ii}}{c_{ii}} \frac{2\pi f \tau}{1 + (2\pi f \tau)^2} = \frac{\delta c_{ii}}{\rho v_s^2} \frac{2\pi f \tau}{1 + (2\pi f \tau)^2}, \quad (3.80)$$

where ρ is the density of the material. Still, the problem of the determination of Grüneisen numbers γ_k^i remains. Often the oversimplified but often useful approximation has been made that the phonon frequencies depend on dilatational type of strains only and all branches have the same Grüneisen number which is given by

$$\gamma = 3\alpha K/C, \quad (3.81)$$

where K is the isothermal bulk modulus. Another way of describing anharmonicity equal to Grüneisen numbers is in terms of third-order elastic constants as both are related.

Some groups have worked on the Akhieser theory. To my knowledge, the evaluation of Woodruff and Ehrenreich [61] is the most detailed and accepted one. On the other hand, their rigorous theory is too impracticable to allow direct comparison with experiments. Thus, simplified approaches have been considered here. The process of the Akhieser effect is in principle well understood, but a quantitative expression for explaining experimental data is still lacking.

In the Akhieser regime the whole assembly of thermal phonons is modulated by the impressed acoustic wave. At lower temperatures where the mean free path of the thermal phonons is of similar magnitude or greater than the wave length of the acoustic wave interactions between the individual phonons - acoustic and thermal - take place. This effect was originally suggested by Landau and Rumer [62].

Three phonon processes which means that the incoming acoustic phonon collides with a thermal phonon to generate a second thermal phonon. In these interactions the laws of conservation - energy and momentum - have to be obeyed. The conservation of energy is related to

$$f_{ac} + f_{tp1} = f_{tp2}, \quad (3.82)$$

while the conservation of momentum is described by

$$\vec{q}_{ac} + \vec{q}_{tp1} = \vec{q}_{tp2} + \vec{G}. \quad (3.83)$$

with the reciprocal lattice vector of the crystal \vec{G} . As written before U-processes with $G \neq 0$ become seldom at low temperatures. Also, U-processes are highly unlikely when one phonon is in the low frequency ($< 10^{10}$ Hz) range. This is the case for our Q measurements with resonance frequencies in the kHz-range. Therefore, only N-processes are considered.

Many efforts have been made to model the interactions of acoustic waves with thermal phonons [61, 63–76]. Nevertheless, especially high-frequency acoustic waves have been taken into account, in contrary to our measurements in the kHz range [77–88]. The losses due to thermal phonons can be decreased in the Akhieser regime by introducing point defects in the crystal, e. g., by radiation damage. The reduction has its origin in the decrease of the lifetime of the thermal phonons by more frequent collisions with point defects. On the other hand, this decrease in lifetime increases the uncertainty of the phonon frequency. In the Landau-Rumer regime the probability of interactions of acoustic phonons with thermal ones grows thus increasing the losses in this region.

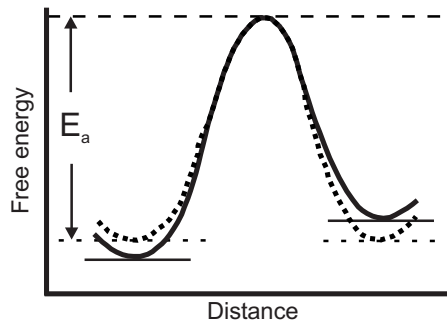


Fig. 3.10: Double-well potential.

3.4 Internal losses in a 'real' solid

In a 'real' solid containing defects additional losses to those described in the preceding section 3.3 appear. Nevertheless, since we are dealing with certain low-loss materials, some defects are largely not present. These materials are quite hard which means that they withstand plastic deformations. Plastic deformations are correlated with the creation and movement of dislocations [89]. Thus, e. g., dislocations play a minor role. Losses due to free electrons were also of minor importance as no metals have been studied. Thus, the mechanical losses in our experiments are mainly assigned to be induced by thermal phonons, point defects and surface effects. Surface effects can be strongly reduced by polishing. The remaining influence of point defects is described in the following section.

3.4.1 Point defect related relaxations

Point defects possess properties that are of importance concerning anelasticity. They distort the lattice and they are in general capable of migrating in the crystal. The jump of a defect from one site in a crystal lattice to another can be described by a jump from one potential minimum to another in a double-well potential. Thereby a wall with a height equal to the activation energy E_a has to be overcome (Fig. 3.10). Thermally activated jumps permanently occur at a sufficient temperature. The occupation numbers of the states with minimum potential energy, indeed, remain the same, forming a dynamic equilibrium. However, an arriving acoustic wave may lift one side of the potential while the other side is lowered, depending on the direction of propagation and polarisation of the wave. The occupation numbers of the new equilibrium state are different to that of the former equilibrium. Therefore, an effective redistribution of the defects from the state of higher to that of lower potential energy occurs. This process, called relaxation, takes some time, named relaxation time (cf. 3.1.5). Through the redistribution, energy is dissipated to the thermal bath. This energy is in effect withdrawn from the oscillation. The result is a damped vibration.

The relaxation time depends exponentially upon the reciprocal temperature [90]

$$\tau = \tau_0 \exp\left(\frac{E_a}{k_B T}\right), \quad (3.84)$$

similar to the Arrhenius law. The combination of Eqs. (3.38) and (3.84) results in

$$\tan(\phi) = \Delta \frac{2\pi \cdot f \cdot \tau_0 \cdot e^{\frac{E_a}{k_B T}}}{1 + \left(2\pi \cdot f \cdot \tau_0 \cdot e^{\frac{E_a}{k_B T}}\right)^2}. \quad (3.85)$$

Especially at very low temperatures there exists another process than that of thermal activation described above. A particle can overcome the potential barrier by quantum-mechanical tunnelling [91].

An adequate way of describing point defect induced relaxation is based upon considerations of symmetry [44, 48, 92, 93]. The applied stress is taken to be homogeneous, so that only the type of site on which a defect is situated (and not its exact location) is important. This consideration reduces the possible symmetry operations to that of rotational type which are collected in the 32 point groups.

Now the case of just one point defect is considered. The presence of the defect destroys the translational symmetry of the crystal, and the resultant crystal may be thought of as a large molecule. The point-group symmetry of this defective crystal is named 'defect symmetry'. The defect symmetry can be lower than or equal to that of the former crystal. In the first case there exist n_d distinguishable configurations or orientations of the defect. For an elementary defect like a single substitutional or interstitial atom, or a vacancy the defect symmetry is equal to the site symmetry of the defect, not considering a probable further lowering of symmetry through readjustment of the surrounding lattice. The site symmetry, which is generally different for different points in the unit cell of the crystal, depends on the space group of the crystal and is conveniently given in the International Tables for X-ray Crystallography [94] for all possible sites in all of the 230 space groups. The defect symmetry of a composite defect can be lower or equal to the site symmetry. The following description of anelastic behaviour due to point defects follows that of Nowick and Berry [44].

3.4.1.1 Elastic dipole

A point defect introduced into a crystal produces local distortions. These distortions enable an interaction between the defect and an applied stress. Because of the analogy to the interaction of an electric dipole with an electric field the defect producing local distortions has been called elastic dipole [95].

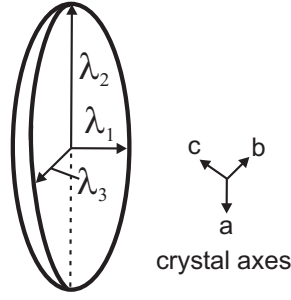


Fig. 3.11: The strain ellipsoid of the λ tensor for a particular defect orientation in the crystal.

The strain introduced by a defect is

$$\epsilon_{ij}^d - \epsilon_{ij}^0 = \sum_{p=1}^{d_d} \lambda_{ij}^{(p)} C_p. \quad (3.86)$$

ϵ_{ij}^d and ϵ_{ij}^0 are the strains of the crystal with and without defects and p is the index of the relevant defect orientation going from 1 to n_d .

$$C_p = V_0 N_p \quad (3.87)$$

is the mole fraction of defects in orientation p , with the molecular volume V_0 and the number of defects in orientation p per unit volume N_p . $\lambda_{ij}^{(p)}$ is the strain per mole fraction of defects that have the same orientation p , characterising the elastic dipole. This second-order tensor which completely determines the interaction of a defect with a stress field is given by

$$\lambda_{ij}^{(p)} = \partial \epsilon_{ij} / \partial C_p. \quad (3.88)$$

The λ tensor is symmetric since it represents a strain tensor and can be visualised by a strain ellipsoid with three perpendicular axes (Fig. 3.11). In the coordinate system of the principal axes, the λ tensor is of diagonal form, with the principal values λ_1 , λ_2 , and λ_3 and independent of the orientation p

$$\begin{pmatrix} \lambda_1 & 0 & 0 \\ 0 & \lambda_2 & 0 \\ 0 & 0 & \lambda_3 \end{pmatrix}. \quad (3.89)$$

$\lambda_{ij}^{(p)}$ can be gained from the principal values by

$$\lambda_{ij}^{(p)} = \sum_{m=1}^3 \alpha_{im}^{(p)} \alpha_{jm}^{(p)} \lambda_m, \quad (3.90)$$

where $\alpha_{im}^{(p)}$ is the direction cosinus between the axis i and the m^{th} principal axis for the dipole orientation p . In general, there is no simple relation between the crys-

tal axes and the principal axes of the λ tensor. Indeed, when the defect possesses symmetry, the principal axes lie along the symmetry axes of the defect and in some cases the number of independent principal values is decreased from three to either two or one (cf. Tab. A.1). Since the form of the λ tensor is determined solely by the symmetry system of the defect, the same λ tensor may belong to different defect orientations. Accordingly, two defects with different orientations but the same λ tensor are indistinguishable by analysing their behaviour under stress. For the number of independent λ tensors n_t holds $n_t \leq n_d$. If $n_t = 1$ all defects (with different orientation) behave identically under an applied stress. If $n_t > 1$ a redistribution of defects occur with one defect orientation energetically favoured over the others, causing anelasticity. This means that the criterion for anelasticity due to point defects is that $n_t > 1$. In other words, only a defect with a system of lower symmetry than that of the crystal can cause anelastic relaxation. For the values of n_t for various defect symmetries in the cubic and trigonal crystal system see Tab. A.2.

There are equivalent descriptions of the elastic dipole. Kröner [96] characterised the elastic dipole by the negative stresses needed to maintain constant strain per unit concentration of defects introduced into orientation p

$$P_{ij}^{(p)} = -\partial \sigma_{ij} / \partial N_p = -V_0 (\partial \sigma_{ij} / \partial C_p). \quad (3.91)$$

P tensor and λ tensor are related by the elastic constants

$$P_{ij}^{(p)} = V_0 \sum_{k,l} c_{ijkl} \lambda_{kl}^{(p)}, \quad (3.92)$$

$$\lambda_{ij}^{(p)} = V_0^{-1} \sum_{k,l} s_{ijkl} P_{kl}^{(p)}. \quad (3.93)$$

The sum of the mole fractions of defects in orientation p , C_p , over all crystallographic equivalent orientations is constant

$$\sum_{p=1}^{n_t} C_p = C_0 = \text{constant}. \quad (3.94)$$

A defect may change its orientation, but does not vanish. Also, no new defects are introduced. With no stress applied all crystallographic equivalent orientations are equally occupied, $C_p = C_0/n_t$ for all p . By applying an homogeneous uniaxial stress the corresponding strain is given by

$$\epsilon = J_U \sigma + \sum_{p=1}^{n_t} \lambda^{(p)} [\bar{C}_p - C_0/n_t]. \quad (3.95)$$

The first term represents the elastic strain, while the second gives the anelastic strain. $\lambda^{(p)}$ can be calculated by Eq. (3.90). For the calculation of the relaxation strength the equilibrium values of the concentrations \bar{C}_p for a given stress are required. The deviation from the concentration in the unstressed solid is proportional to the stress and the total concentration

$$\bar{C}_p - \frac{C_0}{n_t} \approx \frac{C_0 V_0 \sigma}{n_t k_B T} \left[\lambda^{(p)} - \frac{1}{n_t} \sum_q \lambda^{(q)} \right]. \quad (3.96)$$

The redistribution of the elastic dipoles under an applied stress to a new equilibrium is called stress-induced ordering. The substitution of Eq. (3.96) into (3.95) gives the relaxation of the compliance

$$\delta J = \frac{\bar{\epsilon}^{an}}{\sigma} = \frac{C_0 V_0}{n_t k_B T} \left[\sum_p (\lambda^{(p)})^2 - \frac{1}{n_t} \left(\sum_p \lambda^{(p)} \right)^2 \right]. \quad (3.97)$$

The particular $\lambda^{(p)}$ can be obtained by using Eq. (3.90). Values for n_t for the cubic and trigonal system are listed in Tab. A.2. Eq. (3.97) is valid for any simple stress system. It can be simplified to

$$\delta J = \beta_n (C_0 V_0 / k_B T) (\delta \lambda)^2, \quad (3.98)$$

where β_n is a numerical factor of the order of unity and $\delta \lambda$ is the appropriate difference in principal values. An estimation of $\delta \lambda$ is calculated for interstitial sodium ions in crystalline quartz as studied in section 5.2 using Eq. 3.98 [39]. The sodium fraction in our samples lies below by ICP-OES (Inductively Coupled Plasma Optical Emission Spectrometry) detectable amounts of $3 \mu\text{g}$ per g. Thus, the concentration of defects is $C_0 < 3 \times 10^{-6} M_{\text{SiO}_2} / M_{\text{Na}} = 3 \times 10^{-6} \cdot (60.09 \text{ g/mol}) / (22.99 \text{ g/mol}) \approx 7.8 \times 10^{-6}$, where M_{SiO_2} respectively M_{Na} are the molar masses. The molecular volume is $V_0 = M_{\text{SiO}_2} / (\rho_{\text{SiO}_2} N_A) = (60.09 \times 10^{-3} \text{ kg/mol}) / (2648 \text{ kg/m}^3 \cdot 6.0221353 \times 10^{23} \text{ mol}^{-1}) \approx 3.77 \times 10^{-29} \text{ m}^3$. δJ is estimated using the maximum measured loss of $\phi_{\text{max}} \approx 2 \times 10^{-5}$ at $T_{\text{peak}} = 35 \text{ K}$ for a z-cut crystalline quartz sample (cf. Fig. 5.4(a)), $\delta J = 2 \phi_{\text{max}} J = 2 \cdot 2 \times 10^{-5} / (76.5 \text{ GPa}) \approx 5.2 \times 10^{-16} \text{ m}^2/\text{N}$.

The result is $\delta \lambda = \sqrt{\delta J k_B T_{\text{peak}} / (\beta_n C_0 V_0)} \approx 0.03$. Thus, differences in strains per unit concentration of defects in two principal directions of about 3 % are yielded, assuming $3 \mu\text{g}$ sodium per g of crystalline quartz. In fact, $\delta \lambda$ could be higher due to a smaller defect concentration. Therefore, other methods than ICP-OES with higher sensitivity like ICP-MS (Inductively Coupled Plasma Mass Spectrometry) [97] should be applied to determine the defect concentration in the future.

For certain stresses there is a complete absence of any relaxation as a consequence of the defect symmetry. Therefore, 'selection rules' for the existence or absence of

relaxation under a certain stress are given in the next section. Because of the relation of the relaxation to the defect symmetry they provide an important basis for the identification of the symmetry of an unknown defect in a given crystal.

3.4.1.2 Selection rules

Selection rules offer evidence of the existence or absence of relaxation under a certain stress but they do not say anything about relaxation strengths. If a certain symmetry is assigned to a defect and the selection rules allow for a relaxation, this relaxation nevertheless might not be observed. Then, the predicted symmetry need not be wrong in any case. A reason might be that $C_0(\delta\lambda)^2$ (cf. Eq. 3.98) is too small to detect.

In the following it is assumed that only a single species of defect is present, so that the conservation condition Eq. (3.94) applies. Then, only compliances of type II contribute to relaxation. Recall that a compliance of type I does not reduce the symmetry of the crystal. Therefore, a symmetry operation of this kind taking p into q leaves $\lambda^{(p)} = \lambda^{(q)}$. In this case $\lambda^{(p)}$ is independent of p , resulting in $\delta J = 0$ which can be seen from Eq. (3.97). Thus, only stresses and compliances of type II have to be considered.

Eq. (3.86) is reexamined in terms of symmetrized stresses and strains as well as symmetrized linear combinations of the concentrations. The basic principle behind it is that a given symmetrized coordinate of concentration can only generate a strain which is of the same symmetry designation, i. e., which transforms in the same manner under symmetry operations of the crystal. The original set of concentrations is taken as the basis for an n_d -dimensional representation of the crystal group which is then reduced to IRs. If a symmetry coordinate of strain belongs to the same IR as one of the symmetry coordinates of concentration, the corresponding compliance will undergo relaxation. The resulting selection rules are arranged in Tabs. 3.4 and 3.5. The numbers given in the table (1, 2, or 3) indicate the number of distinct relaxation times. The magnitude of relaxation for symmetrized compliances of type II S'_γ with symmetry designation γ can then be calculated for any crystal and defect symmetry

$$\delta S'_\gamma = \frac{C_0 V_0}{n_t k_B T} \lambda'^2_\gamma, \quad (3.99)$$

where λ'_γ is the symmetrized component of the λ tensor for the designation γ . This equation differs from Eq. (3.97) in that the last term of Eq. (3.97) is zero for the considered compliances of type II which correspond to pure shear stresses. The sum $\sum_p (\lambda^{(p)})^2$ is replaced by the simpler term λ'^2_γ . The expression of λ'_γ is carried out in terms of the components $\lambda^{(p)}_{ij}$ for one value of p (e.g., $p=1$) [48]. Results for the

Crystal	Compliance	Defect			
		Tetragonal	Trigonal	Orthorhombic < 100 > < 110 >	
Cubic (O_h, T_d, O)	$s_{11} - s_{12}$	1	0	2	1
	s_{44}	0	1	0	1
Trigonal (D_{3h}, C_{3v}, D_3)	$s_{11} - s_{12}$	}	-	0	-
	s_{44}				
	s_{14}				

Tab. 3.4: Selection rules for anelasticity, part 1 [44, 48]. The numbers given (1, 2, or 3) indicate the number of distinct relaxation times. '0' means that no relaxation occurs. A dash indicates that the defect symmetry is not possible in the particular crystal system.

Crystal	Compliance	Defect		
		Monoclinic < 100 >	Trigonal < 110 >	Triclinic
Cubic (O_h, T_d, O)	$s_{11} - s_{12}$	2	1	2
	s_{44}	1	2	3
Trigonal (D_{3h}, C_{3v}, D_3)	$s_{11} - s_{12}$	}	-	2
	s_{44}			
	s_{14}			

Tab. 3.5: Selection rules for anelasticity, part 2 [44, 48]. The numbers given (1, 2, or 3) indicate the number of distinct relaxation times. '0' means that no relaxation occurs. A dash indicates that the defect symmetry is not possible in the particular crystal system.

magnitude of relaxation of the type II shear compliances are arranged for the cubic and trigonal crystal systems, omitting the superscript p for convenience.

Cubic:

$$\delta(S_{11} - S_{12}) = \frac{C_0 V_0}{6k_B T} [(\lambda_{11} - \lambda_{22})^2 + (\lambda_{11} - \lambda_{33})^2 + (\lambda_{22} - \lambda_{33})^2], \quad (3.100)$$

$$\delta S_{44} = \frac{4C_0 V_0}{3k_B T} [\lambda_{23}^2 + \lambda_{31}^2 + \lambda_{12}^2]. \quad (3.101)$$

Trigonal:

$$\delta(S_{11} - S_{12}) = \frac{C_0 V_0}{4k_B T} [(\lambda_{11} - \lambda_{22})^2 + 4\lambda_{12}^2], \quad (3.102)$$

$$\delta S_{44} = \frac{2C_0 V_0}{k_B T} [\lambda_{23}^2 + \lambda_{31}^2], \quad (3.103)$$

$$\delta S_{14} = \frac{C_0 V_0}{2k_B T} [\lambda_{23}(\lambda_{11} - \lambda_{22}) + 2\lambda_{13}\lambda_{12}]. \quad (3.104)$$

Eqs. (3.100)-(3.104) are applicable for defects of any allowed symmetry in the corresponding crystal. For the substitution of $\lambda_{ij}^{(1)}$ in terms of the principal values see Tab. A.3. Using the above expressions for the relaxation of the symmetrized compliances, δE^{-1} or δG^{-1} can be obtained for any orientation in the crystal by the aid of the appropriate equations in section 3.2.1.

Thus, two alternatives can be used

- Eqs. (3.100)-(3.104) plus a complete set of components $\lambda_{ij}^{(1)}$ for *one* defect orientation or
- Eq. (3.97) plus the component $\lambda_{11}^{(p)}$ in the direction of uniaxial stress but for *all* defect orientations.

A remaining problem is that not all independent components of the λ tensor are accessible by anelastic measurements (cf. Tab. A.1). Missing components can be obtained by measuring changes in the lattice parameters of a crystal due to the presence of a collection of randomly oriented defects which give rise to strains of type I. For cubic crystals, the type I strain is purely hydrostatic. The relative change in lattice parameter 'a' per unit concentration of defects is

$$a^{-1}(da/dC_0) = 1/3(\lambda_1 + \lambda_2 + \lambda_3), \quad (3.105)$$

and in the case for a trigonal crystal

$$a^{-1}(da/dC_0) = 1/2(\lambda_1 + \lambda_2), \quad (3.106)$$

$$c^{-1}(dc/dC_0) = \lambda_3. \quad (3.107)$$

Note that dielectric relaxation is also subject to selection rules that may coincide with the anelastic ones [48, 98]. Thus, measurements of dielectric losses could be a useful additional method to mechanical loss measurements.

As mentioned before, Tabs. 3.4 and 3.5 give the number of distinct relaxation times for the specified defect and crystal symmetry. These relaxation times can be written in terms of the probabilities per second for a dipole to change from orientation p to q, ν_{pq} , for one orientation p (e. g., p=1). If there is more than one independent ν_{1q} , a numbering system for the dipoles is required. A compact form is given with a stereographic-projection diagram. The diagram is drawn such that the major symmetry axis reaches out of the page and gives for each dipole orientation the position where a given principal axis intersects the reference sphere.

For trigonal crystals, there are three compliances showing relaxation and having all the same relaxation times since they belong to the same symmetry designation. The

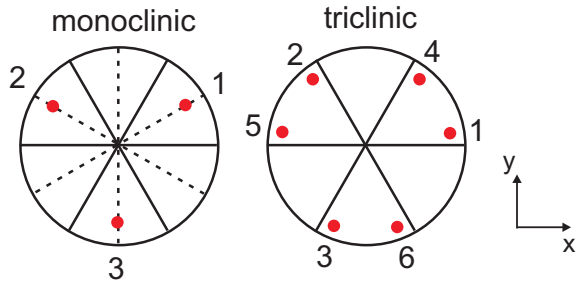


Fig. 3.12: The numbering convention for defects in trigonal crystals [44].

projection diagram is shown in Fig. 3.12 and the relaxation rates are [44]

Monoclinic defect:

$$\tau^{-1} = 3\nu_{12}. \quad (3.108)$$

Triclinic defect:

$$\tau^{-1} = (3\nu_{12} + \nu_{14} + \nu_{15} + \nu_{16}) \pm 1/2 \left[(\nu_{14} - 2\nu_{15} + \nu_{16})^2 + 3(\nu_{14} - \nu_{16})^2 \right]^{1/2}. \quad (3.109)$$

In many cases, like for the triclinic effect in a trigonal crystal (Eq. 3.109), a defect can give rise to two or more relaxation times which may differ considerably from each other, and thus may be even decades apart in their magnitudes. For the concomitant phenomenon of the 'frozen-free split' see the appendix.

Note, that in this chapter assumptions have been made for a first practicable description of the mechanical losses induced by point defects. Thus, only defects of a single species (crystallographically equivalent set) have been considered. For further effects, 'reactions' of defects, the conversion of a defect of one species into another species, may be taken into account, in particular for crystalline quartz [98]. 'Interactions' of defects are negligible since the crystals used are of such high quality that remaining defects are strongly diluted.

3.5 Overview of external losses

The determination of internal mechanical losses, associated with processes in the material, requires the external losses to be of lower order of magnitude. Main external loss sources occurring in our experiments are briefly outlined in the following.

For the measurement of its internal mechanical losses the sample has to be suspended. The points of contact to the suspension allow for a transfer of oscillation energy from the vibrating substrate to the suspension where it might be dissipated. Thus, measurements on modes with larger displacement in the area of contact to the suspension show in general higher losses [99].

Residual gas damping may also cause additional losses. At the usually low pressures a

momentum transfer between the vibrating sample and the surrounding gas molecules that collide with it is the dominating source. The result is a damping effect. The magnitude of residual gas damping is inversely proportional to the residual gas pressure as well as the surface area, and proportional to the frequency of the motion. Therefore, the measurement of mechanical losses should be performed under vacuum. For details on residual gas damping see [8].

3.6 Estimation of losses far below the resonant frequencies

A direct measurement of the mechanical losses at the frequencies of the detection band of IGWDs is impracticable for big samples with a geometry similar to that of the test masses of the IGWDs, possessing resonant frequencies above 10 kHz. In the off-resonant region only diminutive oscillation amplitudes can be achieved. Using samples of a smaller size with lower resonant frequencies like vibrating reeds [100], on the other hand, has the disadvantage for the study of substrate materials of a smaller volume to surface ratio and possible different effects of geometry dependent parameters like the thermal conductivity. A more feasible approach is to determine the mechanical losses at the resonances of the test masses and then extrapolate the losses in the lower frequency region. At a resonant frequency, the reciprocal of the mechanical loss factor is given by the quality factor, or Q factor, of the oscillation.

$$\frac{1}{\phi(f_0)} = Q(f_0). \quad (3.110)$$

The Q factor is proportional to the ratio of the stored energy E_{max} to the dissipated energy ΔE_{max} during an oscillation cycle

$$Q = 2\pi \cdot \frac{E_{max}}{\Delta E_{max}}. \quad (3.111)$$

In temperature and frequency regions with only minor variations of the mechanical losses, the reciprocals of the Q factors provide a good approximation for the losses at off-resonant frequencies. This is the case for fused silica at room temperature as can be seen in section 5.1. However, this approximation may not hold for a wide temperature range, e. g. down to cryogenic temperatures. Therefore, it is preferable to extrapolate the mechanical losses at other frequencies than the resonant ones by performing systematic Q measurements.

Combining Eqs. (3.38) and (3.110) a single relaxation effect causes a damping at the

resonant frequency f_0 of the sample

$$Q_{rel}^{-1}(f_0, T) = \Delta(f_0, T) \frac{2\pi \cdot f_0 \cdot \tau}{1 + (2\pi \cdot f_0 \cdot \tau)^2}. \quad (3.112)$$

The temperature dependence of the resonant frequency has been omitted as it changes less than 2 % between 5 K and 300 K for the materials which we have investigated (fused silica, crystalline quartz, silicon, and calcium fluoride) and as such has a minor effect on damping.

The total damping at f_0 is the sum over all relaxation losses plus background damping Q_{bg}^{-1} due to, for example, losses in the suspension of the sample (cf. section 3.5)

$$Q^{-1}(f_0, T) = \sum_i Q_{rel,i}^{-1}(f_0, T) + Q_{bg}^{-1}(f_0, T). \quad (3.113)$$

With Eq. (3.112) the total damping is determined by

$$Q^{-1}(f_0, T) = \sum_i \Delta_i(f_0, T) \frac{2\pi \cdot f_0 \cdot \tau_i}{1 + (2\pi \cdot f_0 \cdot \tau_i)^2} + Q_{bg}^{-1}(f_0, T). \quad (3.114)$$

Therefore by measuring the damping, or rather the Q factor, it should be possible to obtain the relaxation parameters, assuming that the background losses are sufficiently small.

In order to extrapolate the losses at off-resonant frequencies by using Eqs. (3.114) in this frequency range, the dependences of the relaxation strength on temperature, frequency, and on the directions of the crystal, as well as the mode shape must be known. Since the mechanical losses in anisotropic materials can vary significantly for different directions in the solid, optimal crystal cuts can be chosen. In iron, for instance, losses induced by hopping carbon impurities are observable when applying stresses in the $\langle 100 \rangle$ directions whereas in the $\langle 111 \rangle$ directions the losses decrease to zero [101]. Further, the temperature and frequency dependences of the relaxation times that do not follow the Arrhenius-like law (Eq. (3.84)) must be known, as well as those of the background losses. In summary, for each application, an optimal operation temperature can be determined for the frequency band at which mechanical losses should be minimal.

4 Cryogenic Resonant Acoustic spectroscopy of bulk materials (CRA spectroscopy)

Systematic measurements of the mechanical quality factor Q on low-loss materials require a high sensitivity method stable from room temperature to cryogenic temperatures. To fulfil these demands a new kind of mechanical spectroscopy, Cryogenic Resonant Acoustic (CRA) spectroscopy of bulk materials, has been established in our project. The following sections give a brief overview of the method. For a detailed description and characterisation see [8].

4.1 Overview of experimental setup and measuring principle

The experimental setup is placed inside a custom made cryostat to perform the Q measurements within a temperature range from 5 K to 300 K (Fig. 4.1) [102]. The

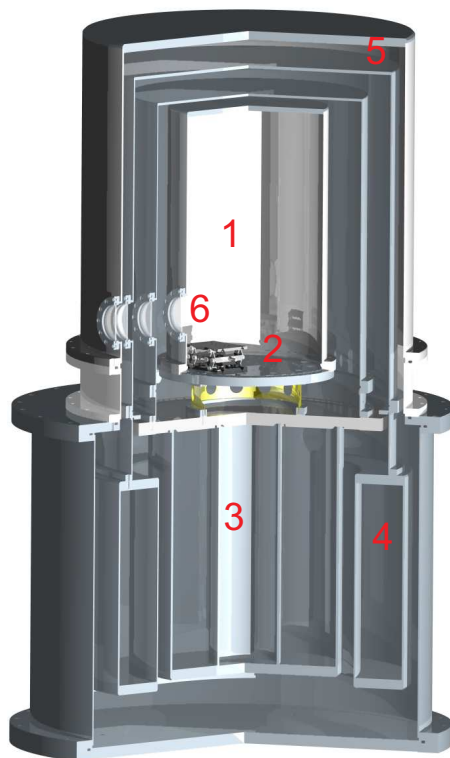


Fig. 4.1: Schematic of the custom made cryostat [103]. 1 - probe chamber, 2 - experimental platform, 3 - LHe tank, 4 - LN₂ tank, 5 - isolation shields, 6 - optical windows.

experimental platform is located above the liquid helium tank. Fig. 4.2 gives a view into the probe chamber. In combination of cooling with the boil-off gas from the liquid helium tank and heating the desired temperature can be achieved by means of a LakeShore temperature controller (LS340) and is kept during the Q measurements to better than 0.3 K. A non-contact measurement of the temperature of the first sample is done by determining the temperature of a 'twin substrate' - identical in material and shape - which is symmetrically placed to the first one and has a calibrated temperature sensor attached to it. Due to the symmetric setup the second sample will have the same temperature as the first one. To reduce residual gas damping the probe chamber is evacuated to at least 10^{-3} Pa. The sealing is done by metallic indium.

The analysed samples were cylindrical in shape with a diameter typically of 76.2 mm and thicknesses varying between 6 mm and 75 mm. Thus, our samples were smaller in size than the mirror substrates of the IGWDs. Using samples of original size would have been too expensive and would have required even much more technical effort as already was the case. Nevertheless, for the analysis of internal mechanical losses in the materials it only had to be guaranteed that the influence of the surface losses as well as the suspension losses are inferior to the effect of the intrinsic processes. This could be assured by a careful sample preparation and a sophisticated suspension system.

The samples were cut to the desired orientation with an accuracy of better than one degree. This work as well as polishing of the samples (front side, back side, and circumference) was done by the company Hellma-Optik [104], which is specialized on polishing of optical components. As a result of this process the crystal exhibits a roughness lower than 10 nm on all surfaces. After this geometrical manufacturing, the sample passes through a standard optical cleaning process before each measurement. In a clean room facility it is treated with acetone and isopropanol. The installation of the substrate into the experimental setup under the usage of rubber gloves was carried out as quickly as possible after the cleaning process to avoid contaminations of dust. Prior to the sealing of the probe chamber the substrate has been carefully cleaned with dry nitrogen gas.

The suspension should interact as less as possible with the sample since a transfer of energy from the sample to the suspension would result in additional damping. Different suspension systems have been proposed: the suspension of the substrate by means of a wire or ribbon as a pendulum [105], by clamping it between nodal points [106] or even balancing it on a hemisphere under certain conditions [107]. We focused on the pendulum suspension. The material of choice for the suspension wire loop is tungsten due to its appropriate mechanical properties like its high tension loading capability of up to 3.55 GPa [8]. The tungsten wire is polished with diamond paste

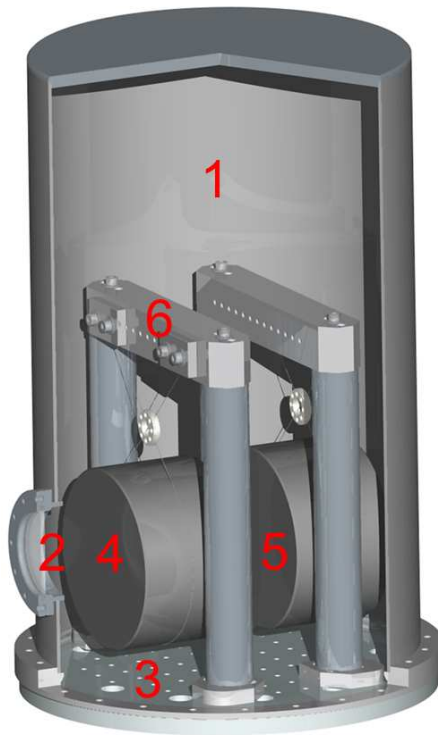


Fig. 4.2: Schematic of the probe chamber [103]. 1 - probe chamber, 2 - optical window, 3 - experimental platform, 4 - Q substrate, 5 - thermometry substrate, 6 - suspension system.

to smooth sharp-edged grooves introduced by the production process and afterwards cleaned with acetone and isopropanol. The wire's diameter is chosen to be preferably thin, such that the stress under load of the substrate is higher than 50% of the rupture stress. This choice originates in the relationship between stress and dissipated energy in the suspension wire. The dilution factor expresses this behavior quantitatively. For further information see, e.g, the work of Cagnoli et al. [108]. Close above the substrate the wire is fixed with an aluminium clamp in a crossed position. To provide a stable configuration which is essential for cryogenic measurements the crossing point is located in the middle of the clamp. The length of the wire should be chosen in a way that resonances of the suspension do not coincide with excited resonances of the substrate. For further information see the work of Nawrodt et al. [99].

Experiments show, that the location of the wire on the circumference is crucial for the measurement of high Q factors. Especially, a position that symmetrically divides the crystal into halves seems advantageous. A further influence on the measured Q factor exists in tilting of the substrate in the wire loop. A tilting of few arc minutes may reduce the Q factor.

The sample is excited to resonant vibrations by means of an electrostatic actuator. This non-contact method avoids additional losses due to mechanical contact. This actuator consists of a comb-like structure on a printed circuit board. By applying a high voltage (up to 1600 V) with an adequate frequency the test sample is excited to its resonant modes. For several reasons it makes sense to determine the resonant frequencies and

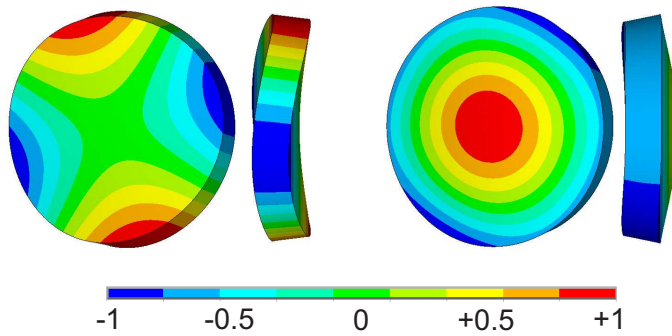


Fig. 4.3: Front and side view of two mode shapes. The colours indicate the displacement in direction of the cylinder axis. Red and blue areas indicate maximum displacement whereas green areas are motionless. The coloured chart represents the displacement normalized to the highest value of the particular mode.

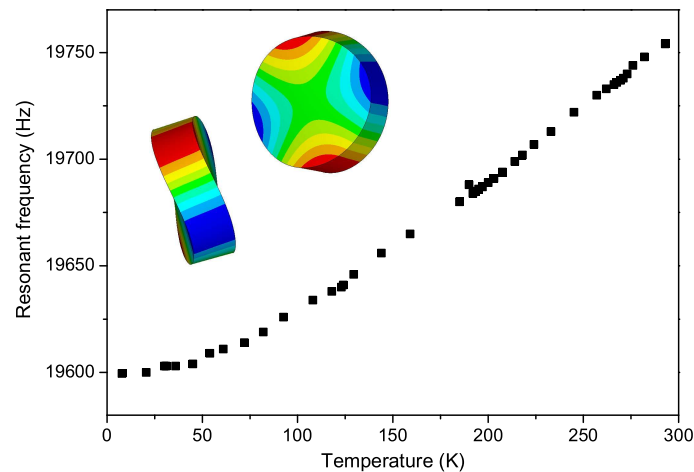


Fig. 4.4: Resonant frequency of a crystalline quartz sample (74.8 mm in diameter and 24.2 mm thick) versus temperature (pictures of mode shape included).

mode shapes to be expected by calculations before starting the measurement. Modes with high Q factors have a very narrow resonance width which makes them difficult to locate the resonant frequencies experimental. For the readout of the oscillations as well as a selection of characteristic modes the knowledge of the mode shape is essential. Therefore, the resonant frequencies and mode shapes have been determined by using the Finite Element Analysis (FEA) based software ANSYS [36]. For background reading on FEA the work of Bathe is recommended [109, 110]. Fig. 4.3 shows exemplarily two calculated mode shapes. The displacement in direction of the cylinder axis is illustrated by means of a contour plot. Since the resonant frequency changes in general with temperature this dependence can also be used to determine the temperature contactlessly. An example of the change of the resonant frequency with temperature is shown in Fig. 4.4. The magnitude of the excited oscillation amplitude depends on the dielectric properties of the substrate material. For crystalline quartz, silicon, CaF_2 and fused silica amplitudes of 0.2 nm to 1000 nm are achieved. A window in the cryostat permits the usage of a Michelson-like interferometer for the readout of the

vibration amplitude. The used laser vibrometer was built by SIOS [111]. It has a resolution of about 0.1 nm up to a frequency of 500 kHz. Thus, the readout is also designed to be free of contact to the sample allowing for higher sensitivity.

An amplitude ring-down method is most suitable to determine Q factors of higher than 3×10^4 for resonant frequencies of about 10 kHz. After removing the driving electric field the subsequent amplitude ring-down is recorded. From the 1/e-ring-down time τ_d of the amplitude it is possible to calculate the mechanical Q factor by using the relation

$$Q = \pi \cdot f_0 \cdot \tau_d, \quad (4.1)$$

where f_0 is the resonant frequency. Assuming a resonant frequency of 10 kHz and a Q of 10^8 a ring-down time of 53 min is expected. This example demonstrates the need of a high sensitivity setup in a long-term temperature-stable and undisturbed environment.

For Q factors of up to 10^6 the determination of the Q by recording the resonance curve is appropriate. The Q factor is then given by

$$Q = f_0 / \Delta f_0. \quad (4.2)$$

Δf_0 is the width of the resonance peak, meaning the distance in frequency between the points where the amplitude has decreased to $1/\sqrt{2}$ of its maximum value. We mainly deal with low mechanical losses where the width of the resonance peak is very small. Therefore, the ring-down method is mostly applied.

The optimization of the suspension system follows with regard to the determined decay time and Q factor as the last step. For isotropic materials this step can be skipped as rotations of the substrate in the wire loop leave the Q factors unchanged. The mode shape is self-aligned with respect to boundary conditions minimizing friction loss. In contrast, in anisotropic materials the mode shape rotates with the structure coordinate system (Fig. 4.5). Depending on the coupling of the displacements of the substrate to the wire the Q factor varies with orientation of the substrate in the wire loop [112]. To find the highest possible Q factor of the substrate in this suspension system the substrate is rotated by small angles (Fig. 4.6a)). The position corresponding to the highest Q factor is that where the least energy is transferred from the substrate to the suspension. For results on the variation of the Q factor with angle of rotation see Fig. 4.6b). The starting position was arbitrarily chosen. The readout of all Q measurements belonging to the same rotation angle was done on the same point on the surface. The substrate under investigation was made of CaF_2 (100) with a diameter of about 76.2 mm and a thickness of 75 mm (for further results see section 5.3). Although the angle was roughly estimated with up to 10° error, a symmetry

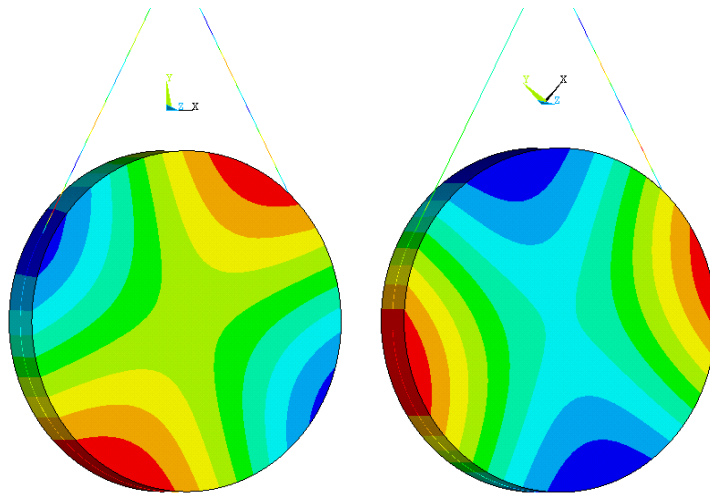


Fig. 4.5: Influence of a rotation of the substrate on the alignment of the excited mode shape of a crystalline quartz sample.

around 50° is clearly visible for all modes. This symmetry is reflected in the mode shapes. Thus, about 30 runs of rotation are necessary to start the Q measurements with the highest achievable Q factor in the suspension system.

The highest Q factor potentially measurable with our current setup for the modes with the lowest frequencies of about 10 kHz is about $Q \approx 3.3 \times 10^9$, if the total 1/e-ring-down time is recorded during the liquid helium holding time of the cryostat of about 30 hours. For clear signals, recording the ring-down to 90 % of the initial amplitude is sufficient. This increases the potentially measurable Q factor for a 10 kHz mode by factor 10 to $Q \approx 3.3 \times 10^{10}$. Due to the reproducibility of the measurement technique the Q factor is determined with an accuracy of 10 % to 20 %.

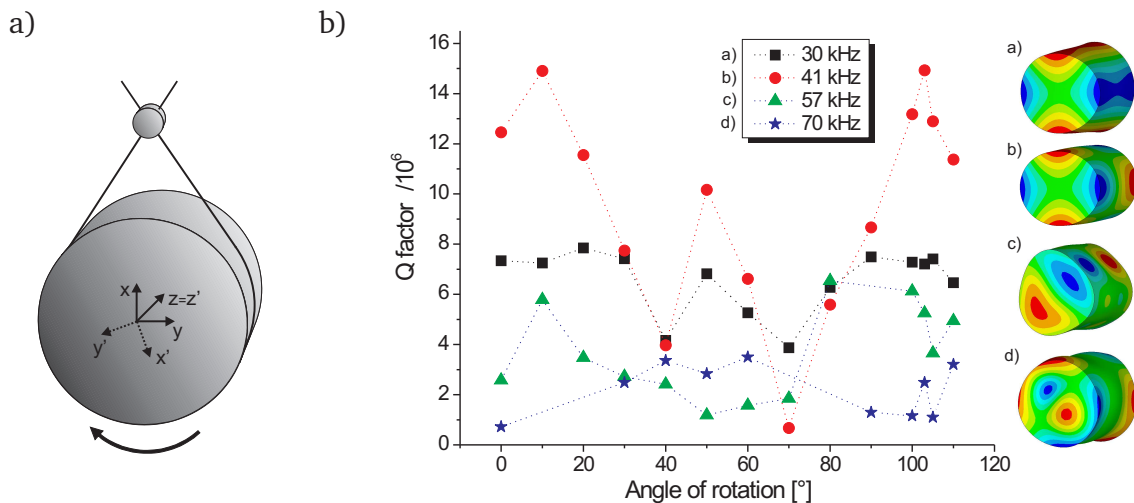


Fig. 4.6: a) Schematic view of the suspension system. Samples of anisotropic materials might have to be rotated in the wire loop to gain the highest Q factor possible in the suspension system. b) Q factor versus angle of rotation of the substrate in the wire loop. The dotted lines are drawn as guide line for the eye. The corresponding mode shapes are plotted on the right.

4.2 Parameters of the measuring system

Cryostat:

LN ₂ tank	59 l
LHe tank	49 l
Height of probe chamber	500 mm
Diameter of probe chamber	300 mm
Temperature of probe chamber	5 ... 325 K
Temperature stability	better than 0.3 K
He residual gas pressure	$< 10^{-3}$ Pa

Tab. 4.1: Parameters of the custom made cryostat [113].

Laser vibrometer:

Frequency range	0.1 ... 500 kHz
Amplitude	0.1 nm ... 10 μ m
Distance of probe to interferometer	(500 \pm 25) mm

Tab. 4.2: Parameters of the laser vibrometer [111].

5 Modelling of mechanical losses

Current IGWDs are operated at room temperature with test masses made from fused silica. Since mechanical losses are in general dependent on temperature, the suitability of fused silica as a test mass material also for future cryogenic IGWDs has to be proven. In this chapter it will be shown that fused silica is not suited for this purposes due to its amorphous structure. Further on, the mechanical losses of potential low-loss crystalline materials are analysed, especially in the low temperature range. For the modelling of the mechanical losses measured with CRA spectroscopy (see chapter 4) the methods acquired in chapter 3 are adopted. In particular, Eq. (3.114) has been used to fit the reciprocal of the measured Q values versus temperature. In the process, the loss curve has been decomposed into different loss contributions visible as clear damping peaks. An Arrhenius-like law (Eq. (3.84)) has been assumed for all relaxation times since it yielded the best results for relaxation peaks caused by thermal phonons. The relaxation strength Δ , the relaxation constant τ_0 and the activation energy E_a have to be determined for each peak. At first, the peak with dominating contribution has been fit. The quality of all other fits depend on the accuracy of this first fit. According to Eq. 3.39 the relaxation strength has been initially chosen to be twice the maximum value of the measured loss. The variation of E_a and τ_0 affects the position of the peak on the temperature scale, and its shape. The values of τ_0 are similar for relaxation processes of the same kind (e. g., induced by thermal phonons or point defects). The fit process is quite complex since all measured loss curves for one sample respectively the same material have to be taken into account. The underlying reason is that the symmetrized stresses and strains responsible for the occurrence of relaxation, mentioned in section 3.2.1 contribute to many mode shapes and, therefore, the same relaxation processes should be visible to some extent in many loss curves. It is advisable to start the fit process on the loss curve with the most clearly visible damping peaks and go in iterations through all curves.

5.1 Fused silica

Fused silica offers manifold properties that make it suitable as a substrate material for the test masses and therefore optical components of the current IGWDs operating at room temperature. The application of high laser powers for the reduction of photon shot noise requires a material with a low optical absorption at the used laser wavelength. Fused silica meets the demand with an absorption of less than 0.25 ppm/cm

for a very pure (OH reduced to less than 50 ppm) sample at the laser wavelength of 1064 nm [114]. As fused silica is a material of great relevance for the optics industry such high purity grades can be achieved. Further, fused silica offers an attractive low thermoelastic noise in IGWD detection band at room temperature caused by its small thermal expansion coefficient of $4.9 \times 10^{-7} K^{-1}$ [115]. Also, the Brownian part of the thermal noise is very low since fused silica shows low mechanical losses at room temperature, i. e., high Q factors of up to 2×10^8 [116].

Now, fused silica should be examined regarding its mechanical properties for cryogenic IGWDs. As mechanical losses are in general temperature dependent, the undesirable effect can occur that a test mass material with high Q factors at room temperature changes to a low-Q material at low temperatures making it not applicable in cryogenic detectors. It has been found that Q factors of fused silica samples significantly decrease with decreasing temperatures. Early measurements used the so-called ‘resonant piezoelectric method’ and found a damping peak of fused silica at about 35 K [117] measured at a resonant frequency of 50 kHz. Other early works were performed at rather high frequencies far above the gravitational wave detection band (>500MHz) [118]. More recent investigations used Brillouin spectroscopy and concentrated on small samples (<1 cm³). Q factors of the order 10^3 were achieved [119, 120]. We reexamined fused silica by CRA spectroscopy which is described in chapter 4. On the one hand, this method permits high measurement accuracies by realising excitation and readout without mechanical contact. On the other hand, we used artificially produced samples with a high grade of purity allowing for the resolution of narrow damping structures in the temperature spectrum. We also used rather large samples having an increased relevance for test mass applications in gravitational wave detectors.

In Fig. 5.1 the reciprocals of the measured Q factors are plotted versus temperature. The data have been taken on a cylindrical substrate made of fused silica [121] with a diameter of 76.2 mm and 12 mm thick. The excited mode shapes are also visualised in Fig. 5.1. A large, broad damping peak occurs. No strong dependence of the peak shape or height on the mode shape is visible. The mechanical losses increase about 4 orders of magnitude from room temperature to 30 K finally resulting in a value of 10^{-3} at 30 K. To rule out the potential influence of thermoelastic damping, thermoelastic losses in fused silica have been estimated by using Eq. (3.68), shown in Fig. 5.2. Since the thermoelastic losses are lower than 10^{-13} over the whole temperature spectrum, they are negligible.

Fused silica is a material with high structural variation. The structural unit, a silicon atom surrounded by 4 oxygen atoms in the form of a tetrahedron, equals that of crystalline quartz. But the variation in bond lengths and bond angles generates

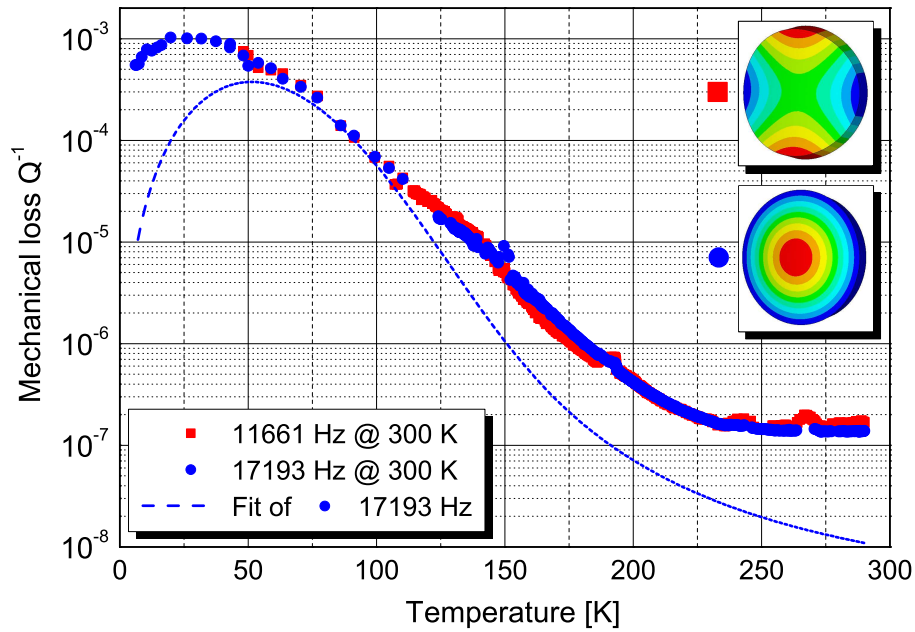


Fig. 5.1: Reciprocal of the measured Q factors versus temperature for a fused silica substrate 76.2 mm in diameter and 12 mm thick. The dashed line represents a theoretical model for a dominant loss mechanism at intermediate temperatures which was fitted to the measured data for the mode with frequency 17193 Hz at 300 K. Details of the fit parameters are given in the text. Insets show the calculated mode shapes of the measured modes. The colours indicate the displacement in direction of the cylinder axis. Red and blue areas indicate maximum displacement whereas green areas are motionless. For the numerical simulations the FEA based software ANSYS [36] was used. The essential material parameters have been taken from SCHOTT Lithotec [121].

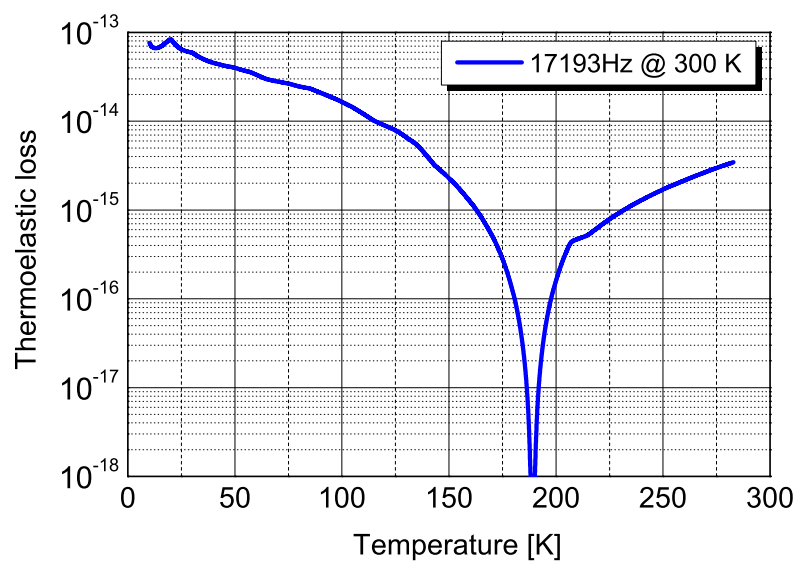


Fig. 5.2: Approximation of thermoelastic losses in fused silica.

its amorphous character. This variation also seems to be the cause for the observed large, broad damping peak [91, 118, 122, 123]. In general one can assume that a vast number of different bonding configurations with different bonding energies exist. Considering the simplest case, the energy landscape of two configurations can be described by two valleys of an asymmetric double-well potential. The wall height between them is given by the stiffness of the directed bonding forces and can be overcome by thermal energy.

Three possibilities of the microscopic origin of the mechanical losses have been proposed:

- (1) transverse movement of oxygen atoms between two potential minima resulting in flipping of the bond [124]
- (2) motion of oxygen atoms in the direction of the bond between two potential minima [125]
- (3) rotation of the SiO_4 tetrahedrons by small angles [126].

Due to the amorphous character of fused silica a wide variation in the height of the energy barrier occurs and therewith a distribution in activation energies. An activation energy E_a is needed to overcome the barrier between the two configurations. A stress-induced transition between configurations with a following removal of energy from the acoustic wave can be treated by the model described in section 3.4.1. For a particular activation energy the temperature dependent relaxation time of the corresponding relaxation process is given by the Arrhenius-like relation (3.84). A distribution in relaxation times requires integrating over all contributions at a fixed temperature [127]. Assuming small losses ($\Delta \ll 1$) the contribution due to a single anelastic process is given by Eq. (3.38). The mechanical loss due to a superposition of loss processes with varying relaxation time can then be written as

$$\phi \approx \Delta \int_{-\infty}^{\infty} \Psi(\ln \tau) \frac{2\pi \cdot f \cdot \tau}{1 + (2\pi \cdot f \cdot \tau)^2} d \ln \tau. \quad (5.1)$$

with the following normalised distribution function

$$\int_{-\infty}^{\infty} \Psi(\ln \tau) d \ln \tau = 1. \quad (5.2)$$

The distribution is linearly related to $\ln \tau$, as $\ln \tau$ is linearly related to the activation energy [127]. Assuming a Gaussian distribution of the barrier heights and therewith also of the activation energies, the relaxation times are lognormal distributed,

$$\Psi(\ln(\tau/\tau_m)) = \frac{1}{\beta\sqrt{\pi}} \exp\left[-(\ln(\tau/\tau_m)/\beta)^2\right], \quad (5.3)$$

where τ_m is the most probable value of τ and β is the half-width of the Gaussian distribution at the point where Ψ falls to $1/e$ of its maximum value. Since solely a variation in activation energies and not in the relaxation constant is assumed, β is chosen to be temperature dependent, $\beta = \beta_c/T$ [127], where β_c is a constant.

The measured data recorded for the resonant frequency of 17193 Hz at 300 K in Fig. 5.1 have been fit using Eqs. (5.1) and (5.3) with the following parameters: $\tau_0 = 1 \times 10^{-13}$ s, $\beta_c = 700$ 1/K and $\tau_m = \tau_0 \times \exp(35.3 \text{ meV}/k_B T)$. The parameters used for τ_0 and τ_m are those reported in the work of Hunklinger [118], and also successfully describe our measurement data between 50 K and 100 K, see the dashed line in Fig. 5.1. Differences to the measured values at other temperatures are possibly due to the following mechanisms. For temperatures above 225 K, phonon-phonon interactions are plausible. Phonon-phonon interactions are expected to play a similarly important role in both, fused silica and crystalline quartz (see section 5.2 respectively Fig. 5.3), which is indeed found in (Fig. 5.1). The deviations between 100 K and 225 K and below 50 K are assumed to be due to other loss mechanisms. At 50 K as well as at about 100 K, a small kink in the curve is visible indicating additional damping peaks. Below 50 K a damping peak has been observed by Hunklinger [118] at far higher resonant frequencies (507 MHz and 930 MHz). Due to the much higher frequencies the damping peaks were clearly separated from each other and observed as distinct peaks. Note that a loss peak caused by relaxation processes moves with decreasing frequency to lower temperatures. Peaks having different parameters entering the relation for the relaxation time are not equally shifted. Thus, the peak observed by Hunklinger is likely to appear in our measurements below 50 K partially covered by the damping peak due to structural variations since the resonant frequencies are lower. According to the work of Hunklinger [118] it is caused by relaxation processes of the two-level-systems by resonant absorption or emission of thermal phonons. The origin of the damping peak at about 150 K is not known to our knowledge. An analysis of this problem would require a clearer separation of this damping peak from our fitted damping peak at about 80 K. This could be achieved by measurements at lower frequencies which are, however, experimentally rather challenging.

In summary, fused silica is well suited to realise low thermal noise floors in the signal band of the *current* working IGWDs since it offers low mechanical losses. For a *future* generation of *cryogenic* IGWDs, however, fused silica is not appropriate as the thermal noise would be higher than that of the current IGWDs [128].

In general, amorphous materials show broad loss peaks, due to the variation of structural properties and thus the variety of relaxation parameters. A damping curve with at most narrow peaks should be therefore generated by a material with mainly single relaxation processes caused by weak deviations from a periodic crystal structure with

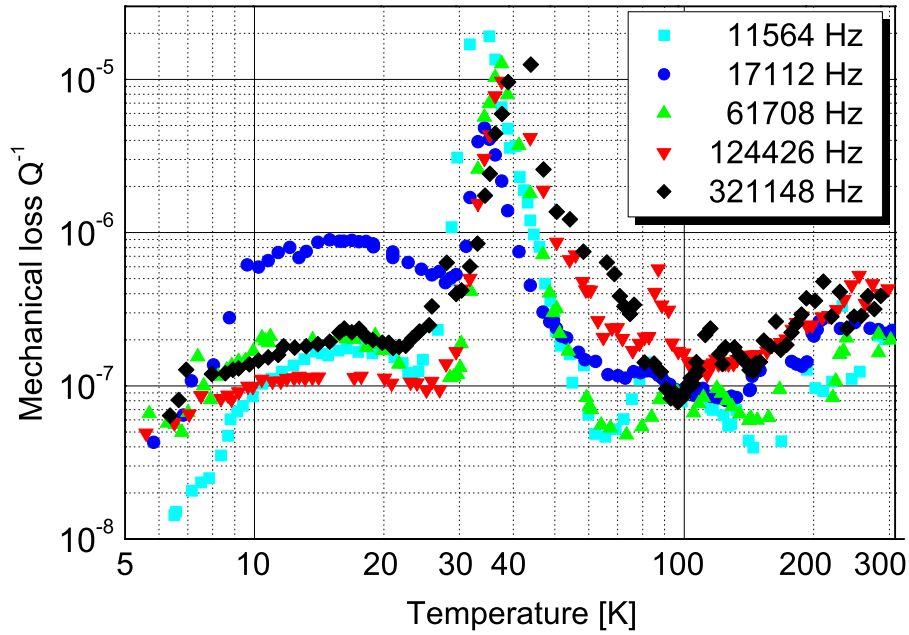


Fig. 5.3: Reciprocal of the measured Q factors versus temperature for a z-cut crystalline quartz substrate (74.8 mm in diameter and 12.05 mm thick). The stated resonant frequencies are the data at 300 K.

long range order. At first, fused silica's crystalline counterpart, crystalline quartz, is considered.

5.2 Crystalline quartz

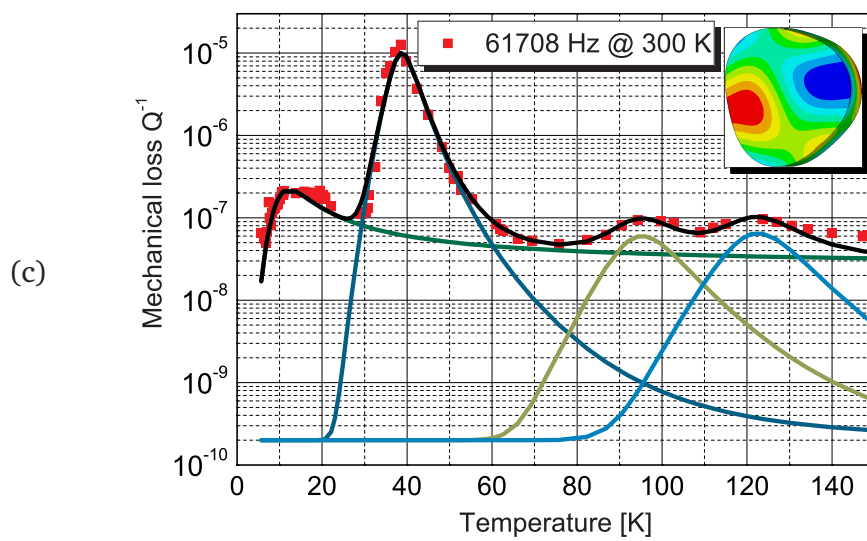
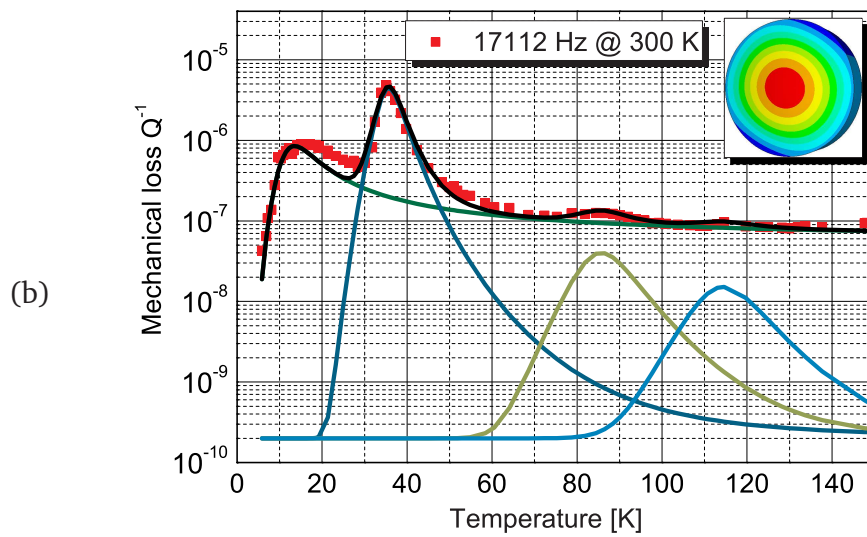
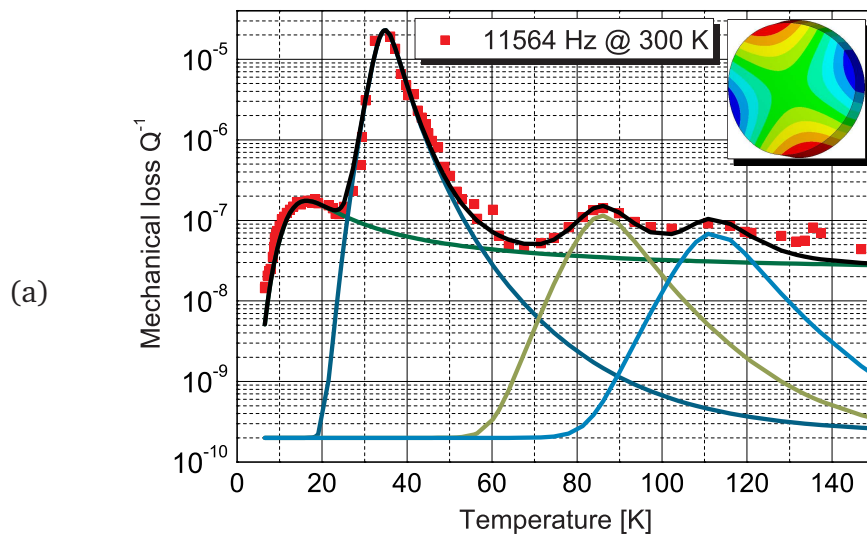
Like fused silica, crystalline quartz shows a low optical absorption coefficient of 3.4 ppm/cm at 1064 nm [129]. This fact promises a similar low shot noise level. To study the mechanical properties of crystalline quartz at low temperatures cryogenic Q measurements have been performed on samples of different size and cut. A further important aspect of the studies on crystalline quartz is that this material is fairly well-known due to the broad research, particularly in the 1950s and 1960s (see, for instance, [60, 130–137]). Thus, a test of our new method of mechanical spectroscopy, CRA spectroscopy (see chapter 4), is possible [138].

The first samples of crystalline quartz under investigation were z-cut, i. e., oriented with the c- or z-axis in direction of the cylinder axis. Fig. 5.3 shows the reciprocal of the Q factors of a substrate, 74.8 mm in diameter and 12.05 mm thick, measured at different resonant frequencies in the temperature range from 6 K to 300 K. Several damping peaks are visible. Especially for the largest loss peak the following behaviour is clearly observable. The temperature of the peak maximum shifts with increasing frequency to higher temperature values. This is an indication for the oc-

RELAX. PEAK	FREQUENCY @ 300 K (Hz)	T_{peak} (K)	Δ ($\times 10^{-8}$)	τ_0 (s) ($\times 10^{-14}$)	E_a (meV)
1. (olive)	11564	15	35	80×10^6	4
	17112	14	170	30×10^6	4
	61708	14	44	15×10^6	3
	124426	11	24	30×10^6	1.7
	321148	12	38	9×10^6	2
2. (blue)	11564	34	4600	30	53
	17112	35	900	80	50
	61708	39	2000	10	57
	124426	41	2500	20	54
	321148	45	2500	30	51
3. (light green)	11564	86	23	44	128
	17112	86	8	44	124.5
	61708	95	12	44	128
	124426	100	24	44	128
	321148	106	< 1	44	128
4. (cyan)	11564	112	14	4	190
	17112	114	3	4	190
	61708	122	13	4	190
	124426	127	15	4	190
	321148	138	20	4	195
5. (violet)	321148	118	30	1	180
6. (orange)	124426	57	80	50	73
	321148	64	120	100	72
7. (magenta)	124426	75	20	50	95
	321148	85	10	70	99

Tab. 5.1: Parameters of the relaxation peaks in Figs. 5.4(a)-(e) gained by a fit procedure using Eq. (3.114). The background loss Q_{bg}^{-1} is max. 2×10^{-10} .

currence of frequency-dependent relaxation processes in the material. The damping curves have been separated into Figs. 5.4(a)-(e) for a more detailed examination. The following consideration is important for the test of our measurement method. If our measurements reflect the inner damping processes, modes with similar mode shapes measured on different substrate geometries should exhibit similar relaxation parameters. Therefore, the damping behaviour of the first mode (Fig. 5.4(a), often called 'butterfly' because of the resemblance of the wing movement) has also been studied on a second sample, about twice as thick (24.2 mm) as the first one. Both samples were cut out of the same crystal boule [141]. The results of the Q measurement on the second sample are shown in Fig. 5.5 while the change of the resonant frequency with temperature is plotted in Fig. 4.4 already. In fact, this measurement has been performed earlier. Since then, the measurement method had been improved. Thus, the data are more dense for the thinner sample than for the thicker one. Two



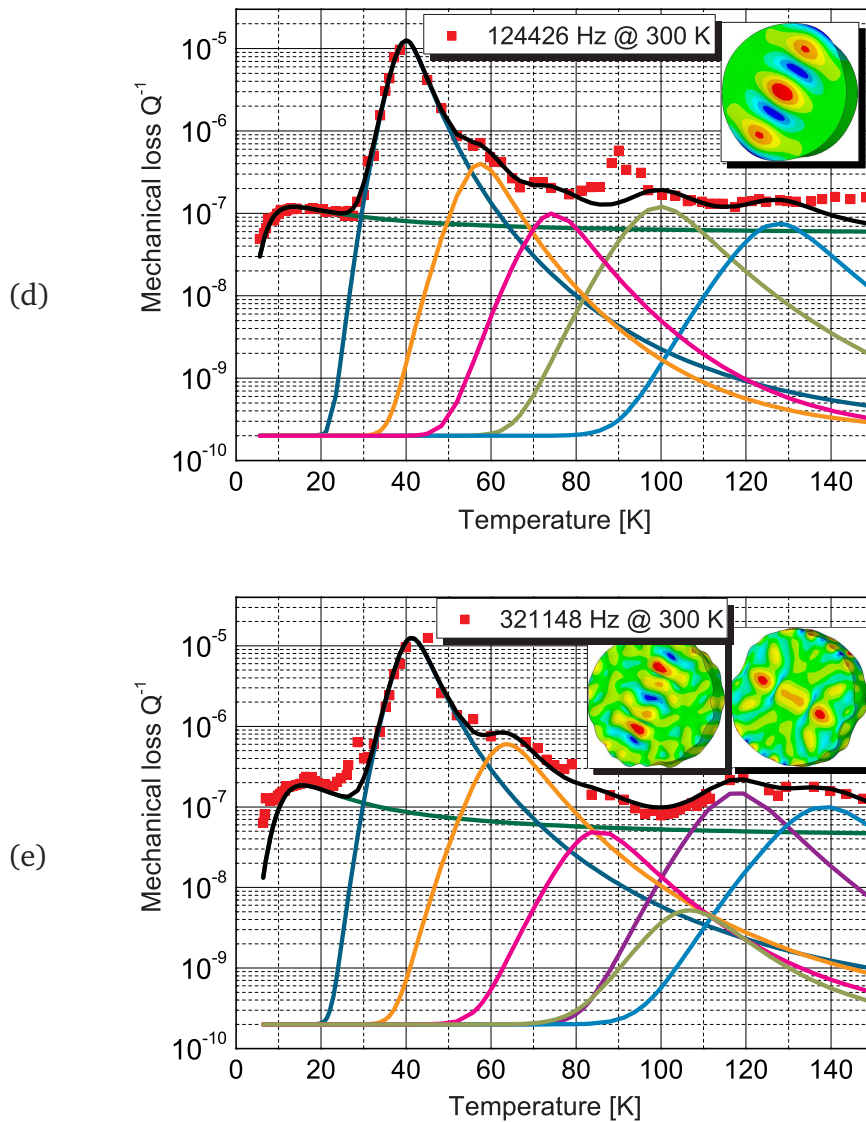


Fig. 5.4: Reciprocal of the measured Q factors versus temperature for a z-cut crystalline quartz sample (74.8 mm in diameter and 12.05 mm thick) measured at the resonant mode with the frequency of (a) 11564 Hz, (b) 17112 Hz, (c) 61708 Hz, (d) 124426 Hz, and (e) 321148 Hz at 300 K. Insets show the calculated mode shapes of the measured modes. The essential material parameters have been taken from Smakula et al. [139] (density) and Bechmann [140] (elastic coefficients). For 321148 Hz the correlated mode shape is not clear as the accuracy of the calculations decreases with increasing frequency as well as the mode density increases. Two most likely mode shapes are shown. The damping peak fit curves are marked with different colours. For their parameters see Tab. 5.1. The total damping curve is drawn in black.

RELAX. PEAK	FREQUENCY @ 293 K (Hz)	T_{peak} (K)	Δ ($\times 10^{-8}$)	τ_0 (s) ($\times 10^{-14}$)	E_a (meV)
1. (dark green)	19754	15	25	60×10^6	3.3
2. (dark blue)	19754	36	460	300	46

Tab. 5.2: Parameters of the relaxation peaks in Fig. 5.5 gained by a fit procedure using Eq. (3.114). The background loss Q_{bg}^{-1} is max. 2.8×10^{-8} .

distinct peaks dominate the damping curves, the first with a maximum at about 15 K and a second, higher peak at about 35 K. These peaks also occur for 4 other modes measured at the first sample shown in Figs. 5.4(b)-(e), but shifted with frequency. As written before, the shift of the temperature of the damping maximum with frequency is an indication for relaxation processes occurring in the material.

There are different methods of calculating the relaxation parameters. One is to fit the damping curves using Eq. (3.114). Another is to use an Arrhenius plot, if the relaxation times follow the Arrhenius-like law Eq. (3.84). The mechanical loss (Eq. (3.38)) is maximum when the angular frequency of the elastic wave is equal to the reciprocal of the relaxation time:

$$2\pi \cdot f \cdot \tau = 2\pi \cdot f \cdot \tau_0 \cdot e^{\frac{E_a}{k_B T_{peak}}} = 1, \quad (5.4)$$

which results in

$$\ln(2\pi \cdot f) = -\ln(\tau_0) - \frac{E_a}{k_B} \frac{1}{T_{peak}}. \quad (5.5)$$

The natural logarithm of the frequency of the elastic wave displays a linear correlation to the reciprocal of the temperature where maximum damping occurs. This can be shown graphically in the Arrhenius plot. The activation energy can be determined from the slope of the linear function, and the relaxation constant from the offset [142]. The Arrhenius plot is only applicable when the peak maxima are clearly visible. Therefore, it was possible to create an Arrhenius plot for the second damping peak (dark blue line), which has fairly good visible peak maxima, measured at the first sample (Fig. 5.7). The parameters gained from the Arrhenius plot are: $\tau_{0,2} = 6 \cdot 10^{-13} \text{ s}$, $E_{a,2} = 50 \text{ meV}$. The parameters shown in Tab. 5.1 obtained by fitting the damping curves in Figs. 5.4(a)-(e) using Eq. (3.114) are consistent with them. All relaxation times have been assumed to follow an Arrhenius-like law Eq. (3.84). According to the superposition principle of mechanical losses, the total damping curve has been decomposed into contributions (displayed by coloured lines) due to single anelastic processes of different origin. An advantage of the Arrhenius plot compared to the fitting method is the rapid calculation of the relaxation parameters. But mostly,

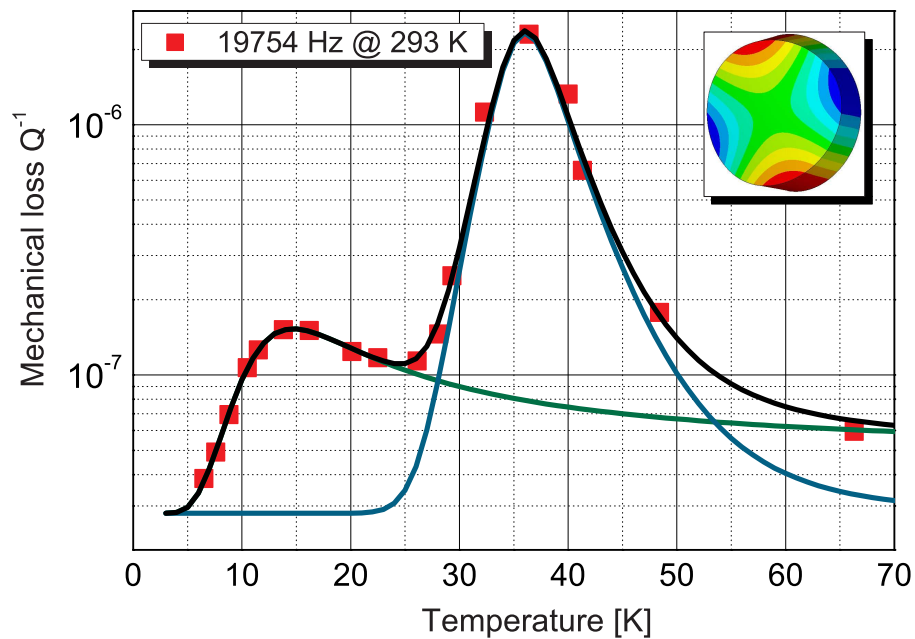


Fig. 5.5: Reciprocal of the measured Q factors versus temperature for a z-cut crystalline quartz sample (74.8 mm in diameter and 24.2 mm thick) measured at the resonant mode (picture of mode shape included) with the frequency of 19754 Hz at 293 K. Squares: measured data; black line: fit of measured data, i.e., sum of the fits of relaxation peak 1 (green) and 2 (blue). For the fit parameters see Tab. 5.2.

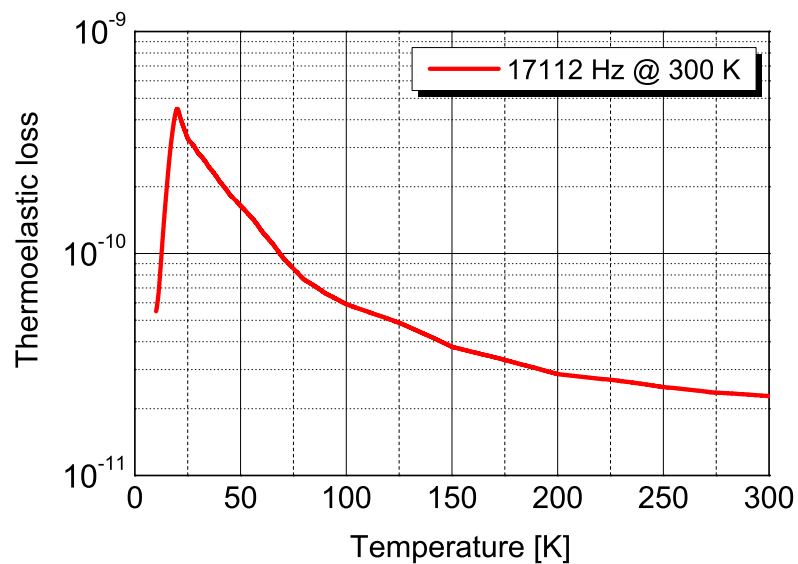


Fig. 5.6: Approximation of thermoelastic damping in crystalline quartz.

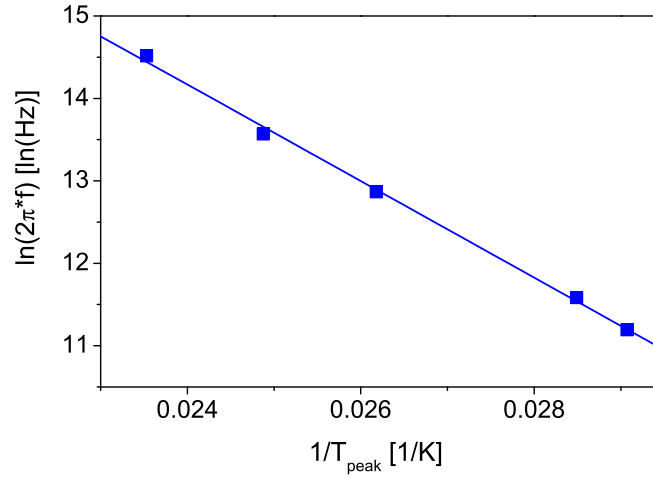


Fig. 5.7: Arrhenius plot of the second damping peak (at about 40 K) of a z-cut crystalline quartz sample (74.8 mm in diameter and 12.05 mm thick).

the maxima of the relaxation peaks cannot be determined with sufficient accuracy. The background losses Q_{bg}^{-1} (for details see section 3.5) are always upper limits and could not be determined with greater accuracy due to the temperature limit of our experimental setup. They are chosen according to the shape of the first damping peak which underlies the damping curve over the whole temperature range. The error of the Q measurements can be estimated to be about 10% (see chapter 4). The height of the squares of the measuring points is equal to the height of the error bars. The error in estimating the relaxation strength is of similar magnitude. The errors in determining the activation energy and relaxation constant are smaller, about 2%. The relaxation parameters obtained for the two damping peaks measured at the 'butterfly' mode of the second substrate are given in Tab. 5.2. They match the parameters received for the same mode shape of the first sample. This demonstrates that the damping peaks are due to an internal process and not due to the circumstances of measurement. A potential influence of the thermoelastic damping could be ruled out. The approximation of the thermoelastic losses in crystalline quartz using Eq. (3.68) is shown in Fig. 5.6. The estimated maximum loss occurring at about 20 K is of the order of magnitude of the background losses and, thus, is negligible.

Two additional damping peaks are visible at the higher temperature range for the thinner substrate, depending on frequency, at about 85 K to 110 K and 110 K to 140 K, respectively (relaxation peaks 3-4 in Tab. 5.1). Higher modes measured (Fig. 5.4(d)-(e)) reveal further damping peaks (relaxation peaks 5-7 in Tab. 5.1).

The first relaxation peak (dark green line) can be explained by interactions of the acoustic vibrations with thermal phonons. The background of dissipation due to interactions of the acoustic wave with thermal phonons is described in section 3.3.2. Since the relaxation peak is clearly visible in our measurements of crystalline quartz,

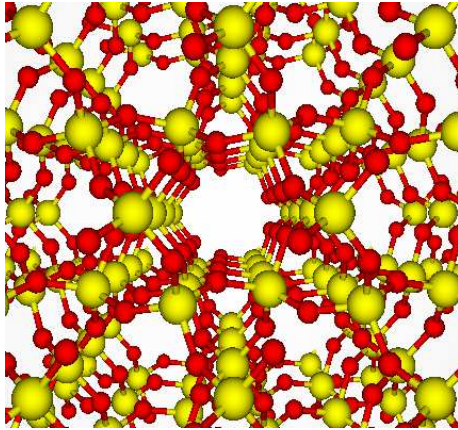


Fig. 5.8: Structure of crystalline quartz. View into the so-called 'c-axis channel'. Yellow atoms: silicon, red atoms: oxygen.

both regimes, Landau-Rumer as well as Akhieser, have to be taken into account. The relaxation strength was assumed to be constant and the relaxation times have been model because the assumption agreed well with the measured data. The relaxation time describing the phonon-phonon peak at room temperature of $\tau_1 = 6 \times 10^{-7} \text{s} \cdot \exp(3.3 \text{meV}/(k_B \cdot 300\text{K})) = 6.8 \times 10^{-7} \text{s}$ matches well with the lifetime of the 3.4 THz longitudinal phonons propagating in a y-cut quartz crystal of about $4 \times 10^{-7} \text{s}$ [143]. Small differences in the relaxation constants and activation energies are due to, e. g., fit errors and errors in the Q measurements as mentioned above. Nevertheless, the lack of a temperature-dependent relaxation strength may be responsible for the small deviation of the fit curve from the measured data as seen in Fig. 5.4(b). Since the phonon-phonon interactions contribute to the entire damping curve this might have an influence on the parameters of other relaxation processes in the fit procedure.

The second relaxation peak (dark blue line) is caused by impurities introduced during the crystal growth [136, 142]. Aluminium atoms present in the growth solution substitute silicon atoms [142]. The resulting Al^{3+} ions require charge-compensating ions which are realised by alkali ions in an alkali-rich growth environment or by protons. The ions are located nearby the Al^{3+} site in the so-called 'c-axis channels' (Fig. 5.8). Their defect symmetry is triclinic [98]. The potential energy landscape can be described by double-well potentials (Fig. 5.9). A stress-induced motion of the alkali ions from one equilibrium position to another removes energy from the acoustic wave. Maximum loss occurs when the angular frequency of the acoustic wave is equal to the jump frequency of the alkali ions. These damping peaks can be adjusted by sweeping (electrodifusion) or irradiating the crystal [144–148]. The alkali ions involved in the relaxation process causing the second peak are sodium ions [142]. The fit parameters are in agreement with previous works [131, 147, 149, 150]. The sodium concentration of our samples is below the detection limit of ICP-OES of $3 \mu\text{g}$ per g. Therefore, other methods than ICP-OES with higher sensitivity like ICP-MS (Inductively Coupled Plasma Mass Spectrometry) [97] should be applied to determine

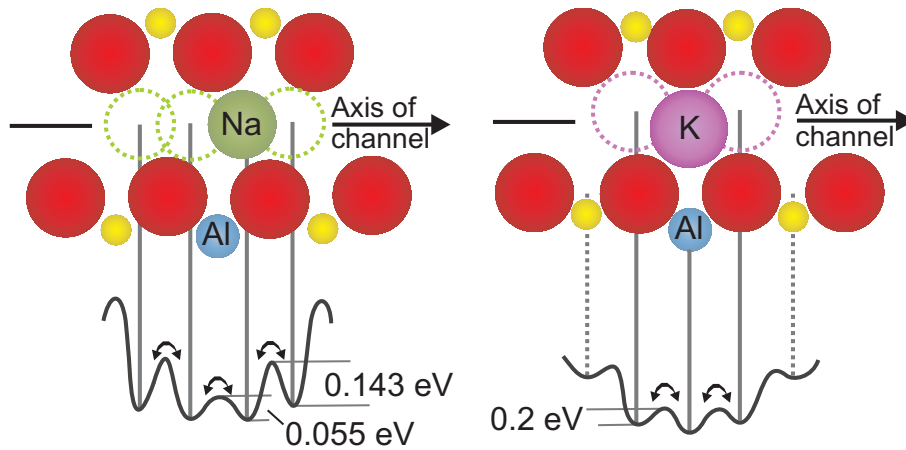


Fig. 5.9: Double-well potentials along c-axis channel in crystalline quartz [66]. Yellow atoms: silicon, red atoms: oxygen.

the defect concentration in the future. For an estimation of the differences in strains per unit concentration of defects in two principal directions in the crystal see section 3.4.1.1.

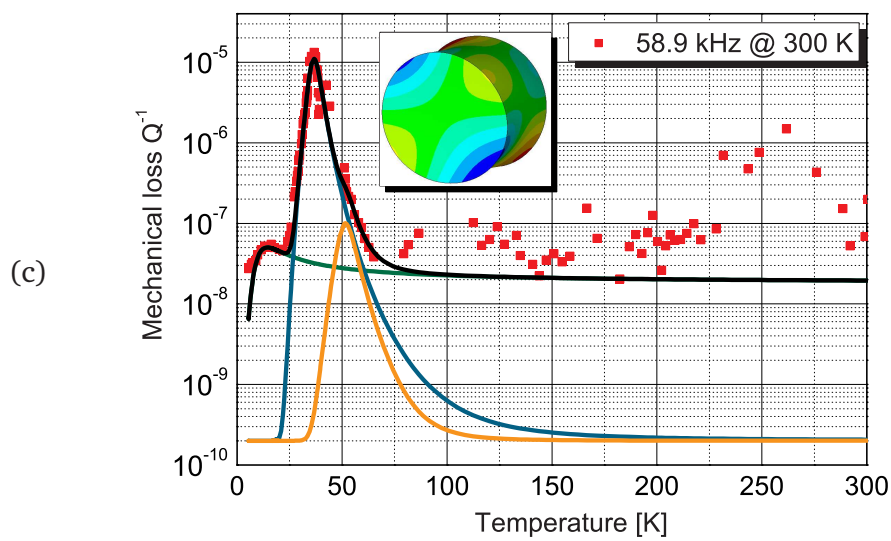
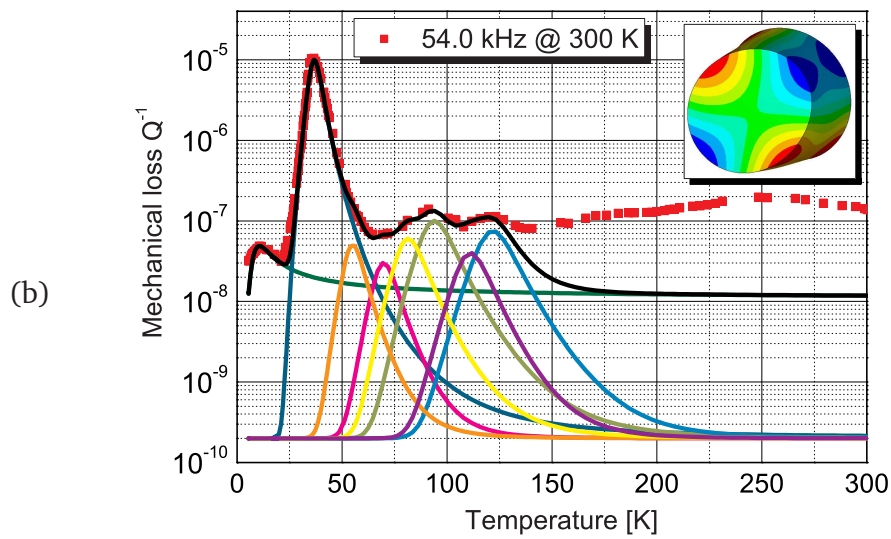
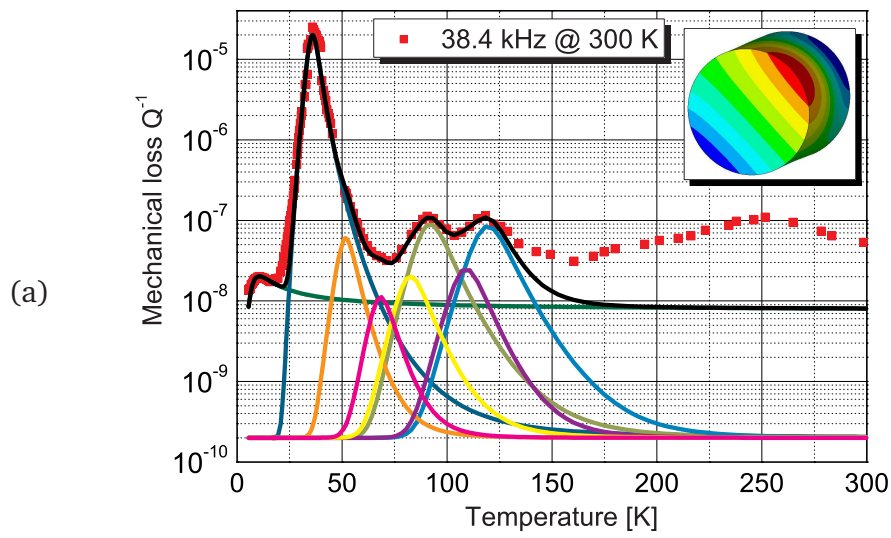
The relaxation process underlying the third peak (light green line) in Figs. 5.4(a)-(e) is likely due to sodium ions, too. The parameters are in remarkable agreement with that reported by Martin [147, 150]. This peak disappears only in the highest-frequency mode (321148 Hz at 300 K) as another peak covers it (violet line) here. The origin of this additional peak is unknown. Its relaxation parameters are similar to the fourth relaxation peak (light blue line). This damping peak may be caused by potassium ions [136, 142]. The two highest modes measured reveal two other damping peaks (orange and magenta lines). Their origin is unclear as they have, to our knowledge, never been observed before. According to the magnitude of the relaxation times and activation energies, further hopping processes of defects can be presumed. In combination with intensified Q measurements of resonant modes in this frequency region, a chemical analysis of the impurity content of the crystalline quartz and optical spectroscopy methods, e.g. via infrared spectroscopy, should provide further information. This information could support a theoretical interpretation of the source of the damping process and, thus, provide further information about the structure.

To study the mechanical losses in crystalline quartz dependent on the crystal cut, three samples have been produced from the same crystal boule. An x cut, a y cut and a z cut were shaped into cylindrical form, 45 mm in diameter and 50 mm thick. Due to time constraints - one measurement takes about one month - only the x cut was measured until the end of this work. The results of the Q measurements in the temperature range from 6 K to 300 K are shown in reciprocal form in Figs. 5.10 (a)-

(f). Similar damping peaks like for the z cut appear. Their relaxation parameters have been gained by a fit procedure also using Eq. (3.114). The results are listed in Tab. 5.3. All damping peaks except no. 5 in Tab. 5.3 measured at the x cut are existent for the x-cut sample as well as the z-cut crystal. The variation of the relaxation parameters for the x cut compared to that of the z cut is much lower than the variation of the parameters measured at one cut with mode shape, for both cuts. However, an influence of the different geometry of the x-cut substrate on the relaxation strength could not be excluded. The planned measurements on the z-cut crystal of identical geometry will answer this question.

The influence of the mode shape on the relaxation strength of the particular relaxation process can be determined by comparing mode shape and fit parameters. The first mode (Fig. 5.4(a)) and second mode (Fig. 5.4(b)) of the z-cut sample have been selected for reasons of clarity. They exhibit distinct mode shapes. The first mode resembles a butterfly, the second oscillates like a drum. The 'drum' mode shows the highest relaxation strength concerning the phonon interaction damping mechanism of all modes measured at the z cut. However, the influence on the alkali ions located in the c-axis channels is much weaker compared to the other modes measured. The 'butterfly' mode in particular shows a more than fourfold higher relaxation strength for the second relaxation peak (dark blue line) caused by stress-induced hopping of sodium ions. A plausible reason is that modes of longitudinal character rather stretch the crystal structure along the c-channels leaving the valleys in the double-well potential of equal height, while modes of shear character rather deform the potential in the channel. This description agrees with the selection rules given in section 3.4.1.2. According to them, only shear stresses and strains (i. e., of type II) contribute to relaxation processes in crystalline quartz, if considering only one defect species.

Summarising, the highest Q factor observed by us in crystalline quartz is 1×10^8 at 5 K. Above this temperature, higher Q values might be gained by sweeping or irradiating the crystal. The observed mechanical loss peaks could be well described by the models acquired in chapter 3. New relaxation peaks have been found. The variation of the relaxation parameters for x- and z-cut quartz is much lower than the variation of the parameters measured at one cut with mode shape, for both cuts. Experiments to study the effect of geometry on the relaxation strength are planned.



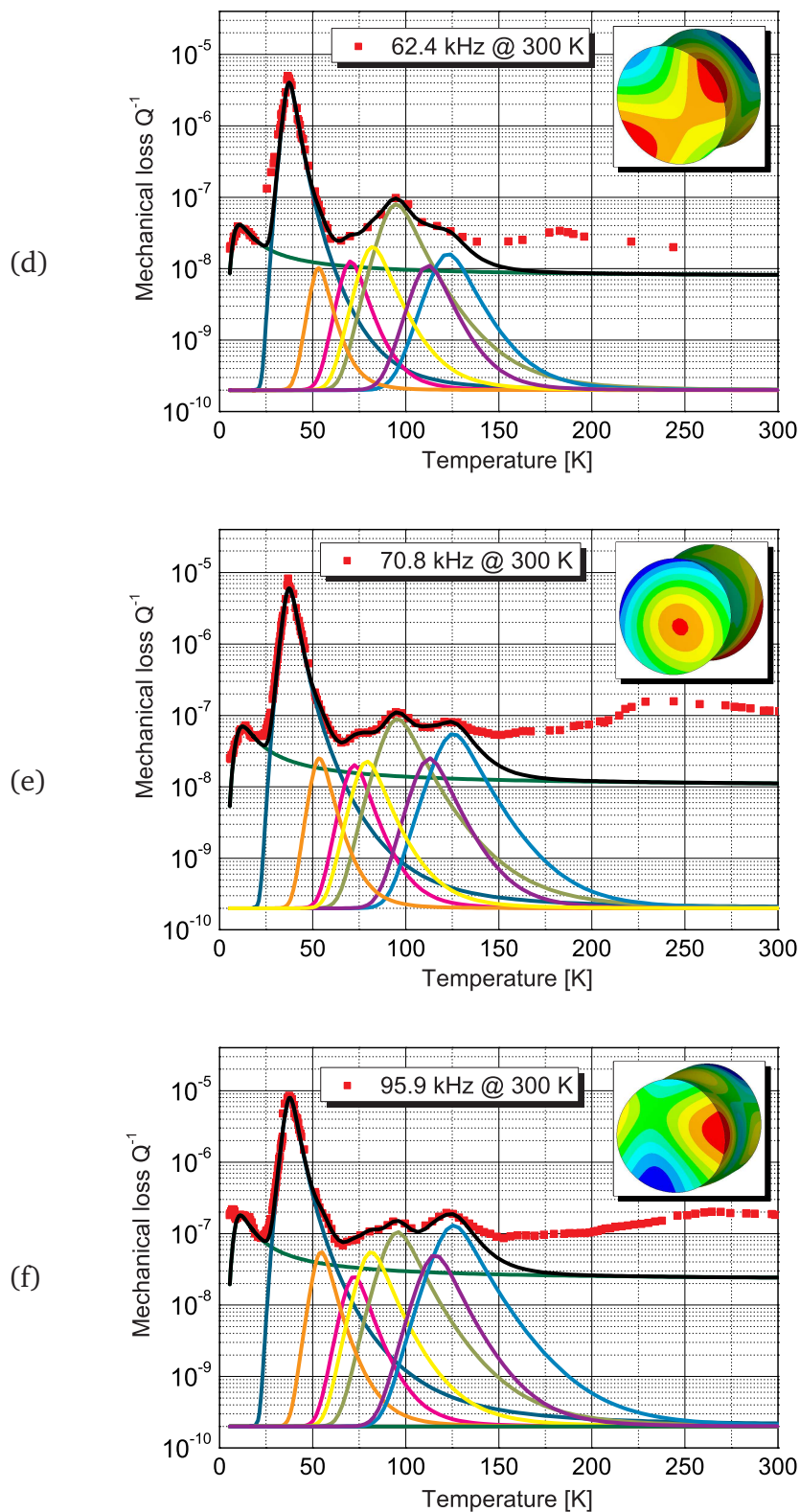


Fig. 5.10: Reciprocal of the measured Q factors versus temperature for an x-cut crystalline quartz sample (45 mm in diameter and 50 mm thick) measured at the resonant mode (picture of mode shape included) with the frequency of (a) 38.4 kHz, (b) 54.0 kHz, (c) 58.9 kHz, (d) 62.4 kHz, (e) 70.8 kHz, and (f) 95.9 kHz at 300 K. The damping peak fit curves are marked with different colours. For their parameters see Tab. 5.3. The total damping curve is drawn in black.

RELAX. PEAK	FREQUENCY @ 300 K (kHz)	T_{peak} (K)	Δ ($\times 10^{-8}$)	τ_0 (s) ($\times 10^{-14}$)	E_a (meV)
1. (olive)	38.4	10	4	80×10^6	1.5
	54.0	10	9.7	33×10^6	2
	58.9	13	10	50×10^6	2.1
	62.4	10	8.2	23×10^6	2.2
	70.8	12	14	16×10^6	2.8
	95.9	11	36	10×10^6	2.7
2. (blue)	38.4	36	4000	8	55
	54.0	37	2000	30	51
	58.9	36	2200	10	54
	62.4	37	800	10	55
	70.8	37	1200	30	51
	95.9	38	1590	30	50.5
3. (orange)	38.4	52	12	20	75
	54.0	55	10	40	75
	58.9	52	20	20	73
	62.4	53	2	20	75
	70.8	53	5	20	75
	95.9	55	11	20	75
4. (magenta)	38.4	68	2.2	15	101
	54.0	70	6	15	101
	62.4	75	2.5	15	101
	70.8	75	4	15	103
	95.9	73	5	15	101
5. (yellow)	38.4	82	4	40	115
	54.0	81	12	40	111
	62.4	82	4	40	111
	70.8	83	4.5	40	106
	95.9	82	11	30	109
6. (light green)	38.4	92	18	40	128
	54.0	93	20	40	128
	62.4	94	16	40	128
	70.8	95	18	60	124.5
	95.9	95	21	30	128
7. (violet)	38.4	109	5	2	180
	54.0	111	8	2	180
	62.4	112	2.2	2	180
	70.8	113	5	2	180
	95.9	116	10	2	182
8. (cyan)	38.4	119	17	4	190
	54.0	122	15	4	190
	62.4	123	3.2	4	190
	70.8	125	11	4	193
	95.9	125	26	4	190

Tab. 5.3: Parameters of the relaxation peaks in Figs. 5.10(a)-(f) gained by a fit procedure using Eq. (3.114). The background loss Q_{bg}^{-1} is max. 2×10^{-10} .

5.3 Crystalline calcium fluoride

Crystalline calcium fluoride is a material with key qualifications for optical technology - excellent transmittance, high laser damage threshold, low axial and radial stress birefringence, and high refractive-index homogeneity [141]. For its application in lithography technology single crystals grown from highly pure raw materials are available. Together with its good mechanical properties this qualifies calcium fluoride as a potential material for cryogenic IGWDs [151]. Q factors of up to 4.5×10^7 at room temperature are comparable with that of fused silica [152]. Indeed, systematic Q measurements for calcium fluoride existed only at room temperature so far [152]. Measurements in the low temperature range had been only performed at few cryogenic temperatures [153].

We performed systematic Q measurements in the wide temperature range from 300 K down to about 6 K [154]. The analysed sample was a single crystal, cylindrical in shape (76.2 mm in diameter, 75 mm thick) and oriented with the cylinder axis parallel to the [100] direction of the crystal. The material was produced by Schott Lithotec [141]. The suspension was realised with a tungsten wire-loop of 75 μm thickness. A thinner wire of 50 μm would have been sufficient regarding the tensile loading, but due to the low hardness of calcium fluoride the wire cut into the substrate. At room temperature we located 47 modes in the frequency range from 20 kHz to 100 kHz with amplitudes of 0.2 nm to 24 nm [99]. A selection of well measurable modes resulted in Q factors reaching over two decades from 2.8×10^5 to 1.3×10^7 . A further selection in respect of modes with a minor coupling of substrate and suspension (for details see section 4.1) ended in temperature dependent Q measurements on three modes whose results are shown in Fig. 5.11. Examining the mechanical losses of the selected modes there is only a minor variation with mode shape. Peaks with the same characteristic parameters appear in all damping curves except very narrow loss peaks above 100 K attributed to coupling of the substrate motion to the suspension [99]. Due to the temperature dependence of the resonant frequencies of substrate and suspension both may coincide at certain temperatures. In that case, oscillation energy is well transferred from the substrate to the suspension where it dissipates. Therefore, the length of the suspension wire has to be carefully chosen. The maximum Q value is reached at about 64 K with 1.43×10^8 for the mode with a frequency of 41302 Hz at 300 K. In a second run even 3×10^8 could be reached for the same mode [99]. Above 64 K the losses increase. Below 64 K several damping peaks are visible. The most pronounced peak occurs at about 30 K. In general, the mechanical losses increase below 30 K with decreasing temperature. To analyse the contribution of different relaxation processes to the total losses in calcium fluoride

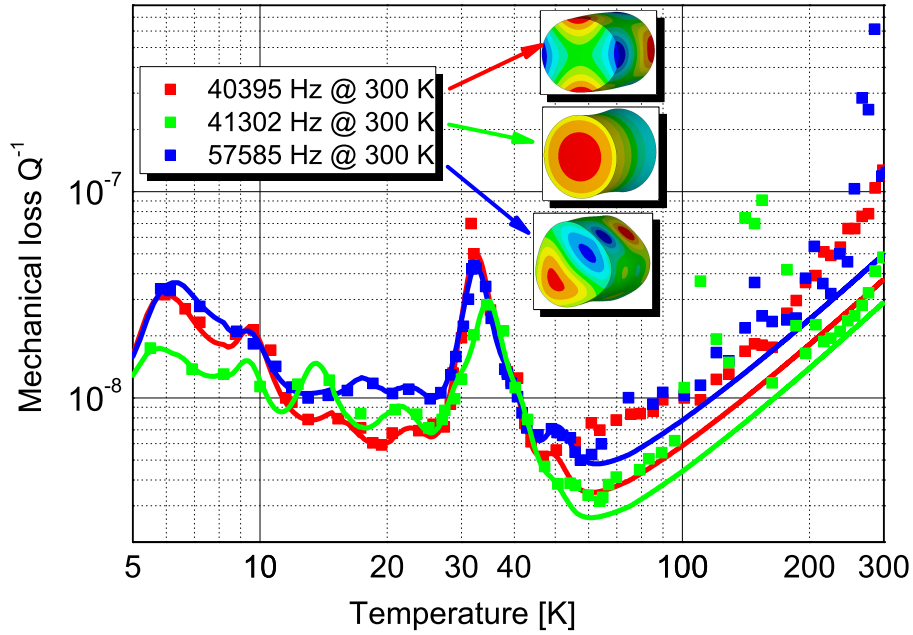


Fig. 5.11: Reciprocal of the measured Q factors versus temperature for a calcium fluoride sample (76.2 mm in diameter and 75 mm thick). Squares: measured data. Lines: fit of total damping curves, for details see Figs. 5.12(a)-(c) and Tab. 5.4. Insets show the calculated mode shapes of the measured modes. The essential material parameters have been taken from Schott Lithotec AG [141] (density) and Huffman et al. [155] (elastic constants).

the three damping curves have been separately fit using Eq. (3.114). The results are plotted in Figs. 5.12(a)-(c) with corresponding fit parameters in Tab. 5.4. In the low temperature range the mechanical losses are dominated by thermoelastic damping (black line in Fig. 5.12(a)-(c)). Although Eq. (3.68) is an approximation for the thermoelastic losses in anisotropic solids, giving correctly the order of magnitude and the trend, it reflects even the shape of the damping curve quite well. Due to the dominant contribution of the thermoelastic losses at low temperatures, the 'phonon-peak' (cyan line in Figs. 5.12(a)-(c)) is less visible. The damping at higher temperatures offers an orientation for fitting. Accordingly, the relaxation strength has been modelled to be proportional to T^2 . To keep the relaxation strength dimensionless, it is split into a dimensionless coupling strength Δ_0 and an also dimensionless function of reduced temperature ϑ and frequency f_r , $d(\vartheta, f_r)$

$$\Delta = \Delta_0 d(\vartheta, f_r). \quad (5.6)$$

Thus, in the case of calcium fluoride $d(\vartheta, f_r) = \vartheta^2$. An investigation of the losses below 5 K where the thermoelastic damping decreases would be helpful for a better determination of the shape of the maximum of the 'phonon-peak'. The relaxation time was assumed to follow an Arrhenius-like law (Eq. (3.84)) just as well as in the

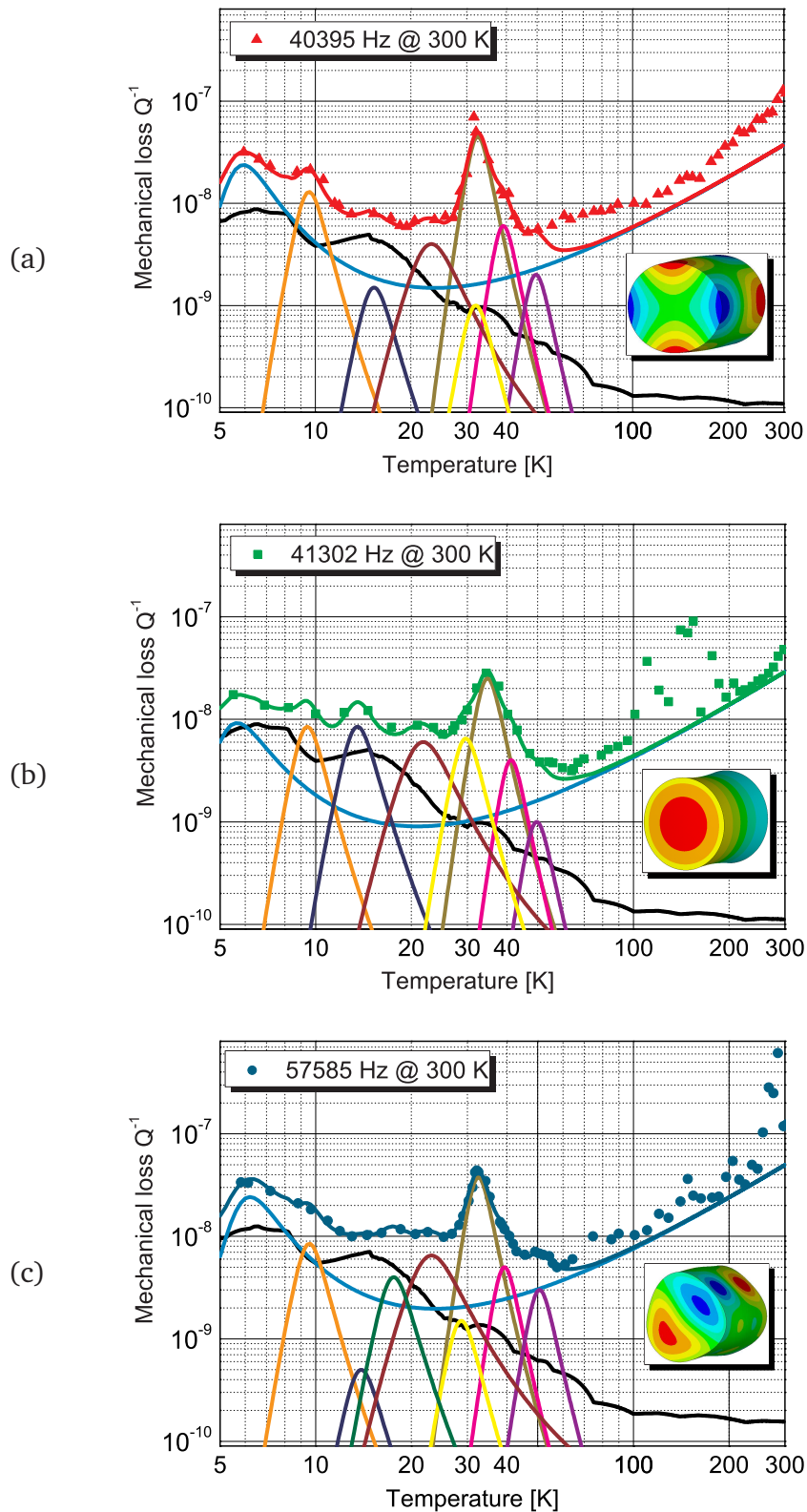


Fig. 5.12: Reciprocal of the measured Q factors vs. temperature for a CaF_2 sample (76.2 mm in diameter, 75 mm thick) measured at the resonant mode with the frequency of (a) 40395 Hz, (b) 41302 Hz, and (c) 57585 Hz at 300 K. Symbols: measured data. The fit curves are marked with different colours. For their parameters see Tab. 5.4. The total damping curves are drawn in the colours of the symbols.

RELAXATION PEAK	FREQUENCY @ 300 K (kHz)	T_{peak} (K)	Δ_0 ($\times 10^{-10}$)	τ_0 (s) ($\times 10^{-13}$)	E_a (meV)	$d(\vartheta, f_r)$
1. (cyan)	40.4	5	14	1×10^4	4.1	ϑ^2
	41.3	5	6	1.9×10^4	3.6	ϑ^2
	57.6	6	13	1×10^4	4.1	ϑ^2
2. (orange)	40.4	9	260	30	11.6	1
	41.3	9	170	30	11.4	1
	57.6	9	170	30	11.3	1
3. (dark blue)	40.4	15	30	1×10^2	17	1
	41.3	13	170	1×10^2	15	1
	57.6	14	10	1×10^2	15	1
4. (dark green)	57.6	17	80	1×10^2	19	1
5. (brown)	40.4	23	80	8×10^3	17	1
	41.3	21	120	10×10^3	15.5	1
	57.6	23	130	10×10^3	15.8	1
6. (yellow)	40.4	32	20	20	40	1
	41.3	29	130	20	37	1
	57.6	28	30	20	35	1
7. (dark yellow)	40.4	32	900	1	49	1
	41.3	34	500	3	49	1
	57.6	32	750	1	48	1
8. (magenta)	40.4	39	120	1	59	1
	41.3	41	80	1	62	1
	57.6	39	100	1	58	1
9. (violet)	40.4	50	40	3	70	1
	41.3	49	20	3	70	1
	57.6	50	60	3	70	1

Tab. 5.4: Parameters of the relaxation peaks in Figs. 5.12(a)-(c) gained by a fit procedure using Eq. (3.114).

case for crystalline quartz (see section 5.2). At 5 K the relaxation time is $\tau_1 = 1 \times 10^{-9} \text{ s} \cdot \exp(4.1 \text{ meV}/(k_B \cdot 5 \text{ K})) \approx 1.4 \times 10^{-5} \text{ s}$. Baumgartner et al. [156] observed a frequency independent value of about $5 \times 10^{-6} \text{ s}$ for the lifetime of acoustic phonons of frequency 0.5 THz to 1.5 THz at 2 K. This value is of the same order of magnitude as that determined by us.

For temperatures above 50 K no damping peaks with clear maxima are visible. The damping curve seems to be dominated alone by interactions of the acoustic wave with thermal phonons. Below 50 K several loss peaks in addition to the 'phonon-peak' occur. The corresponding activation energies reach from about 10 meV to 70 meV. Up to our knowledge they have not been observed before by mechanical spectroscopy. Only studies at higher temperatures have been published. The measurements of Franklin et al. [157] ceased at 77 K. In optical studies wave lengths of about 200 nm to 600 nm

have been used [158] which are associated with much higher activation energies. Nevertheless, Andeen et al. and Fontanella et al. [159–162] observed dielectric losses introduced by complexes in rare-earth doped calcium fluoride below 77 K. Similar loss sources might play a role in our measurements.

In summary, the highest Q factor measured in our experiments on calcium fluoride is 3×10^8 at 64 K. Below that temperature, the measured loss curves have been decomposed into several relaxation peaks having similar parameters for three selected modes. Also, an increasingly dominating contribution of thermoelastic losses could be identified below 64 K.

5.4 Crystalline silicon

Crystalline silicon is a potential material for cryogenic IGWDs because of its excellent thermo-mechanical properties [163]. Indeed, the lacking transmissivity at 1064 nm laser wave length requires an alternative interferometer topology using all-reflective optics. Such interferometer topologies, including nano-structured diffraction gratings offering ultra-low optical losses, are developed in other subprojects of the SFB/TR7 [164–167]. A clear advantage of the all-reflective topology would be the avoidance of thermal effects associated with laser power absorption in the mirrors and beam-splitter. This point becomes even more important in the future as higher laser powers are required to reduce photon shot noise. Thus, thermal noise as well as thermorefractive noise due to a non-homogeneous refraction index could be further reduced. Moreover, silicon is available as high-purity single crystals of sufficient size owing to its outstanding importance as the material for semiconductor industries per se.

The first silicon sample under investigation was of cylindrical shape, 76.2 mm in diameter and 12 mm thick [154]. The cylinder axis was oriented in direction of [100]. The reciprocals of the measured Q factors for three resonant modes are plotted in Fig. 5.13. Comparing our measured data on silicon with those on crystalline quartz and calcium fluoride the influence of the mode shape on the mechanical losses in the temperature range below about 150 K is striking. The 'profiles' of the damping curves, dominated by a varying number of distinct peaks, are quite different for the three modes. Above 150 K their behaviour indeed is similar, showing an increase of the losses with temperature. The damping curves have been separately analysed regarding contributions of different relaxation processes in Figs. 5.14(a)-(c). The corresponding relaxation parameters are given in Tab. 5.5. Like for calcium fluoride, the relaxation strength has been modelled as a product of a dimensionless coupling strength Δ_0 and a dimensionless function of reduced temperature and frequency,

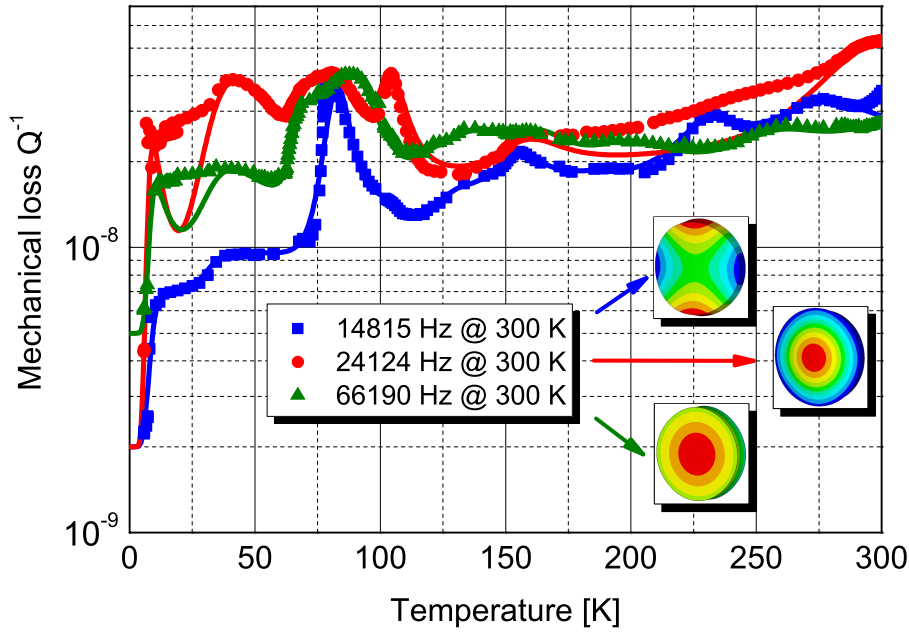


Fig. 5.13: Reciprocal of the measured Q factors versus temperature for a crystalline silicon (100) sample (76.2 mm in diameter and 12 mm thick). Symbols: measured data. Lines: fit of total damping curves, for details see Figs. 5.14(a)-(c) and Tab. 5.5. Insets show the calculated mode shapes of the measured modes. The essential material parameters have been taken from McSkimin et al. [168].

$d(\vartheta, f_r)$ (see Eq. (5.6)). The relaxation time was assumed to follow an Arrhenius-like law (Eq. (3.84)) for each relaxation process. Like for crystalline quartz and calcium fluoride, this assumption works well also for dissipation processes assigned to interactions of the acoustic waves with thermal phonons which dominate the mechanical losses over the whole temperature range (light green line in Figs. 5.14 (a)-(c)). The relaxation strength for this processes was proportional to T , respectively ϑ . In comparison, the results gained by applying the Landau-Rumer theory as well as the Akhieser theory (cf. section 3.3.2) are indicated by dashed black lines in Figs. 5.14 (a)-(c). Whereas the behaviour for very high and very low temperatures is well described by their theories, they fail in the important range of the peak maximum in between. Our model fits the measured data very well, although it is not clear why the description by double-well potentials works in the case of thermal phonons, too.

Several parameters of the remaining loss peaks have been related to formerly observed reorientation processes. Lam and Douglass [169, 170] reported an activation energy of $E_a=0.14$ eV and relaxation constants of $\tau_0=7.2 \times 10^{-12}$ s respectively $\tau_0=4.7 \times 10^{-12}$ s in loss measurements which could be assigned to vibrations of Si-O-Si complexes by infrared spectroscopy on oxygen-doped silicon. The dark green peaks in Figs. 5.14 (a) and (c) show similar parameters.

Lam and Douglass further related the parameters $E_a=0.20$ eV and $\tau_0=8.64 \times 10^{-13}$ s

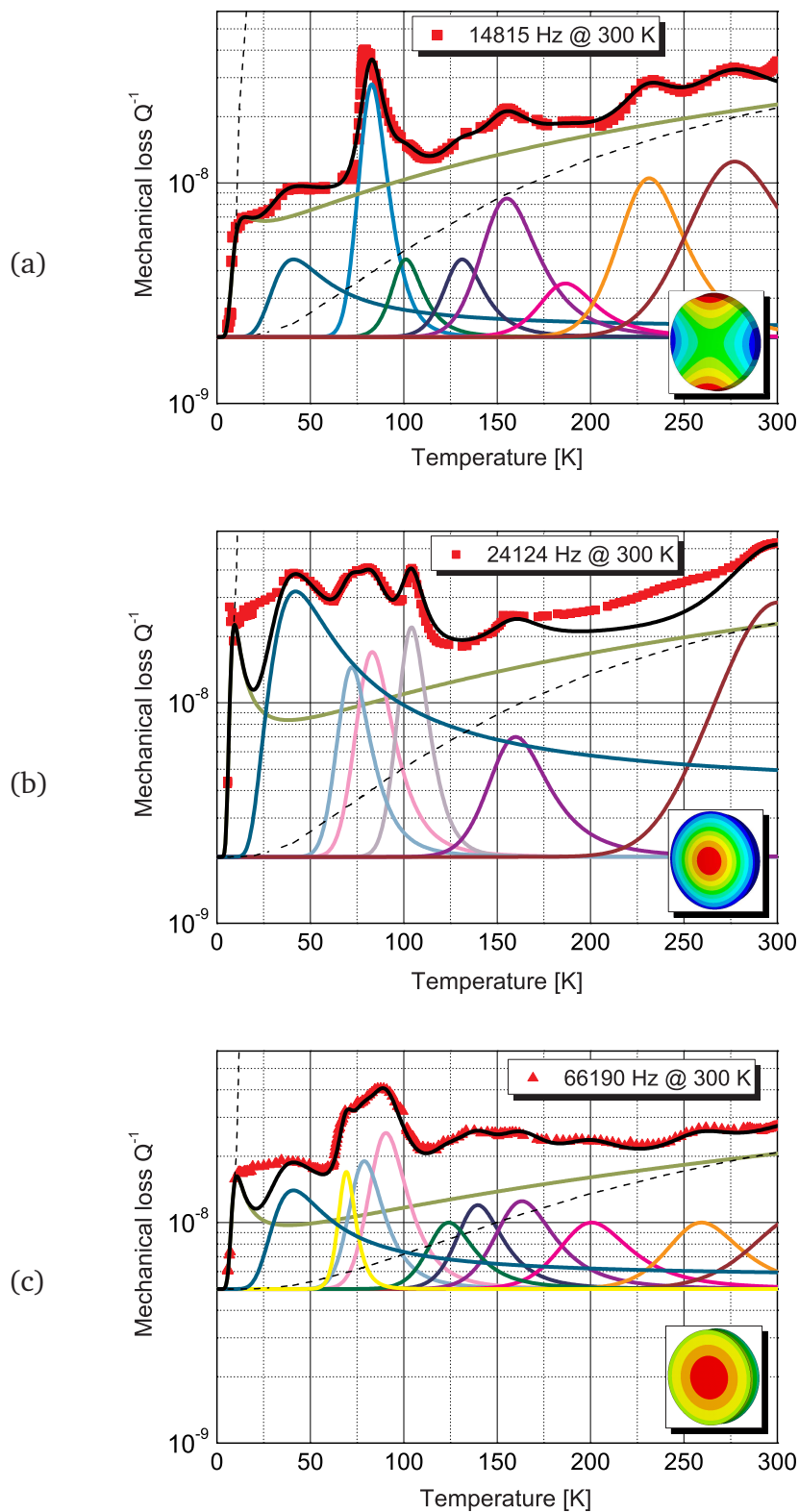


Fig. 5.14: Reciprocal of the measured Q factors versus temperature for a crystalline silicon (100) sample (76.2 mm in diameter and 12 mm thick) measured at the resonant mode (picture of mode shape included) with the frequency of (a) 14815 Hz, (b) 24124 Hz, and (c) 66190 Hz at 300 K. The damping peak fit curves are marked with different colours. For their parameters see Tab. 5.5. The total damping curve is drawn in black. - - - Fit according to Landau-Rumer as well as Akhieser theory (see text).

RELAXATION PEAK	FREQUENCY @ 300 K (kHz)	T_{peak} (K)	Δ_0 ($\times 10^{-10}$)	τ_0 (s) ($\times 10^{-15}$)	E_a (meV)	$d(\vartheta, f_r)$
1. (light green)	14.8	15	7.8	92×10^6	2.5	ϑ
	24.1	9	45	90×10^6	3.3	ϑ
	66.1	10	22	50×10^6	3.3	ϑ
2. (blue)	14.8	40	50	38×10^7	12	1
	24.1	41	600	20×10^7	12.7	1
	66.1	40	180	80×10^7	12	1
3. (yellow)	66.1	69	240	1	129	1
4. (light cyan)	24.1	72	250	9×10^3	84	1
	66.1	79	180	9×10^3	85	1
5. (light magenta)	24.1	83	300	5×10^3	101	1
	66.1	90	410	3×10^3	106	1
6. (cyan)	14.8	83	520	35	140	1
6. (dark green)	14.8	100	50	12×10^2	140	1
	66.1	123	100	60×10^2	138	1
8. (light violet)	24.1	104	400	1	203	1
9. (dark blue)	14.8	131	50	12×10^2	185	1
	66.1	139	140	6×10^2	183	1
10. (violet)	14.8	155	130	25×10^2	205	1
	24.1	160	100	30×10^2	200	1
	66.1	163	150	20×10^2	197	1
11. (magenta)	14.8	185	30	2×10^3	250	1
	66.1	200	100	3×10^3	235	1
12. (orange)	14.8	230	170	20	402	1
	66.1	259	100	100	380	1
13. (brown)	14.8	278	210	14×10^2	380	1
	24.1		530	28×10^2	380	1
	66.1		120	20×10^2	380	1

Tab. 5.5: Parameters of the relaxation peaks in Figs. 5.14(a)-(c) gained by a fit procedure using Eq. (3.114). The background loss Q_{bg}^{-1} is max. 2×10^{-9} .

to the vacancy-oxygen (VO) complex. At that time Watkins and Corbett [171] had already observed by electron spin resonance (ESR) that different kinds of redistribution can take place in an VO center. An electronic redistribution is related to the parameters mentioned above. A defect reorientation is characterised by $E_a=0.38$ eV and a relaxation time of $\tau_0=2 \times 10^{-13}$ s which had been also observed by Berry [172]. We assigned the violet and brown loss peaks observed in all damping curves of the three modes measured (Figs. 5.14 (a)-(c)) to the processes of an electronic redistribution and a defect reorientation of the VO complex, respectively.

Coutinho et al. [173] investigated a hydrogen atom jumping between two Si dangling bonds in vacancy-oxygen-hydrogen complexes (VOH and VOH₂ defects) with

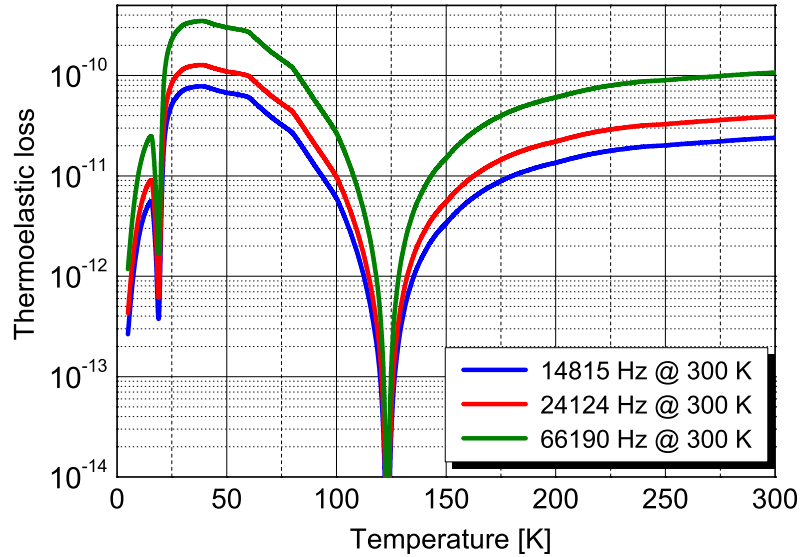


Fig. 5.15: Approximation of thermoelastic damping in crystalline silicon.

$E_a=0.18$ eV. The related relaxation constant reported by Johannesen et al. [174] is $\tau_0=1.1 \times 10^{-12}$ s. The dark blue relaxation peaks in Figs. 5.14 (a) and (c) are assigned to this defect. The silicon samples investigated in our experiments were grown by a Czochralski process. This method introduces a considerable amount of oxygen into the material. The oxygen content of the crystals used in our measurements is about $7 \times 10^{17} \text{cm}^{-3}$. As the VO as well as the VOH complex anneals out at 573 K, such a treatment might decrease the damping in the corresponding temperature regions. In general, samples grown by a process which reduces the introduction of oxygen into the crystalline material, like the float zone method, should be preferred in the future. According to the attenuation measurements of Pomerantz [175] the sample is presumably doped with phosphor (blue peak in Figs. 5.14 (a)-(c)). The associated damping peak occurs in our measurements at about 40 K. Thus, for the application in cryogenic IGWDs undoped silicon substrates should be preferred.

Regarding the relaxation strengths there is a strong dependence on mode shape for many relaxation processes observed for the three measured modes. A deeper study of these processes using in particular the method of symmetrized stresses and strains, and the selection rules described in sections 3.2.1 and 3.4.1.2 is recommended.

An approximation of the thermoelastic losses in silicon using Eq. (3.68) is shown in Fig. 5.15. The maximum loss occurring at about 30 K is estimated to 4×10^{-10} which is negligible as a minimum loss value of 8×10^{-9} has been measured at this temperature. To both higher and lower temperatures the thermoelastic noise decreases rapidly to zero at about 18 K and 123 K as the thermal expansion coefficient goes to zero at that temperatures (cf. Fig. A.14).

For a comparison of the mechanical losses of silicon substrates with different cuts, two

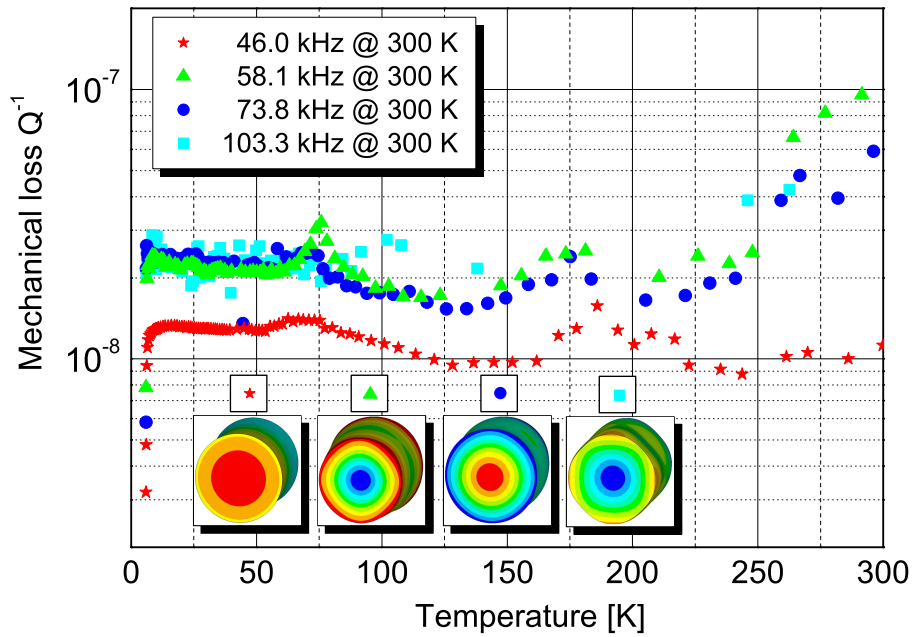


Fig. 5.16: Reciprocal of the measured Q factors versus temperature for a crystalline silicon (100) sample (76.2 mm in diameter and 75 mm thick) measured at 4 resonant modes (pictures of mode shapes included).

cylindrical samples, one with the cylinder axis oriented in the $[100]$ direction and the other oriented in the $[111]$ direction, have been measured. Both were 76.2 mm in diameter and 75 mm thick. The material has been produced by Siltronic AG [176] in a Czochralski process. Therefore, its oxygen content is quite high as written above. The concentration of carbon is specified by the producer to be $4 \times 10^{16} \text{ cm}^{-3}$. The samples have been p-doped with boron to a concentration of $4 \times 10^{14} \text{ cm}^{-3}$. The reciprocals of the measured Q factors are plotted in Fig. 5.16 and Fig. 5.17, respectively. The silicon (100) sample shows small damping peaks at about 75 K and around 180 K for the measured modes. A similar damping curve for a longitudinal mode at 29.2 kHz had been observed by Lam et al. [177]. For all modes, except the first one, the losses increase above 200 K with increasing temperature. Below about 10 K the losses decrease rapidly. This behaviour is ascribed to the 'phonon peak', presumably having its maximum at this temperature. Also effects due to the boron impurities could play a role in this temperature range, similar to that reported by Lam et al. [177]. Indeed, Lam et al. did not observe a decrease of the losses, probably due to the lower frequency used. Regarding the boron impurities a Jahn-Teller effect is considered [178–180]. For the fourfold degenerate ground state of the acceptors a mixing can occur by stresses and strains of symmetry designation E and T_2 (cf. section 3.2.1), changing the energy levels.

The silicon (111) sample shows a pronounced damping peak at about 170 K for the measured modes. For the first and third mode a rapid increase of the losses above

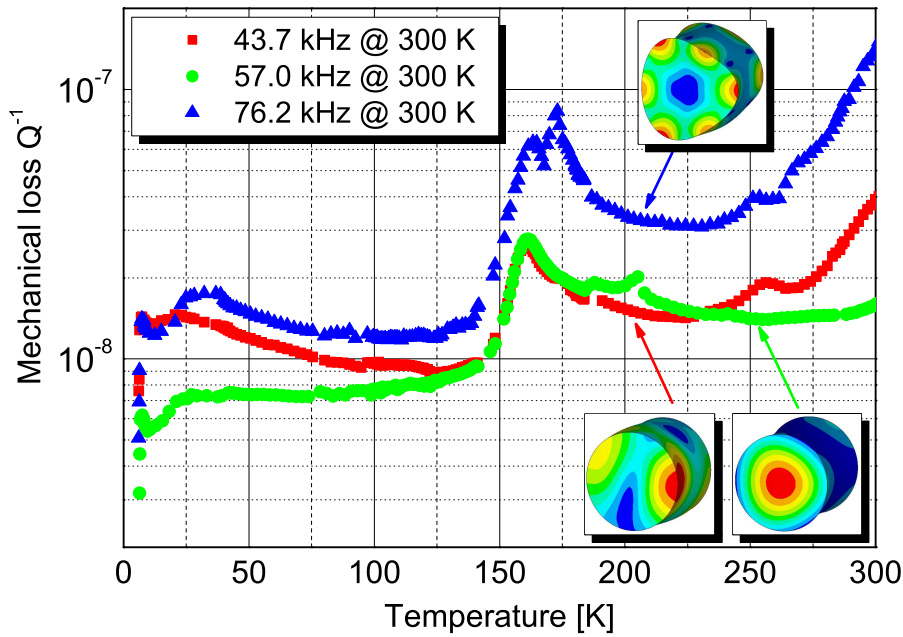


Fig. 5.17: Reciprocal of the measured Q factors versus temperature for a crystalline silicon (111) sample (76.2 mm in diameter and 75 mm thick) measured at 4 resonant modes (pictures of mode shapes included).

250 K is visible. At about 7 K a very sharp damping peak appears with a following step decrease of the losses to lower temperatures. Here also, a 'phonon peak' is assumed.

Comparing the mechanical losses below about 150 K for both cuts, the variation of the losses is stronger between the modes of one cut than between the cuts. The damping curves showing the lowest losses for both cuts have been extracted to Fig. 5.18. Silicon (111) shows lower losses below 150 K and higher losses above that temperature. Thus, this orientation is preferable for application in cryogenic IGWDs, at least according to the selected modes measured. The damping curves discussed above have not been decomposed into their different contributions yet, since the measurements have been done quite recently.

In summary, Q factor values of about 3×10^8 have been obtained at 6 K for boron-doped silicon in the (100) orientation as well as the (111) orientation. At 18 K - which is a reasonable temperature for cryogenic IGWDs - silicon (111) shows Q values of at least 1.5×10^8 . Measurements on a sample presumably doped with phosphorus yielded much lower Q factors. Relaxation processes involving oxygen complexes have been identified for this sample. Further systematic Q measurements are required to study the dependence of the losses on frequency and mode shape, respectively. In addition, other methods like ESR, mass spectrometry, and Brillouin spectroscopy are required to get broad information about the relaxation processes.

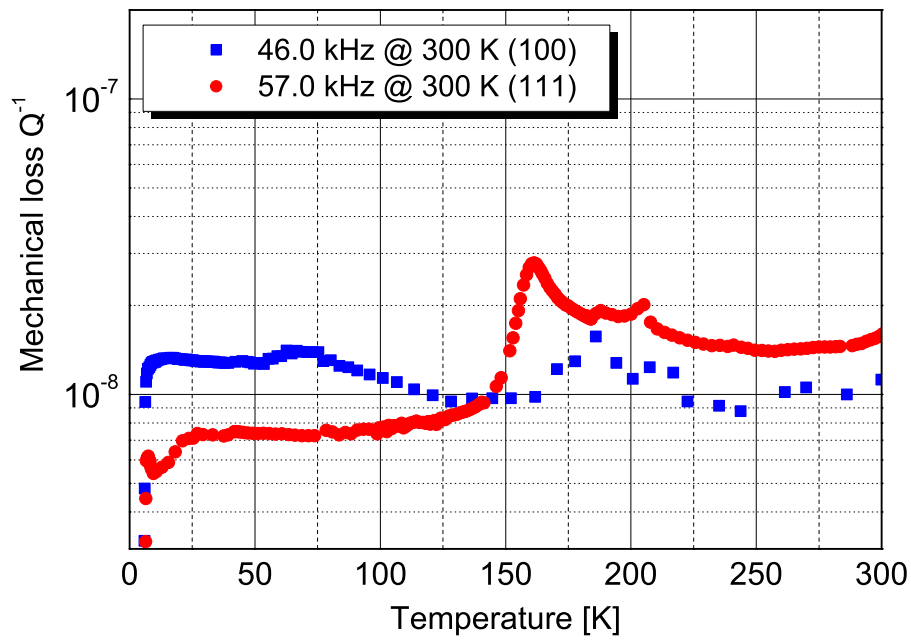


Fig. 5.18: Comparison of the reciprocal of the measured Q factors versus temperature for two crystalline silicon samples (76.2 mm in diameter and 75 mm thick) of orientation (100) and (111). The damping curves showing the lowest losses have been extracted from Fig. 5.16 and Fig. 5.17, respectively.

6 Impact of results on thermal noise reduction

After analysing the results of the temperature dependent Q factor measurements on fused silica, crystalline quartz, calcium fluoride and silicon the question arises, which materials are most suited regarding thermal noise reduction in cryogenic IGWDs. Note that the Q factors, respectively their reciprocals, do not give the mechanical losses in the detection frequency band as mechanical losses are in general frequency dependent. In transferring the mechanical losses from the kHz frequency range to several 100 Hz the measured damping curves have to be shifted to lower temperatures. Also the relaxation strengths of the particular processes may vary with frequency. Note that the damping peaks do not shift equally with frequency due to the different values of activation energy and relaxation constant entering the relation for the relaxation time which depends on temperature. If one damping curve shows a minimum at a certain temperature this does not necessarily hold for damping curves measured at other frequencies. To discover physical relations in the losses at the resonant frequencies by performing systematic Q measurements for an extrapolation to lower frequencies will be the task of our successors. At the current status an estimation of the Brownian part of the thermal noise by means of Levin's method (see section 2.4) can be given by using the highest Q factor value measured for a material at the corresponding temperature. The maximum deformation energy stored in the substrate during an oscillation cycle has been determined using the FEA software ANSYS [36]. Substrates without coating have been considered for the calculation. The original geometry of a GEO600 mirror (9 cm in diameter, 10 cm thick) has been used. If required, even complex geometrical features can be simulated like the stand-offs ('ears') for the suspension of a GEO600 mirror (Fig. 6.1). An estimation of the thermal noise limit to strain sensitivity of the GEO600 detector is given by

$$h_{GEO600}(f) = 2\sqrt{3S_x(f)}/1200, \quad (6.1)$$

assuming that all optical components, mirrors and beam splitter, have the same power spectral density of the thermal displacement, x , at frequency f , $S_x(f)$ [182]. A comparison of the Brownian part of thermal noise at room temperature and at cryogenic conditions is shown in Fig. 6.2. At room temperature the Brownian thermal noise is of the same order of magnitude for all considered materials with an h_{GEO600} value of

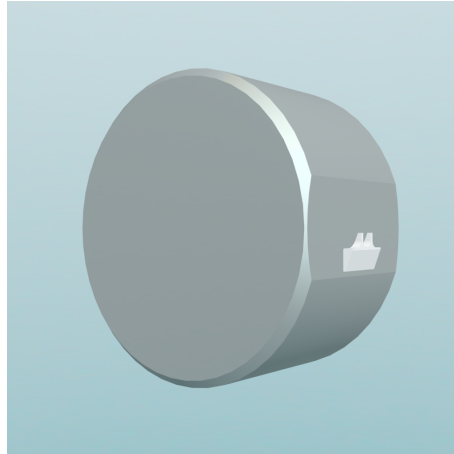


Fig. 6.1: CAD model of a GEO600 mirror, designed with Pro/ENGINEER [181].

about 5×10^{-23} at 100 Hz since the Q factor values are also similar. By contrast, at low temperatures the results of the thermal noise calculations reveal wide differences between the materials investigated. Test masses made of fused silica would lose a factor of about 50 in sensitivity by operating them at about 20 K. Its crystalline counterpart would bring a benefit of more than one order of magnitude by cooling to 5 K, at least for a purity grade similar to the material investigated. A reduction of loss peaks by using samples of higher purity or sweeping or irradiating them could possibly attain higher Q factor values than 2×10^7 even at about 70 K. Indeed, Q factors of more than 1×10^8 like in calcium fluoride and silicon will be hardly to achieve.

Calcium fluoride shows a maximum Q factor of 3×10^8 at 64 K for the measured modes resulting in a h_{GEO600} of 1.4×10^{-24} at 100 Hz. Far lower operating temperatures seem to be unrealistic for calcium fluoride since its thermoelastic losses rise steeply with decreasing temperature.

Silicon shows similar low losses at 18 K which is a realistic operating temperature for cryogenic IGWDs. Moreover, the thermoelastic losses in silicon decrease to zero at this temperature thanks to the vanishing thermal expansion coefficient. Using silicon as a substrate material for a cryogenic version of GEO600 the substrate thermal noise limit to strain sensitivity is estimated to 4×10^{-25} corresponding to an increase in sensitivity of more than two orders of magnitude compared to the current version operating at room temperature.

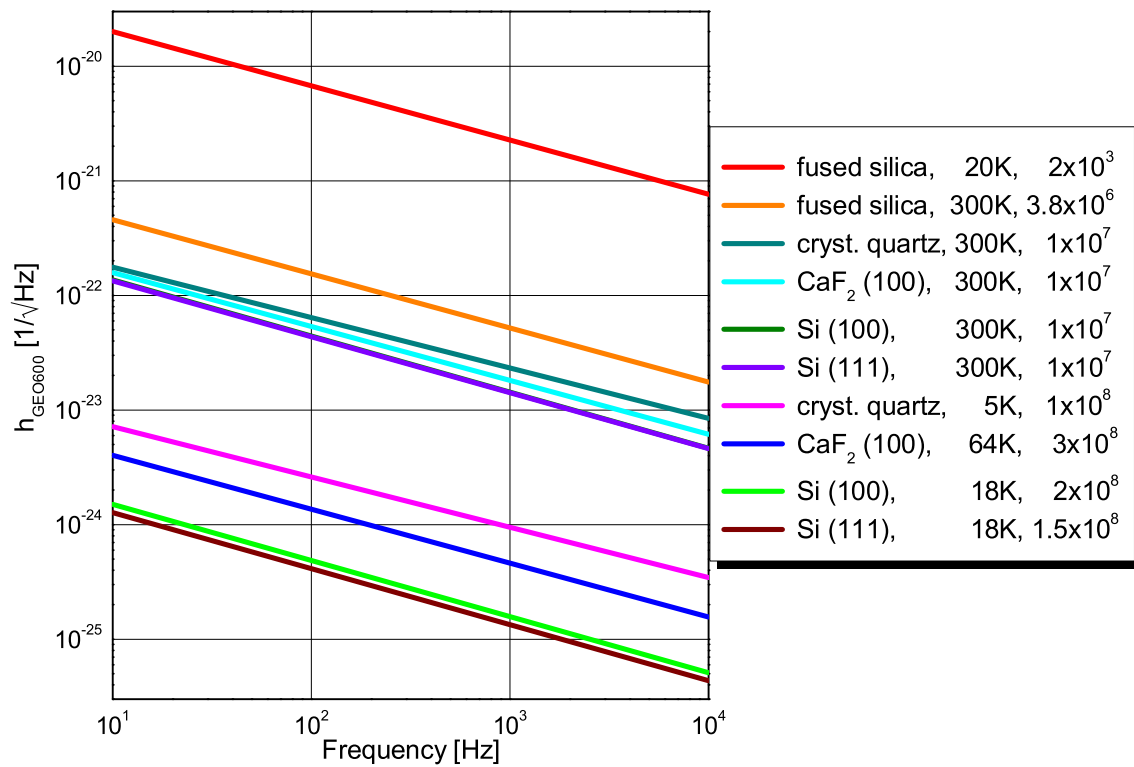


Fig. 6.2: Comparison of the calculation of the Brownian part of the thermal noise in the IGWD GEO600 for several substrate materials. Presented is the estimated noise in room temperature operation and its reduction in a cryogenic IGWD assuming the highest Q factors measured in our experiments and the corresponding temperatures for the particular material.

7 Conclusions and further prospects

The aim of this work consisted in the study of the mechanical losses of potential substrate materials for future cryogenic interferometric gravitational wave detectors to reduce the thermal noise of their optical components.

Interferometric gravitational wave detectors (IGWDs) are among the instruments with the highest sensitivity ever built. Their detection principle is based upon an effective change of the interferometer arm lengths by an arriving gravitational wave. The length change respectively the relative change, indeed, is tiny. 10^{-20} is the relative change caused by a strong gravitational wave, corresponding to its amplitude [10]. The currently working IGWDs reach this sensitivity. Nevertheless, the probability of an event producing a gravitational wave of this amplitude is low. To increase the detection probability and also to gain a deeper look in the universe by establishing a gravitational wave astronomy the enhancement of the sensitivity is inevitable. A main noise source to be reduced is the thermal noise of the optical components like mirrors and beam splitter.

A very promising approach for a reduction of thermal noise is to deprive thermal energy by decreasing the operating temperature of the IGWDs from room temperature to cryogenic temperatures. Since thermal noise mainly depends on two physical values - temperature and mechanical loss at that temperature and given frequency - materials showing low mechanical losses at low temperatures are then required for these future detectors. Fused silica, which is the common material of current IGWDs operated at room temperature, and crystalline quartz, crystalline calcium fluoride, and crystalline silicon, which are potential low-loss materials, have been studied in this work. Therefore, a novel kind of mechanical spectroscopy, cryogenic resonant acoustic (CRA) spectroscopy of bulk materials, has been evolved, based on established methods. CRA spectroscopy is a highly sensitive method thanks to the facility for performing mechanical Q measurements without any contact to the sample. Note that the mechanical Q factors are the reciprocals of the mechanical losses at the resonances. Q factor values of up to 3×10^{10} are in principle measurable in the current configuration. Furthermore, a high temperature stability in the temperature range from 5 K to 325 K as well as a quasi unperturbed measurement is guaranteed by performing the measurements in a custom made cryostat located in a special laboratory. Thanks to this excellent features, CRA spectroscopy has an outstanding role in the international research field. Only few groups are or have been able to perform measurements of similar sensitivity over such a large temperature range and study the

mechanical losses systematically.

A precondition for the Q factor measurements was the determination of the resonant frequencies and mode shapes of the samples. This was realised by the application of the finite element analysis (FEA) based software ANSYS. Thus, characteristic mode shapes could be selected and the experimental search for the resonances could be extremely reduced.

A successful test of CRA spectroscopy has been accomplished by measuring samples of the fairly well-known material crystalline quartz. The gained relaxation parameters of some known loss processes agree well with that stated in literature. Moreover, the capability of CRA spectroscopy of observing intrinsic loss processes respectively relaxation processes has been shown by a variation of sample geometry.

A description of mechanical losses in solids has been acquired and applied to the modelling of the quality factors measured on the potential substrate materials. An effective and controlled reduction of the mechanical losses requires the understanding of the loss mechanisms. A combination of those models and the relaxation parameters gained by performing systematic Q measurements should permit to draw conclusions regarding the mechanical losses in the detection frequency band of the IGWDs which lies beneath the resonances of the measured samples located in the kHz range.

Fused silica is the substrate material currently used in IGWDs. It possesses good optical properties at the currently used laser wavelength of 1064 nm as well as high Q factor values at room temperature. However, our measurements have shown that the losses in fused silica increase with decreasing temperature, showing a high and broad relaxation peak with a maximum loss of about 1×10^{-3} at 20 K for a frequency of 17 kHz. Thus, fused silica is not suited as a substrate material for future cryogenic IGWDs. The origin of the broad relaxation peak lies in the amorphous character of fused silica. The loss peak could be reproduced by assuming relaxation processes in asymmetric double-well potentials with varying wall heights. Even if fused silica has dropped out of the potential material pool, this description may be suitable for modelling the mechanical losses in the dielectric mirror coatings which are of amorphous structure. During the last years the international interest in mechanical loss studies for IGWDs mainly focused on the coating research [183–186]. We also extended our research field to this topic [187, 188].

The result from the measurements on fused silica is that a potential material for cryogenic IGWDs has to be searched within crystalline materials which show far less structural variability. Crystalline quartz, the crystalline counterpart of fused silica, possesses nearly as good optical properties as the amorphous material. Also the mechanical losses at room temperature are similar. However, at low temperatures only small and narrow damping peaks have been measured. Over the whole temperature

range the damping curves were dominated by loss processes caused by interactions of the excited acoustic wave with thermal phonons of the crystal. This behaviour was also observable in the Q measurements on calcium fluoride and silicon. Since these phonon-phonon interactions also occur in an 'ideal' defect-free material and such cannot be influenced by the purity grade of the material, they are of special importance. Modelling the thermal phonon-induced losses turned out to be difficult on the one hand. In spite of extensive research on this topic in the past, the qualitative loss processes are understood, but quantitative description is lacking. Also, previous experiments had been carried out at far higher frequencies, starting at the MHz region and the modelling had been adapted to this regime. On the other hand, we were quite successful in applying a similar model to the thermal phonon-induced losses as for the defect related. Dissipation, meaning the withdrawal of oscillation energy, related to defects occurs at stress-induced redistribution of particles in double-well potentials. Many of the peaks occurring in the damping curves for crystalline quartz could be imputed to relaxation processes involving alkali ions. New damping peaks, whose origin is yet not clear, have been also observed. To reveal their nature other methods like infrared spectroscopy and mass spectrometry should be called. Another promising approach is considering group theory for the support of the description of point defect induced losses since defect symmetry and the occurrence of losses are related. By means of selection rules it should be possible to draw conclusions from the variation of relaxation strength with mode shape regarding the defect symmetry.

Q factor values of up to 1×10^8 at 5 K have been obtained in crystalline quartz. Moreover, it may be possible to further reduce the losses in the minimum at about 70 K by using a material of higher grade, by irradiating it, or by replacing the alkali-ions with other charge carriers by sweeping the crystal. In comparison to the higher Q factors measured on calcium fluoride and silicon at realisable temperatures for cryogenic IG-WDs, however, crystalline quartz loses for now.

Crystalline calcium fluoride has excellent optical properties, often used in lithography technology. For a sample in (100) orientation a maximum Q factor of 3×10^8 has been observed at 64 K. Below this temperature several relaxation processes have been located coincident for three selected modes. The relaxation parameters, in particular the low activation energies, point to electronic reorientation processes. Further on, below 64 K the mechanical losses are increasingly dominated by thermoelastic losses with decreasing temperature. This fact reduces the importance of calcium fluoride as a future substrate material.

On the contrary, crystalline silicon possesses two zero crossings of the thermal expansion coefficient at 18 K and 123 K causing vanishing thermoelastic losses at these temperatures. Furthermore, silicon offers good thermal properties like high thermal

conductivity. 18 K is a realistic temperature for operating a cryogenic IGWD, accessible by pulse tube cryocoolers [189]. At this temperature Q factor values of about 1.5×10^8 have been obtained for boron-doped silicon in the (111) orientation. Silicon (100) also offers high Q factor values in this temperature range. Measurements on another sample yielded much lower Q factors. The interpretation of damping curves recorded for three modes suggest doping with phosphorus. Furthermore, relaxation processes involving oxygen complexes have been identified. The high oxygen concentration is caused by the crystal growth achieved by the Czochralski method. To reduce these losses a method introducing less oxygen into the crystal, like the float zone method, should be preferred. In general, silicon is suitable to study mechanical loss processes dependent on doping and on the crystal orientation.

Thanks due its outstanding importance in semiconductor industries silicon combines properties appropriate for cryogenic IGWDs like its availability as high-purity single crystals of sufficient size as well as economic criteria as affordability of the material. Since silicon is not transparent at 1064 nm the current transmissive interferometer topology would not be applicable. This would be no problem as either a laser wavelength of 1550 nm could be used or the interferometer could be designed to have all-reflective optics [164–167]. We did not find any negative influence of a reflection grating on the mechanical Q factor [187]. An additional benefit of a non-transmissive interferometer topology would be less energy transferred from the laser into the material, further reducing thermal noise. Alternative materials to silicon are sapphire, silicon carbide, or diamond. The last two materials are not available as single crystals of sufficient size. Sapphire, however, has higher thermoelastic losses over the whole temperature spectrum [190]. Based on Levin's method, the change in the Brownian part of the substrate thermal noise has been calculated assuming the highest measured Q factor values. For silicon (111) as the favourite a gain in detection sensitivity of about two orders of magnitude might be achieved by operating the IGWDs at 18 K.

Bibliography

- [1] A. Einstein, *Ann. Phys.* **49**, 769–822 (1916).
- [2] R. A. Hulse and J. H. Taylor, *Astrophys. J.* **195**, L51–L53 (1975).
- [3] J. H. Taylor, L. A. Fowler and P. M. McCulloch, *Nature* **277**, 437–440 (1979).
- [4] J. H. Taylor and J. M. Weisberg, *Astrophys. J.* **253**, 908–920 (1982).
- [5] F. J. Raab (representing the Ligo Scientific Collaboration) and other laser interferometer groups, *J. Phys.: Conf. Ser.* **39**, 25–31 (2006).
- [6] S. Rowan and J. Hough, *Living Rev. Relativity* **3** (2000), url: <http://www.livingreviews.org/lrr-2000-3>.
- [7] S. Miyoki, T. Uchiyama, K. Yamamoto *et al.*, *Class. Quantum Grav.* **23**, S231–S237 (2006).
- [8] R. Nawrodt, *Kryogene Gütemessung an optischen Substratmaterialien für zukünftige Gravitationswellendetektoren*, Ph.D. thesis, Friedrich-Schiller-Universität Jena (2007).
- [9] N. Arnaud, M. Barsuglia, M. A. Bizouard *et al.*, *Astropart. Phys.* **21**, 201–221 (2004).
- [10] B. F. Schutz, *Class. Quantum Grav.* **6**, 1761–1780 (1989).
- [11] B. F. Schutz, *Class. Quantum Grav.* **13**, A219–A238 (1996).
- [12] J. Weber, *Phys. Rev. Lett.* **18**, 498–501 (1967).
- [13] J. Weber, *Phys. Rev. Lett.* **20**, 1307–1308 (1968).
- [14] J. Weber, *Phys. Rev. Lett.* **22**, 1320–1324 (1969).
- [15] V. Fafone, *Class. Quantum Grav.* **21**, S377–S383 (2004).
- [16] D. G. Blair, *Class. Quantum Grav.* **18**, 4087–4100 (2001).
- [17] I. S. Heng, E. Daw, J. Giaime *et al.*, *Class. Quantum Grav.* **19**, 1889–1895 (2002).
- [18] L. Conti, *Nucl. Instrum. Methods Phys. Res. Sect. A-Accel. Spectrom. Dect. Assoc. Equip.* **518**, 236–239 (2004).
- [19] P. Astone, D. Babusci, M. Bassan *et al.*, *Phys. Rev. Lett.* **91**, 111101–1–111101–4 (2003).
- [20] A. de Waard, L. Gottardi, J. van Houwelingen *et al.*, *Class. Quantum Grav.* **20**, S143–S151 (2003).
- [21] P. Astone, M. Bassan, P. Bonifazi *et al.*, *Astropart. Phys.* **7**, 231–243 (1997).

- [22] D. Coward, D. Blair, R. Clay *et al.*, *Class. Quantum Grav.* **19**, 1871–1875 (2002).
- [23] M. Bonaldi, M. Cerdonio, L. Conti *et al.*, *Nucl. Phys. B - Proceedings Supplements* **138**, 443–445 (2005).
- [24] H. Lück, M. Hewitson, P. Ajith *et al.*, *Class. Quantum Grav.* **23**, S71–S78 (2006).
- [25] S. J. Waldman, *Class. Quantum Grav.* **23**, S653–S660 (2006).
- [26] M. Ando, *Class. Quantum Grav.* **22**, S881–S889 (2005).
- [27] F. Acernese, P. Amico, M. Alshourbagy *et al.*, *Class. Quantum Grav.* **23**, S635–S642 (2006).
- [28] GEO600 - The German-British Gravitational Wave Detector, url: <http://geo600.aei.mpg.de/>.
- [29] G. Heinzl, C. Braxmaier, K. Danzmann *et al.*, *Class. Quantum Grav.* **23**, S119–S124 (2006).
- [30] P. R. Saulson, *Fundamentals of Interferometric Gravitational Wave Detectors* (World Scientific, Singapore, 1994).
- [31] H. B. Callen and T. A. Welton, *Phys. Rev.* **83**, 34–40 (1951).
- [32] H. B. Callen and R. F. Greene, *Phys. Rev.* **86**, 702–710 (1952).
- [33] A. Gillespie and F. Raab, *Phys. Rev. D* **52**, 577–585 (1995).
- [34] A. Gillespie, *Thermal noise in the initial LIGO interferometers*, Ph.D. thesis, California Institute of Technology (1995).
- [35] Y. Levin, *Phys. Rev. D* **57**, 659–663 (1998).
- [36] ANSYS, url: <http://www.ansys.com>.
- [37] V. B. Braginsky, M. L. Gorodetsky and S. P. Vyatchanin, *Phys. Lett. A* **264**, 1–10 (1999).
- [38] Y. T. Liu and K. S. Thorne, *Phys. Rev. D* **6212**, 122002–1–122002–10 (2000).
- [39] D. Heinert, *Mechanische Verluste in Festkörpern*, Master’s thesis, Friedrich-Schiller-Universität Jena (2007).
- [40] R. O’Shaughnessy, *Class. Quantum Grav.* **23**, 7627–7630 (2006).
- [41] V. Galdi, G. Castaldi, V. Pierro *et al.*, *Phys. Rev. D* **73**, 127101–1–127101–4 (2006).
- [42] J. Y. Vinet, *Class. Quantum Grav.* **22**, 1395–1404 (2005).
- [43] E. D’Ambrosio, R. O’Shaughnessy, K. Thorne *et al.*, *Class. Quantum Grav.* **21**, S867–S873 (2004).

- [44] A. S. Nowick and B. S. Berry, *Anelastic Relaxation in Crystalline Solids* (New York & London: Academic Press, 1972).
- [45] P. Debye, *Polar Molecules* (Chemical Catalog Company, 1929).
- [46] W. Voigt, *Lehrbuch der Kristallphysik* (Leipzig: Teubner, 1928).
- [47] J. F. Nye, *Physical Properties of Crystals. Their Representation by Tensors and Matrices* (Oxford University Press, 2007).
- [48] A. S. Nowick and W. R. Heller, *Advan. Phys.* **14**, 101–166 (1965).
- [49] R. S. Mulliken, *J. Chem. Phys.* **23**, 1997–2011 (1955).
- [50] V. B. Braginsky and V. P. Mitrofanov, *Systems with Small Dissipation* (Chicago: The University of Chicago Press, 1985), p. 11.
- [51] J. Ferreirinho, *The detection of gravitational waves*, Chapter: 6 Internal friction in high Q materials, 116–168 (Cambridge University Press, 1993).
- [52] D. G. Blair and J. Ferreirinho, *Phys. Rev. Lett.* **49**, 375–378 (1982).
- [53] A. N. Norris and D. M. Photiadis, *Q. J. Mech. Appl. Math.* **58**, 143–163 (2005).
- [54] A. N. Norris, *J. Therm. Stresses* **29**, 169–195 (2006).
- [55] B. H. Houston, D. M. Photiadis, M. H. Marcus *et al.*, *Appl. Phys. Lett.* **80**, 1300–1302 (2002).
- [56] X. Liu, J. F. Vignola, H. J. Simpson *et al.*, *J. Appl. Phys.* **97**, 023524–1–023524–6 (2005).
- [57] B. H. Houston, D. M. Photiadis, J. F. Vignola *et al.*, *Mater. Sci. Eng. A-Struct. Mater. Prop. Microstruct. Process.* **370**, 407–411 (2004).
- [58] A. Akhieser, *J. Phys. (Moscow)* **1**, 277–287 (1939).
- [59] G. A. Alers, *Physical Acoustics: Principles and Methods*, Vol. III B, Chapter: Use of Sound Velocity Measurements in Determining the Debye Temperature of Solids (New York: Academic Press, 1965).
- [60] H. E. Bömmel and K. Dransfeld, *Phys. Rev.* **117**, 1245–1252 (1960).
- [61] T. O. Woodruff and H. Ehrenreich, *Phys. Rev.* **123**, 1553–1559 (1961).
- [62] L. Landau and G. Rumer, *Physik. Z. Sowjetunion* **11**, 18–25 (1937).
- [63] W. P. Mason and T. B. Bateman, *J. Acoust. Soc. Am.* **36**, 644 (1964).
- [64] R. Orbach and L. A. Vredevoe, *Physics* **1**, 91–94 (1964).
- [65] P. G. Klemens, *Physical Acoustics: Principles and Methods*, Vol. III B, Chapter: Effect of Thermal and Phonon Processes on Ultrasonic Attenuation, 201–234 (New York: Academic Press, 1965).

- [66] W. P. Mason, *Physical Acoustics: Principles and Methods*, Vol. III B, Chapter: Effect of Impurities and Phonon Processes on the Ultrasonic Attenuation of Germanium, Crystal Quartz, and Silicon, 235–286 (New York: Academic Press, 1965).
- [67] H. J. Maris, *Phil. Mag.* **12**, 89–106 (1965).
- [68] P. B. Miller, *Phys. Rev.* **1**, A1937–A1938 (1965).
- [69] P. C. Kwok and P. C. Martin, *Solid State Commun.* **3**, 181–184 (1965).
- [70] R. A. Guyer, *Phys. Rev.* **148**, 789–797 (1966).
- [71] J. Kalejs, H. Maris and R. Truell, *Phys. Lett.* **23**, 299–300 (1966).
- [72] N. S. Shiren, *Phys. Lett.* **20**, 10–11 (1966).
- [73] P. G. Klemens, *J. Appl. Phys.* **38**, 4573–4576 (1967).
- [74] R. Klein, *Physik Der Kondensierten Materie* **6**, 38–50 (1967).
- [75] H. H. Barrett and M. G. Holland, *Phys. Rev. B* **1**, 2538–2544 (1970).
- [76] D. A. Garanin and V. S. Lutovinov, *Ann. Phys.* **218**, 293–324 (1992).
- [77] R. Nava, R. Azrt, I. Ciccarello *et al.*, *Phys. Rev. A* **134**, A581–A589 (1964).
- [78] M. Pomerantz, *Phys. Rev.* **139**, A501–A506 (1965).
- [79] M. F. Lewis and E. Patterson, *Phys. Rev.* **159**, 703–711 (1967).
- [80] R. C. Purdom and E. W. Prohofsky, *Phys. Rev. B* **2**, 551–553 (1970).
- [81] P. J. King, *J. Phys. C: Solid State Phys.* **3**, 500–509 (1970).
- [82] W. Liekens, L. Michiels and A. de Bock, *J. Phys. C: Solid State Phys.* **4**, L308–L310 (1971).
- [83] I. S. Ciccarello and K. Dransfeld, *Phys. Rev.* **134**, A1517–A1520 (1964).
- [84] J. de Klerk and P. G. Klemens, *Phys. Rev.* **147**, 585–588 (1966).
- [85] M. J. Keck and R. J. Sladek, *Phys. Rev. B* **2**, 3135–3139 (1970).
- [86] Y. V. Ilisavskii and V. M. Sternin, *Fiz. Tverd. Tela* **27**, 385–391 (1985).
- [87] S. D. Lambade, G. G. Sahasrabudhe and S. Rajagopalan, *Phys. Rev. B* **51**, 15861–15866 (1995).
- [88] G. G. Sahasrabudhe and S. D. Lambade, *J. Phys. Chem. Solids* **60**, 773–785 (1999).
- [89] R. B. Kaner, J. J. Gilman and S. H. Tolbert, *Science* **308**, 1268–1269 (2005).
- [90] R. de Batist, *Internal Friction of Structural Defects in Crystalline Solids*, Vol. 5 of *Defects in crystalline solids* (Amsterdam: North-Holland Pub. Co, 1972).

- [91] A. Würger, *From Coherent Tunneling to Relaxation: Dissipative Quantum Dynamics of Interacting Defects* (Springer, Berlin, 1997).
- [92] A. S. Nowick, *Advan. Phys.* **16**, 1–47 (1967).
- [93] A. S. Nowick and W. R. Heller, *Advan. Phys.* **12**, 251–298 (1963).
- [94] International Union of Crystallography, *International Tables for X-Ray Crystallography*, Vol. I (Birmingham: Kynoch Press, 1952).
- [95] Kröner, *Kontinuumstheorie der Versetzungen und Eigenspannungen* (Berlin: Springer, 1958).
- [96] E. Kröner, *Kontinuumstheorie der Versetzungen und Eigenspannungen*, Vol. 5 of *Ergebnisse der angewandten Mathematik* (Berlin: Springer, 1958).
- [97] D. Wollenweber, S. Strassburg and G. Wunsch, *Fresenius J. Anal. Chem.* **364**, 433–437 (1999).
- [98] A. S. Nowick and M. W. Stanley, *Physics of the Solid State*, Chapter: Analysis of Dielectric and Anelastic Relaxation Due to Point Defects in α -Quartz, 183–206 (London: Academic Press, 1969).
- [99] R. Nawrodt, A. Zimmer, T. Koettig *et al.*, *Eur. Phys. J. Appl. Phys.* **38**, 53–59 (2007).
- [100] M. Hudl, *Untersuchung von mechanischen Dämpfungsvorgängen in dielektrischen Schichten*, Master's thesis, Friedrich-Schiller-Universität Jena (2007).
- [101] L. J. Dijkstra, *Philips Res. Rep.* **2**, 357–381 (1947).
- [102] R. Nawrodt, A. Zimmer, S. Nietzsche *et al.*, *Cryogenics* **46**, 718–723 (2006).
- [103] C. Schwarz, *Kryogene Gütemessung an optischen Substraten für Gravitationswellendetektoren*, Master's thesis, Friedrich-Schiller-Universität Jena (2007).
- [104] Hellma Optik GmbH Jena, Germany, url: www.hellmaoptik.com.
- [105] A. Gillespie and F. Raab, *Phys. Lett. A* **178**, 357–363 (1993).
- [106] K. Numata, G. B. Bianc, N. Ohishi *et al.*, *Phys. Lett. A* **276**, 37–46 (2000).
- [107] INFN Sez. Firenze, GeNS: a Gentle Nodal Suspension, url: <http://moriond.in2p3.fr/J07/trans/saturday/lorenzini.pdf>.
- [108] G. Cagnoli, J. Hough, D. DeBra *et al.*, *Phys. Lett. A* **272**, 39–45 (2000).
- [109] K.-J. Bathe, *Finite Element Procedures* (Bathe, K.-J., 2007).
- [110] K.-J. Bathe, *Finite-Elemente-Methoden* (Berlin: Springer, 2002).
- [111] SIOS Meßtechnik GmbH, Ilmenau, Germany, url: <http://www.sios.de/>.
- [112] D. Heinert, A. Zimmer, R. Nawrodt *et al.*, *arXiv:0709.2093v1 [cond-mat.other]*, accepted for publication in *J. Phys.: Conf. Ser.* (2007).

- [113] Cryovac mbH & Co KG, url: <http://www.cryovac.de/>.
- [114] S. Hild, H. Lück, W. Winkler *et al.*, *Appl. Optics* **45**, 7269–7272 (2006).
- [115] Y. S. Touloukian, R. K. Kirby, R. E. Taylor *et al.* (eds.), *Thermophysical properties of matter (Thermal Expansion, Nonmetallic Solids)*, Vol. 13 (New York, NY: IFI/Plenum, 1977).
- [116] A. Ageev, B. C. Palmer, A. De Felice *et al.*, *Class. Quantum Grav.* **21**, 3887–3892 (2004).
- [117] H. Fine, M. E. and Van Duyne and N. T. Kenney, *J. Appl. Phys.* **25**, 402–405 (1954).
- [118] S. Hunklinger, *Proceedings IEEE Ultrasonics Symposium* 493–501 (1974).
- [119] D. Tielbürger, R. Merz, R. Ehrenfels *et al.*, *Phys. Rev. B* **45**, 2750–2760 (1992).
- [120] R. Vacher, E. Courtens and M. Foret, *Phys. Rev. B* **72**, 214205–1–214205–11 (2005).
- [121] SCHOTT ML GmbH (Kristallzucht Eisenberg, Germany).
- [122] S. Hunklinger and W. Arnold, *Physical Acoustics: Principles and Methods*, Vol. 12, Chapter: Ultrasonic Properties of Glasses at Low Temperatures, 155–215 (New York: Academic Press, 1976).
- [123] S. Hunklinger and M. v. Schickfus, *Amorphous Solids: Low-Temperature Properties*, Vol. 24 of *Topics in Current Physics* (Springer, Berlin, 1981).
- [124] O. L. Anderson and H. E. Bömmel, *J. Am. Ceram. Soc.* **38**, 125–131 (1955).
- [125] R. E. Strakna, *Phys. Rev.* **123**, 2020–2026 (1961).
- [126] M. R. Vukceovich, *J. Non-Cryst. Solids* **11**, 25–63 (1972).
- [127] A. S. Nowick and B. S. Berry, *IBM J. Res. Dev.* **5**, 297–311 (1961).
- [128] A. Schroeter, R. Nawrodt, R. Schnabel *et al.*, *arXiv:0709.4359v1 [gr-qc]*, submitted to *Class. Quantum Grav.* (2007).
- [129] C. Braxmaier, O. Prادل, H. Müller *et al.*, *Phys. Rev. D* **64**, 042001–1–042001–11 (2001).
- [130] J. Volger, J. M. Stevels and C. van Amerongen, *Philips Res. Rep.* **10**, 261–280 (1955).
- [131] H. E. Bömmel, W. P. Mason and A. W. Warner, *Phys. Rev.* **102**, 64–71 (1956).
- [132] R. K. Cook and J. H. Wasilik, *J. Appl. Phys.* **27**, 836–837 (1956).
- [133] J. H. Wasilik, *Phys. Rev.* **105**, 1174–1180 (1957).
- [134] J. C. King, *Phys. Rev.* **109**, 1552–1553 (1958).

- [135] J. C. King, R. A. Laudise and A. A. Ballman, *J. Phys. Chem. Solids* **23**, 1019–1021 (1962).
- [136] D. B. Fraser, *J. Appl. Phys.* **35**, 2913–2918 (1964).
- [137] A. Seed, *Brit. J. Appl. Phys.* **16**, 87–91 (1965).
- [138] A. Zimmer, R. Nawrodt, T. Koettig *et al.*, *Rev. Sci. Instrum.* **78**, 063905–1–063905–8 (2007).
- [139] A. Smakula and V. Sils, *Phys. Rev.* **99**, 1744–1746 (1955).
- [140] R. Bechmann, *Phys. Rev.* **110**, 1060–1061 (1958).
- [141] SCHOTT AG, Division SCHOTT Lithotec (Jena), url: <http://www.schott.com/lithotec/english/>.
- [142] D. B. Fraser, *Physical Acoustics: Principles and Methods*, Vol. V, Chapter: Impurities and Anelasticity in Crystalline Quartz, 59–110 (New York: Academic Press, 1968).
- [143] W. E. Bron, *Phys. Rev. B* **21**, 2627–2629 (1980).
- [144] H. Bahadur, *IEEE Trans. Ultrason. Ferroelectr. Freq. Control* **41**, 820–833 (1994).
- [145] H. Bahadur, *IEEE International Ultrasonics, Ferroelectrics, and Frequency Control Joint 50th Anniversary Conference* 651 (2004).
- [146] S. P. Doherty, J. J. Martin, A. F. Armington *et al.*, *J. Appl. Phys.* **51**, 4164–4168 (1980).
- [147] J. J. Martin, *J. Appl. Phys.* **56**, 2536–2540 (1984).
- [148] J. J. Martin, *IEEE Trans. Ultrason. Ferroelectr. Freq. Control* **35**, 288–296 (1988).
- [149] J. J. Martin, L. E. Halliburton and R. B. Bossoli, *Proc. 35th Ann. Freq. Control Symposium* 317 (1981).
- [150] J. J. Martin, *1996 IEEE International Frequency Control Symposium* 170 (1996).
- [151] P. Amico, L. Bosi, L. Carbone *et al.*, *Rev. Sci. Instrum.* **73**, 179–184 (2002).
- [152] Z. Yan, L. Ju, S. Gras *et al.*, *Eur. Phys. J.-Appl. Phys* **30**, 189–192 (2005).
- [153] K. Yamamoto, S. Miyoki, T. Uchiyama *et al.*, *Class. Quantum Grav.* **21**, S1075–S1081 (2004).
- [154] A. Zimmer, R. Nawrodt, D. Heinert *et al.*, *arXiv:0709.2124v1 [cond-mat.other]*, accepted for publication in *J. Phys.: Conf. Ser.* (2007).
- [155] D. R. Huffman and M. H. Norwood, *Phys. Rev.* **117**, 709–711 (1960).
- [156] R. Baumgartner, M. Engelhardt and K. F. Renk, *Phys. Rev. Lett.* **47**, 1403–1407 (1981).

- [157] A. D. Franklin, J. M. Crissman and K. F. Young, *J. Phys. C: Solid State Phys.* **8**, 1244–1266 (1975).
- [158] D. L. Staebler and S. E. Schnatterly, *Phys. Rev. B* **3**, 516–527 (1971).
- [159] C. G. Andeen, J. J. Fontanella, M. C. Wintersgill *et al.*, *J. Phys. C: Solid State Phys.* **14**, 3557–3574 (1981).
- [160] C. Andeen, D. Link and J. Fontanella, *Phys. Rev. B* **16**, 3762–3767 (1977).
- [161] C. Andeen and J. Fontanella, *J. Phys. Chem. Solids* **38**, 237–241 (1977).
- [162] J. Fontanella, C. Andeen and D. Schuele, *Phys. Rev. B* **17**, 3429–3433 (1978).
- [163] S. Rowan, J. Hough and D. R. M. Crooks, *Phys. Lett. A* **347**, 25–32 (2005).
- [164] A. Bunkowski, O. Burmeister, P. Beyersdorf *et al.*, *Opt. Lett.* **29**, 2342–2344 (2004).
- [165] T. Clausnitzer, E. B. Kley, A. Tünnermann *et al.*, *Opt. Express* **13**, 4370–4378 (2005).
- [166] A. Bunkowski, O. Burmeister, T. Clausnitzer *et al.*, *Appl. Optics* **45**, 5795–5799 (2006).
- [167] R. Schnabel, A. Bunkowski, O. Burmeister *et al.*, *Opt. Lett.* **31**, 658–660 (2006).
- [168] H. J. McSkimin and P. Andreatch, *J. Appl. Phys.* **35**, 3312–3319 (1964).
- [169] C. C. Lam and D. H. Douglass, *J. Low Temp. Phys.* **44**, 259–264 (1981).
- [170] C. C. Lam, *Study of the internal friction in single crystal silicon*, Ph.D. thesis, University of Rochester, Rochester, New York (1979).
- [171] G. D. Watkins and J. W. Corbett, *Phys. Rev.* **121**, 1001–1014 (1961).
- [172] B. S. Berry, *Bull. Am. Phys. Soc.* **24**, 252–252 (1979).
- [173] J. Coutinho, O. Andersen, L. Dobaczewski *et al.*, *Phys. Rev. B* **68**, 184106–1–184106–11 (2003).
- [174] P. Johannesen, B. B. Nielsen and J. R. Byberg, *Phys. Rev. B* **61**, 4659–4666 (2000).
- [175] M. Pomerantz, *Phys. Rev. B* **1**, 4029–4036 (1970).
- [176] Siltronic AG, url: <http://www.siltronic.com/>.
- [177] C. C. Lam and D. H. Douglass, *Phys. Lett. A* **85**, 41–42 (1981).
- [178] E. Sigmund and K. Lassmann, *Phys. Status Solidi B-Basic Solid State Phys.* **111**, 631–637 (1982).
- [179] T. N. Morgan, *Phys. Rev. Lett.* **24**, 887–890 (1970).

- [180] J. Maier and E. Sigmund, *Phys. Rev. B* **34**, 1148–1159 (1986).
- [181] Pro/ENGINEER, url: <http://www.ptc.com>.
- [182] J. R. Smith, G. Cagnoli, D. R. M. Crooks *et al.*, *Class. Quantum Grav.* **21**, S1091–S1098 (2004).
- [183] G. M. Harry, M. R. Abernathy, A. E. Becerra-Toledo *et al.*, *Class. Quantum Grav.* **24**, 405–415 (2007).
- [184] G. M. Harry, H. Armandula, E. Black *et al.*, *Appl. Optics* **45**, 1569–1574 (2006).
- [185] S. D. Penn, P. H. Sneddon, H. Armandula *et al.*, *Class. Quantum Grav.* **20**, 2917–2928 (2003).
- [186] G. M. Harry, A. M. Gretarsson, P. R. Saulson *et al.*, *Class. Quantum Grav.* **19**, 897–917 (2002).
- [187] R. Nawrodt, A. Zimmer, T. Koettig *et al.*, *New J. Phys.* **9**, 225 1–9 (2007).
- [188] I. Martin, H. Armandula, C. Comet *et al.*, *submitted to Phys. Rev. Lett.* (2007).
- [189] T. Koettig, S. Moldenhauer, R. Nawrodt *et al.*, *Cryogenics* **46**, 888–891 (2006).
- [190] J. Degallaix, C. Zhao, L. Ju *et al.*, *J. Phys.: Conf. Ser.* **32**, 404–412 (2006).
- [191] D. F. Mcguigan, C. C. Lam, R. Q. Gram *et al.*, *J. Low Temp. Phys.* **30**, 621–629 (1978).

Zusammenfassung

Ziel dieser Arbeit war es, die mechanischen Verluste von potentiellen Substratmaterialien für die Spiegel zukünftiger kryogener interferometrischer Gravitationswellendetektoren (IGWD) zu untersuchen. Da mechanische Verluste mit thermischem Rauschen in diesen äußerst sensitiven Detektoren in Zusammenhang stehen, bietet eine systematische Analyse derselben die Möglichkeit, gezielte Maßnahmen zur Rauschreduzierung zu ergreifen und damit die Detektionswahrscheinlichkeit von Gravitationswellen zu steigern, sowie die technischen Erfordernisse für eine Astronomie basierend auf Gravitationswellen zu schaffen. Eine solche Gravitationswellenastronomie böte Informationen über das Universum, die aktuell mittels der Detektion elektromagnetischer Strahlung nicht zugänglich sind. Gravitationswellen wechselwirken äußerst schwach mit Materie und tragen daher von der durchlaufenen Umgebung weitgehend unbeeinflusste Informationen mit sich. Dieser Vorteil wirkt sich auf der anderen Seite als Nachteil in ihrer Detektion aus. Der Effekt einer Gravitationswelle mit großer Amplitude ist eine relative Längenänderung von ungefähr 10^{-20} auf der Erde [10].

Ein vielversprechender Weg zur Reduzierung des thermischen Rauschens in den derzeit bei Raumtemperatur betriebenen IGWDs ist der Entzug von thermischer Energie durch Kühlen der Spiegel und Strahlteiler. Da die mechanischen Verluste jedoch im allgemeinen sowohl von der Frequenz als auch von der Temperatur abhängen, werden Materialien für diese optischen Komponenten benötigt, die sehr geringe Verluste bei kryogenen Temperaturen zeigen. Fused silica, als Material der bei Raumtemperatur betriebenen IGWDs, und kristalliner Quarz, kristallines Calciumfluorid und kristallines Silizium, als potentielle verlustarme Materialien, wurden in dieser Arbeit untersucht. Dazu wurde eine neuartige mechanische Spektroskopie entwickelt ('cryogenic resonant acoustic (CRA) spectroscopy of bulk materials'), basierend auf etablierten Methoden. CRA Spektroskopie ist eine hoch sensitive Methode, da die Messung der mechanischen Güten der Proben völlig kontaktfrei abläuft. Als Bemerkung sei eingefügt, dass die mechanischen Güten das Reziproke der mechanischen Verluste bei den Resonanzen der Probekörper sind. Die Standzeiten eines nach Maß angefertigten Kryostaten erlauben die Messung von Gütewerten von bis zu 3×10^{10} in der aktuellen Konfiguration. Dabei ist eine hohe Temperaturstabilität und quasi störungsfreie Messung im Bereich von 5 K bis 325 K durch den in einem Speziallabor aufgestellten Kryostaten gewährleistet. Insgesamt sticht CRA Spektroskopie mit diesen Fähigkeiten im internationalen Feld hervor. Es gibt nur sehr wenige Gruppen, die Messungen mit vergleichbarer Auflösung über einen so großen Temperaturbereich

durchgeführt haben, und auch dies nicht systematisch [153, 191].

Im Vorfeld der Messung wurden die Proben auf ihre Strukturdynamik mittels der auf der Finite Elemente Methode basierenden Software ANSYS hin untersucht. Somit konnten Moden aufgrund ihrer Modenform ausgewählt und gezielt angeregt werden. Da einige Verlustprozesse in kristallinem Quarz bekannt sind, konnte unsere Meßmethode anhand ihrer erfolgreich überprüft werden. Auch konnte mittels der Variation der Geometrie der Proben gezeigt werden, dass tatsächlich intrinsische Verlustprozesse bzw. Relaxationsprozesse beobachtet werden.

Zur Interpretation der gemessenen temperatur- und frequenzabhängigen Gütewerte wurden im Rahmen dieser Arbeit Modelle zur Beschreibung der mechanischen Verlustprozesse erarbeitet und auf die untersuchten Materialien zugeschnitten. Ferner sollen es diese Modelle in Zukunft ermöglichen, mittels der durch systematische Gütemessungen gewonnenen Relaxationsparameter Rückschlüsse auf die mechanischen Verluste im Detektionsfrequenzbereich der IGWDs, welcher niedriger als die Resonanzfrequenzen der Probekörper liegt, zu ziehen.

Fused silica stellte sich bei unseren Messungen als für kryogene Systeme nicht geeignet heraus. Seine amorphe Struktur beinhaltet eine Variabilität, die eine Vielzahl von Relaxationsprozessen mit leicht abweichenden Parametern zur Folge hat, welche sich als hohes und breites Verlustmaximum bei 20 K bemerkbar machen. Dieses Verlustmaximum konnte gut durch Relaxationsprozesse in asymmetrischen Doppelmuldenpotentialen beschrieben werden. Wenn auch Fused Silica nicht als Substratmaterial für die optischen Komponenten kryogener IGWDs in Frage kommt, so ist das Modell der Verluste amorpher Festkörper durchaus weiterhin interessant. Die Spiegel benötigen für ihre Funktionsfähigkeit neben dem Substrat eine optische (dielektrische) Beschichtung, welche von amorpher Struktur ist. Während der letzten Jahre konzentrierten sich auf internationaler Ebene viele Gruppen darauf, die mechanischen Verluste dieser optischen Funktionsschichten zu untersuchen [183–186]. Auch wir erweiterten unseren Forschungsbereich in diese Richtung [187, 188].

Das Fazit der Untersuchung der mechanischen Verluste von Fused Silica bei tiefen Temperaturen ist, sich für kryogene Anwendungen kristallinen Materialien zuzuwenden, da dort die in amorphen Festkörpern vorhandene Strukturvariabilität nicht gegeben ist. So wies das kristalline Gegenstück zu Fused Silica bei Raumtemperatur ähnliche Verluste auf, bei tiefen Temperaturen jedoch zeigten sich kleinere, weitaus schmalere Verlustpeaks. Über den gesamten Temperaturbereich hinweg wurde die Dämpfungskurve von Verlustprozessen, induziert von Wechselwirkungen der angeregten akustischen Welle mit thermischen Phononen des Festkörpers, bestimmt. Dieses Verhalten zeigte sich ebenfalls bei den Materialien Calciumfluorid und Silizium. Da diese Phonon-Phonon-Wechselwirkung auch in defektfreien Materialien auftritt und

somit nicht signifikant durch den Reinheitsgrad des Materiales gesteuert werden kann, kommt ihr besondere Bedeutung zu. Die Modellierung der Phononinduzierten Verluste gestaltete sich einerseits schwierig, da die Verlustprozesse zwar qualitativ bekannt sind, es jedoch trotz intensiver Forschung in der Vergangenheit an quantitativen Beschreibungsmöglichkeiten mangelt. Auch wurden bisherige Experimente eher bei hohen Frequenzen, ab dem MHz-Bereich, durchgeführt und dementsprechende Modelle betrachtet. Andererseits gelang uns die Beschreibung der Phonon-Phonon Wechselwirkung mittels ähnlicher Parameter wie denen von defektinduzierten Verlusten. Dissipation, also Entzug von Schwingungsenergie, tritt im Zusammenhang mit Defekten bei einer spannungsinduzierten Umverteilung in Doppelmuldenpotentialen auf.

In kristallinem Quarz konnten Verlustpeaks Relaxationsprozessen verursacht durch Alkali-Ionen zugeschrieben werden. Ferner wurden Dämpfungspeaks entdeckt, deren Ursache bisher unbekannt ist, deren Relaxationsparameter jedoch auf ebenfalls defektinduzierte Verluste hindeuten. Daher sind in Zukunft weitere Untersuchungsmethoden wie Infrarotspektroskopie und Massenspektrometrie hinzuzuziehen. Aber auch der Ansatz des Zusammenhanges zwischen der Defektsymmetrie und dem Auftreten von Verlusten ist vielversprechend. Mittels Auswahlregeln ist es somit prinzipiell möglich, von der Variation der Relaxationsstärke mit der Modenform auf die Defektsymmetrie zurück zu schließen. Insgesamt konnten die gemessenen Dämpfungskurven sowohl für z-cut als auch für x-cut Quarz mit hoher Genauigkeit reproduziert werden. Das zugrundeliegende Modell beinhaltet die Parameter Relaxationsstärke und Relaxationszeit, unter Berücksichtigung auftretender Hintergrundverluste durch z.B. die Halterung der Proben. Die Relaxationsstärke hängt sowohl von der Frequenz als auch von der Temperatur ab. Die Relaxationszeit ändert sich ebenfalls mit der Temperatur. In einem iterativen Vorgang, unter Einbeziehung aller gemessenen Dämpfungskurven an dem jeweiligen Material, wurden die Relaxationsparameter durch ein Anpassen der berechneten an die gemessene Kurve erhalten.

Die Verluste von kristallinem Quarz sind recht niedrig, es wurden Güten von bis zu 1×10^8 bei 5 K gemessen. Auch erscheint es möglich, die Verluste um 70 K durch größere Reinheit, Bestrahlung des Materials oder Austauschen der Alkali-Ionen gegen andere Ionen wie Protonen weiter zu senken. Jedoch sprechen die an Calciumfluorid und Silizium gemessenen höheren Güten bei für kryogene IGWDs praktikabel zu vertretenden Temperaturen zunächst für diese Materialien.

Für Calciumfluorid (100) wurde ein Höchstwert von 3×10^8 bei 64 K beobachtet. Unterhalb dieser Temperatur wurden für drei ausgewählte Moden übereinstimmend in den Dämpfungskurven zahlreiche Relaxationsprozesse lokalisiert. Die Relaxationsparameter, insbesondere die niedrigen Aktivierungsenergien, deuten auf elektronische Umordnungsprozesse hin. Unter 64 K werden die mechanischen Verluste mit

abnehmender Temperatur zunehmend durch thermoelastische Verlustprozesse dominiert. Diese schmälern die Bedeutung von Calciumfluorid als zukünftigem Substratmaterial.

Silizium hingegen weist sogar zwei Nulldurchgänge des thermischen Expansionskoeffizienten bei 18 K und 123 K auf, wodurch auch die thermoelastischen Verluste bei diesen Temperaturen verschwinden. Zudem weist Silizium gute thermische Eigenschaften wie eine sehr hohe Wärmeleitfähigkeit auf. 18 K wäre eine realistische Temperatur für kryogene IGWDs, die auch durch Pulsationsröhrenkühler erreicht werden könnte [189]. Bei dieser Temperatur wurden an einer Bor-dotierten Siliziumproben in (111) Orientierung hohe Güten von $1,5 \times 10^8$ gemessen. Auch Silizium (100), ebenfalls Bor-dotiert, zeigte sehr hohe Güten. Die Messung einer Probe unbekannter Dotierung ergab niedrigere Gütewerte. Die Auswertung der Dämpfungskurven für drei Moden legt eine Phosphor-Dotierung nahe. Ferner wurden Relaxationsprozesse in Zusammenhang mit Sauerstoff-Komplexen identifiziert. Der hohe Sauerstoffgehalt erklärt sich durch die Kristallzüchtung im Czochralski-Prozess. Um die Stärke dieser Verlustprozesse zu verringern, ist daher eine Methode zu bevorzugen, die weniger Sauerstoff in den Kristall einbringt, wie das Float-Zone-Verfahren. Insgesamt bietet Silizium interessante Möglichkeiten, Verlustprozesse dotierungs- und orientierungsabhängig zu untersuchen.

Auch durch seine herausragende Stellung in der Halbleiterindustrie vereint es für kryogene IGWDs geeignete Eigenschaften von der Erhältlichkeit in hoher Reinheit und ausreichender Größe als Einkristall bis hin zu wirtschaftlichen Faktoren wie der Bezahlbarkeit des Materials. Allein die bisherige transmissive Interferometertopologie bei einer Laserwellenlänge von 1064 nm wäre nicht mehr realisierbar, was jedoch kein Problem darstellt, da entweder der Betrieb bei 1550 nm stattfinden oder zukünftig eine nicht-transmissive Topologie verwendet werden könnte [164–167]. Ein negativer Einfluß eines Beugungsgitters auf die mechanische Güte wurde in unseren Messungen nicht festgestellt [187]. Eine nicht-transmissive Interferometertopologie hätte zudem den Vorteil, weniger Energie des Lasers in das Material einzubringen und somit das thermische Rauschen zusätzlich zu senken. Alternative Materialien zu Silizium sind Saphir, Siliziumkarbid und Diamant. Die beiden zuletzt genannten Materialien sind allerdings nicht als Einkristalle ausreichender Größe erhältlich. Saphir hingegen weist höhere thermoelastische Verluste über das gesamte Temperaturspektrum auf [190]. Die Berechnung des Brownschen Anteils des thermischen Rauschens der Spiegelsubstrate mittels der Methode von Levin unter Berücksichtigung der höchsten gemessenen Gütewerte ergab für Silizium (111) als Favoriten eine Erhöhung der Detektionsempfindlichkeit um zwei Größenordnungen bei einer Betriebstemperatur des IGWDs von 18 K.

Appendix

The interrelations between J_1 and J_2 respectively M_1 and M_2 (Kramers-Kronig relations) are:

$$J_1(f) - J_U = \frac{2}{\pi} \int_0^{\infty} J_2(a) \frac{a da}{a^2 - (2\pi f)^2}, \quad (\text{A.1})$$

$$J_2(f) = \frac{2(2\pi f)}{\pi} \int_0^{\infty} [J_1(a) - J_U] \frac{da}{(2\pi f)^2 - a^2}, \quad (\text{A.2})$$

$$M_1(f) - M_R = \frac{2(2\pi f)^2}{\pi} \int_0^{\infty} \frac{M_2(a)}{a} \frac{2\pi f da}{(2\pi f)^2 - a^2}, \quad (\text{A.3})$$

$$M_2(f) = \frac{2}{\pi} \int_0^{\infty} [M_1(a) - M_R] \frac{2\pi f da}{a^2 - (2\pi f)^2}. \quad (\text{A.4})$$

The relationship between the mechanical loss ϕ and the attenuation \mathcal{A} is given by:

$$\phi = \frac{2v_s}{2\pi f} \mathcal{A} (\text{nepers/m}), \quad (\text{A.5})$$

$$\phi = \frac{0.23v_s}{2\pi f} \mathcal{A} (\text{dB/m}). \quad (\text{A.6})$$

v_s is the (averaged) velocity in the medium

Elastic stiffness constants for the cubic system:

$$c_{cubic} = \begin{pmatrix} c_{11} & c_{12} & c_{12} & 0 & 0 & 0 \\ c_{12} & c_{11} & c_{12} & 0 & 0 & 0 \\ c_{12} & c_{12} & c_{11} & 0 & 0 & 0 \\ 0 & 0 & 0 & c_{44} & 0 & 0 \\ 0 & 0 & 0 & 0 & c_{44} & 0 \\ 0 & 0 & 0 & 0 & 0 & c_{44} \end{pmatrix}. \quad (\text{A.7})$$

The elastic compliance constants for the cubic system are of equal form.

Elastic stiffness constants for the trigonal system (classes $3m, 32, \bar{3}m$):

$$c_{trigonal} = \begin{pmatrix} c_{11} & c_{12} & c_{13} & c_{14} & 0 & 0 \\ c_{12} & c_{11} & c_{13} & -c_{14} & 0 & 0 \\ c_{13} & c_{13} & c_{33} & 0 & 0 & 0 \\ c_{14} & -c_{14} & 0 & c_{44} & 0 & 0 \\ 0 & 0 & 0 & 0 & c_{44} & c_{14} \\ 0 & 0 & 0 & 0 & c_{14} & 1/2(c_{11} - c_{12}) \end{pmatrix}. \quad (\text{A.8})$$

Elastic compliance constants for the trigonal system (classes $3m, 32, \bar{3}m$):

$$s_{trigonal} = \begin{pmatrix} s_{11} & s_{12} & s_{13} & s_{14} & 0 & 0 \\ s_{12} & s_{11} & s_{13} & -s_{14} & 0 & 0 \\ s_{13} & s_{13} & s_{33} & 0 & 0 & 0 \\ s_{14} & -s_{14} & 0 & s_{44} & 0 & 0 \\ 0 & 0 & 0 & 0 & s_{44} & 2s_{14} \\ 0 & 0 & 0 & 0 & 2s_{14} & 2(s_{11} - s_{12}) \end{pmatrix}. \quad (\text{A.9})$$

In the following, relations between the compliances and the stiffnesses are given [47].

Cubic system:

$$c_{11} = \frac{s_{11} + s_{12}}{(s_{11} - s_{12})(s_{11} + 2s_{12})}, \quad (\text{A.10})$$

$$c_{11} = \frac{-s_{12}}{(s_{11} - s_{12})(s_{11} + 2s_{12})}, \quad (\text{A.11})$$

$$c_{44} = 1/s_{44}. \quad (\text{A.12})$$

Trigonal system (classes $3m, 32, \bar{3}m$):

$$c_{11} + c_{12} = s_{33}/s, \quad (\text{A.13})$$

$$c_{11} - c_{12} = s_{44}/s', \quad (\text{A.14})$$

$$c_{13} = -s_{13}/s, \quad (\text{A.15})$$

$$c_{14} = -s_{14}/s', \quad (\text{A.16})$$

$$c_{33} = (s_{11} + s_{12})/s, \quad (\text{A.17})$$

$$c_{44} = (s_{11} - s_{12})/s', \quad (\text{A.18})$$

$$\text{where } s = s_{33}(s_{11} + s_{12}) - 2s_{13}^2 \quad (\text{A.19})$$

$$\text{and } s' = s_{44}(s_{11} - s_{12}) - 2s_{14}^2. \quad (\text{A.20})$$

The relationships between the elastic constants and moduli (for cubic materials) are:

$$\text{bulk modulus: } B = \frac{1}{3}(c_{11} + 2c_{12}), \quad (\text{A.21})$$

$$\text{Young's modulus: } E = \frac{(c_{11} - c_{12})(c_{11} + 2c_{12})}{c_{11} + c_{12}}, \quad (\text{A.22})$$

$$\text{Poisson's ratio: } \nu = \frac{c_{12}}{c_{11} + c_{12}}, \quad (\text{A.23})$$

$$\text{shear modulus: } G = c_{44}. \quad (\text{A.24})$$

The elastic constants of isotropic materials can be calculated by:

$$c_{11} = \frac{E}{1 + \nu} \left(1 + \frac{\nu}{1 - 2\nu} \right), \quad (\text{A.25})$$

$$c_{12} = \frac{E}{1 + \nu} \frac{\nu}{1 - 2\nu}, \quad (\text{A.26})$$

$$c_{12} = \frac{E}{1 + \nu} = G. \quad (\text{A.27})$$

Tab. A.1: Effect of defect symmetry on principal values and principal axes of the λ tensor.

Defect symmetry	Principal values	Principal axes	No. of independent components of λ
Cubic	$\lambda_1 = \lambda_2 = \lambda_3$	arbitrary	1
Tetragonal, hexagonal, and trigonal	$\lambda_1 \neq \lambda_2 = \lambda_3$ or $\lambda_1 = \lambda_2 \neq \lambda_3$	axis 1 along major symmetry axis or axis 3 along major symmetry axis	2
Orthorhombic	$\lambda_1 \neq \lambda_2 \neq \lambda_3$	along the three symmetry axes	3
Monoclinic	$\lambda_1 \neq \lambda_2 \neq \lambda_3$	axis 1 or 3 along the symmetry axis	4
Triclinic	$\lambda_1 \neq \lambda_2 \neq \lambda_3$	unrelated to crystal axes	6

Tab. A.2: n_t for various defect symmetries.

Crystal	Defect				
	Tetragonal	Trigonal	Ortho- rhom- bic	Monoclinic	Triclinic
Cubic (O_h, T_d, O)	3	4	6	12	24
Cubic (T_h, T)	-	4	3	6	12
Trigonal (D_{3h}, C_{3v}, D_3)	-	1	-	3	6

Tab. A.3: Expression for $\lambda_{ij}^{(1)}$ in terms of principal values.

Crystal	Defect	$\lambda_{11}^{(1)}$	$\lambda_{22}^{(1)}$	$\lambda_{33}^{(1)}$	$\lambda_{23}^{(1)}$	$\lambda_{31}^{(1)}$	$\lambda_{12}^{(1)}$
Cubic	Tetragonal	λ_1	λ_2	λ_2	0	0	0
	Trigonal	λ_a	λ_a	λ_a	$\lambda_c/3$	$\lambda_c/3$	$\lambda_c/3$
	< 100 > orthorhombic	λ_1	λ_2	λ_3	0	0	0
	< 110 > orthorhombic	λ_b	λ_b	λ_3	0	0	$\lambda_c/2$
Trigonal	Monoclinic	λ_1	λ_f	λ_g	λ_k	0	0

The abbreviations used in Tab. A.3 are

$$\alpha = (\cos(\theta))^2, \quad (\text{A.28})$$

$$\beta = (\sin(\theta))^2, \quad (\text{A.29})$$

$$\lambda_a = (\lambda_1 + 2\lambda_2)/3, \quad (\text{A.30})$$

$$\lambda_b = (\lambda_1 + \lambda_2)/2, \quad (\text{A.31})$$

$$\lambda_c = \lambda_1 - \lambda_2, \quad (\text{A.32})$$

$$\lambda_f = \alpha\lambda_2 + \beta\lambda_3, \quad (\text{A.33})$$

$$\lambda_g = \beta\lambda_2 + \alpha\lambda_3, \quad (\text{A.34})$$

$$\lambda_k = \sqrt{\alpha\beta}(\lambda_2 - \lambda_3). \quad (\text{A.35})$$

Relaxation rates for different defect symmetries in cubic crystals:

Tetragonal defect:

$$\tau^{-1}(s_{11} - s_{12}) = 3\nu_{12} \quad (\text{A.36})$$

Trigonal defect:

$$\tau^{-1}(s_{44}) = 4\nu_{12} \quad (\text{A.37})$$

< 110 > orthorhombic defect:

$$\tau^{-1}(s_{11} - s_{12}) = 6\nu_{13} \quad (\text{A.38})$$

$$\tau^{-1}(s_{44}) = 2\nu_{12} + 4\nu_{13} \quad (\text{A.39})$$

< 100 > orthorhombic defect:

$$\tau^{-1}(s_{11} - s_{12}) = (v_{12} + 3v_{13} + v_{14} + v_{16}) \pm \left[v_{12}^2 + v_{14}^2 + v_{16}^2 - v_{12}v_{14} - v_{12}v_{16} - v_{14}v_{16} \right]^{1/2} \quad (\text{A.40})$$

< 110 > monoclinic defect:

$$\tau^{-1}(s_{11} - s_{12}) = 3(2v_{15} + v_{16} + v_{17}) \quad (\text{A.41})$$

$$\begin{aligned} \tau^{-1}(s_{44}) &= (v_{12} + 3v_{13} + 5v_{15} + 3/2v_{17}) \pm & (\text{A.42}) \\ &\pm \left[(v_{13} - v_{12} - v_{15} + 1/2v_{16} + 1/2v_{17})^2 + 2(v_{16} - v_{17}) \right]^{1/2} \end{aligned}$$

Frozen-free split:

In many cases, like for the triclinic effect in a trigonal crystal (Eq. 3.109), a defect can give rise to two or more relaxation times which may differ considerably from each other, and thus may be even decades apart in their magnitudes. Translated to temperatures this implies that the relaxation maxima appear at different temperatures, e. g., one at low temperatures and one at much higher temperatures. In the region between the loss peaks, the rate which gives rise to the low-temperature relaxation is high compared to the applied frequency. The corresponding reorientation occurs freely. On the other hand, the high-temperature relaxation rates are much lower than the applied frequency, resulting in frozen reorientations. Accordingly, the phenomenon of widely separated relaxations is named 'frozen-free split'.

A frozen-free split appears, if the elastic dipole does not have access to all of its n_t equivalent orientations via the dominant reorientation frequency. This frequency gives rise to a reorientation of the dipole only among a subset of all of its possible orientations, causing the low-temperature relaxation. The motion between equivalent subsets generates the high-temperature relaxation. Both relaxations have to be considered for the determination of the defect symmetry by the selection rules.

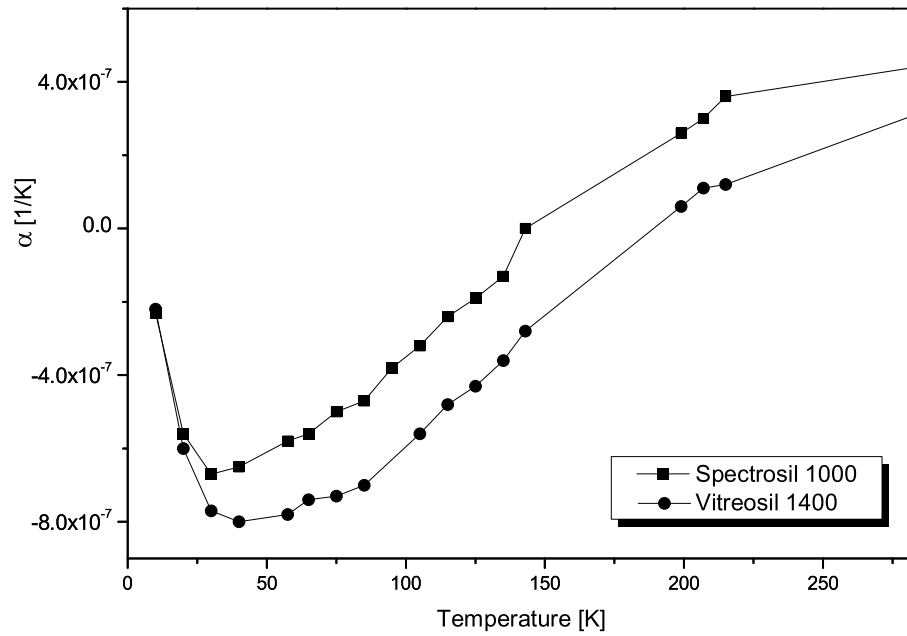


Fig. A.1: Linear thermal expansion coefficient of fused silica [1].

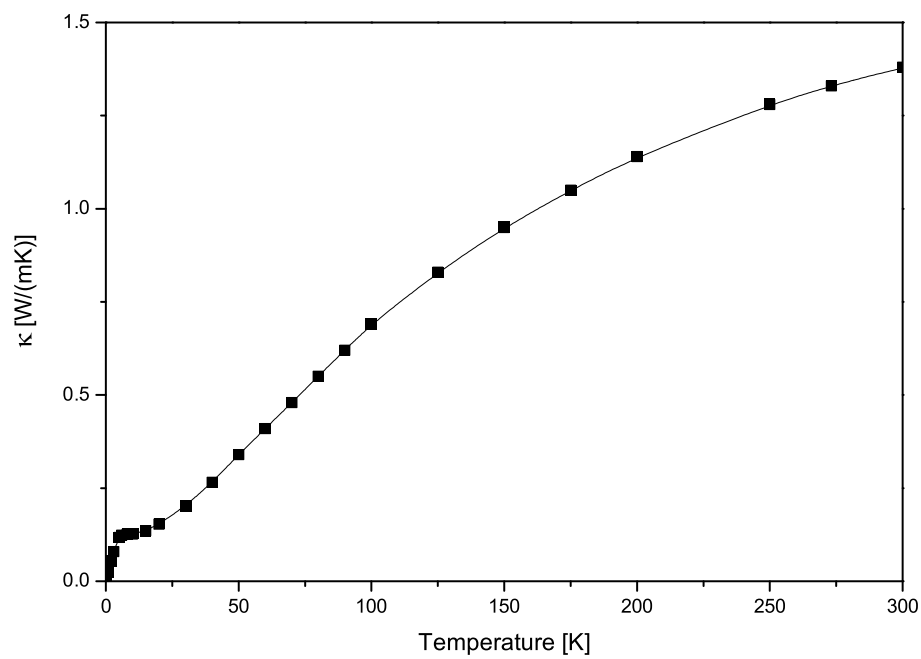


Fig. A.2: Thermal conductivity of fused silica [2].

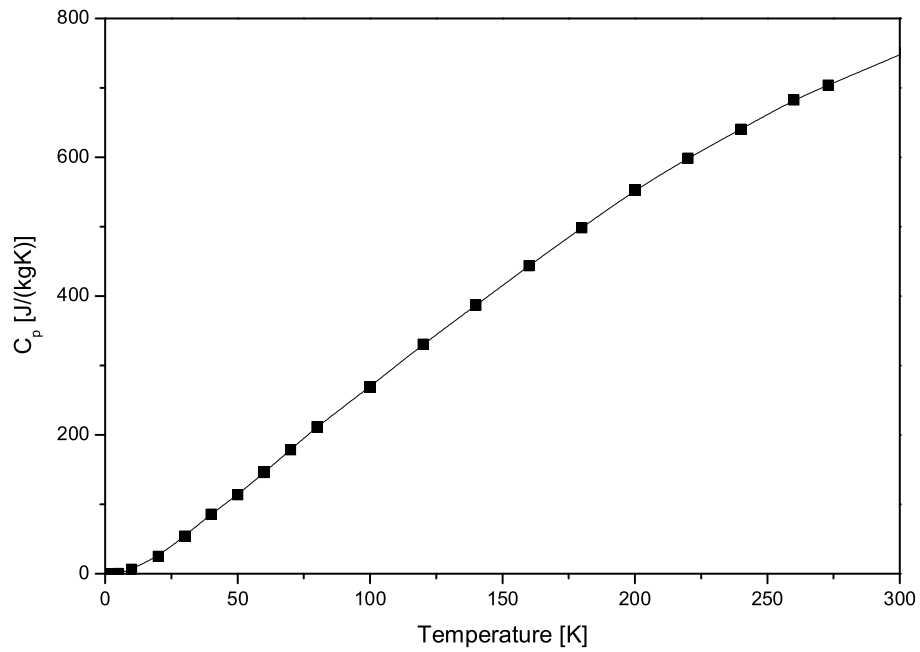


Fig. A.3: Specific heat capacity of fused silica [3].

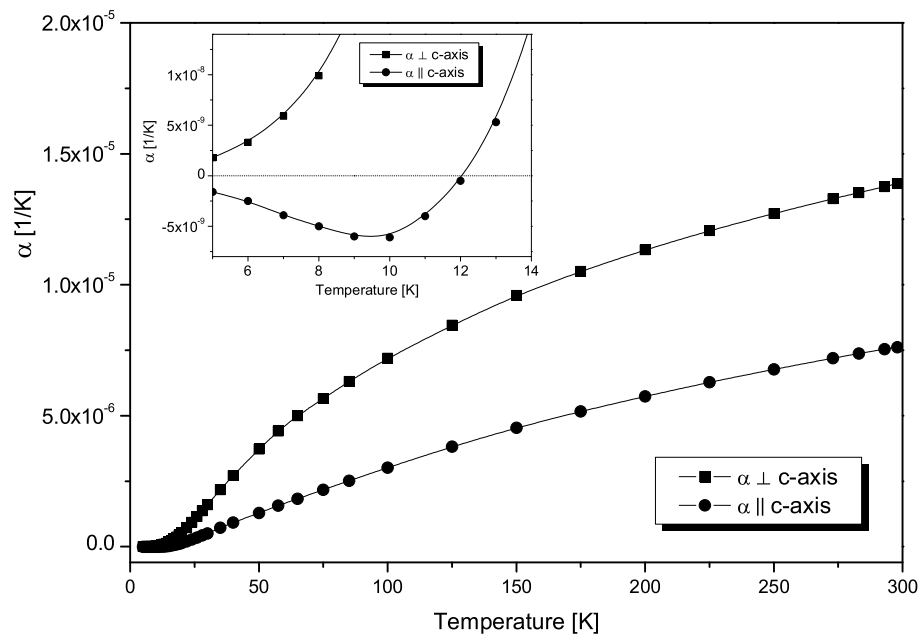


Fig. A.4: Linear thermal expansion coefficient of crystalline quartz [4].

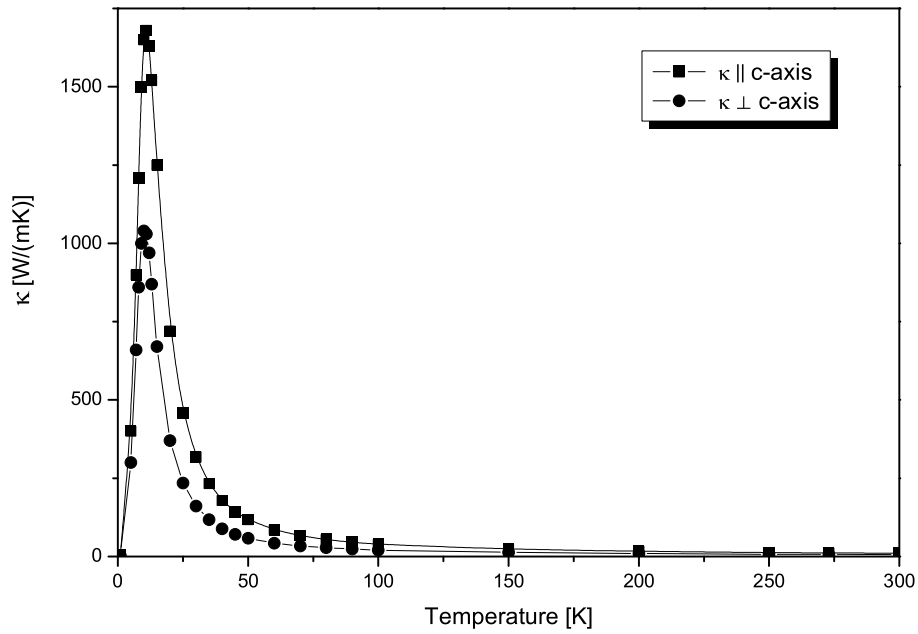


Fig. A.5: Thermal conductivity of crystalline quartz [2].

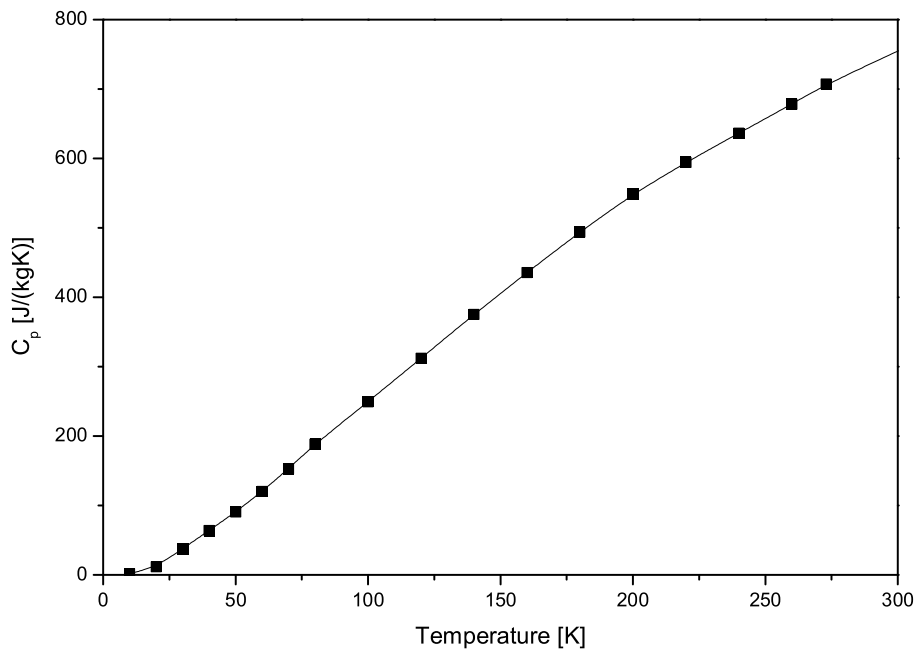


Fig. A.6: Specific heat capacity of crystalline quartz [3].

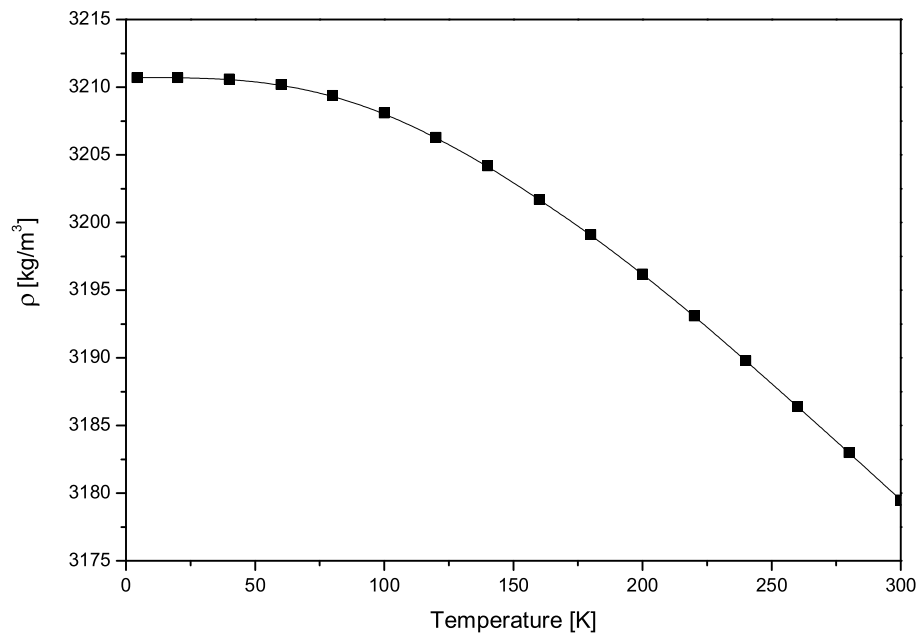


Fig. A.7: Density of calcium fluoride [5].

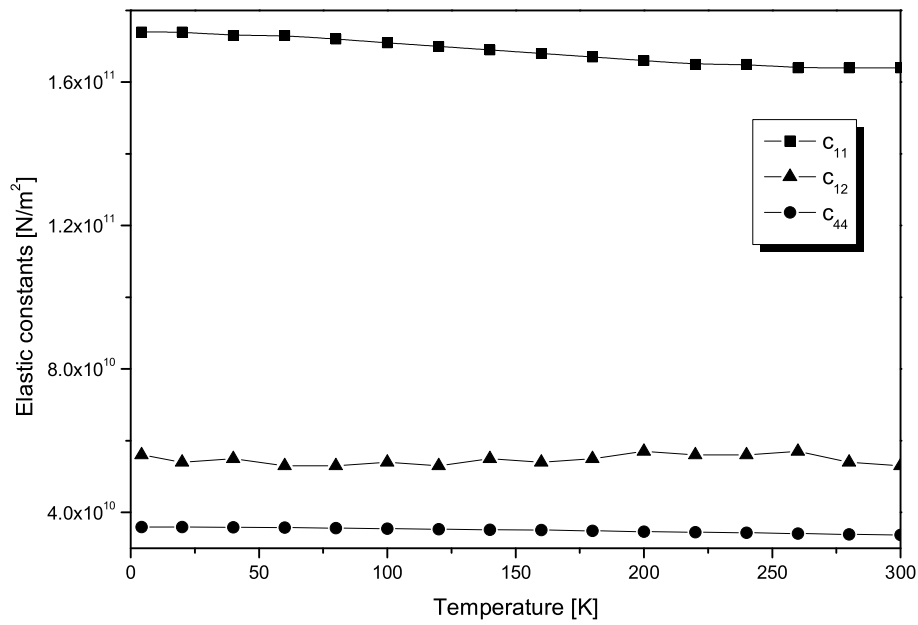


Fig. A.8: Elastic constants of calcium fluoride [5].

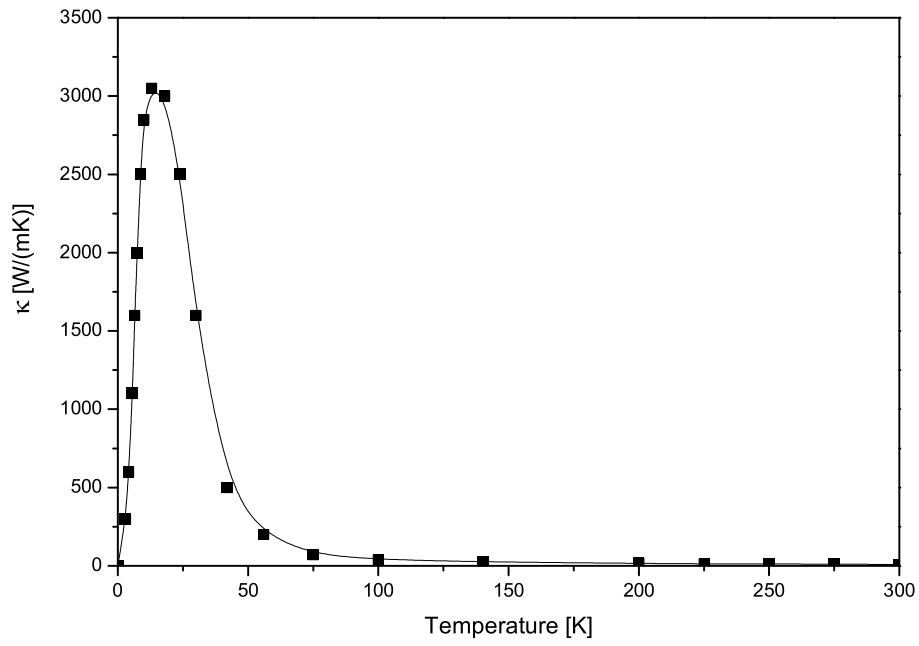


Fig. A.9: Thermal conductivity of calcium fluoride [6].

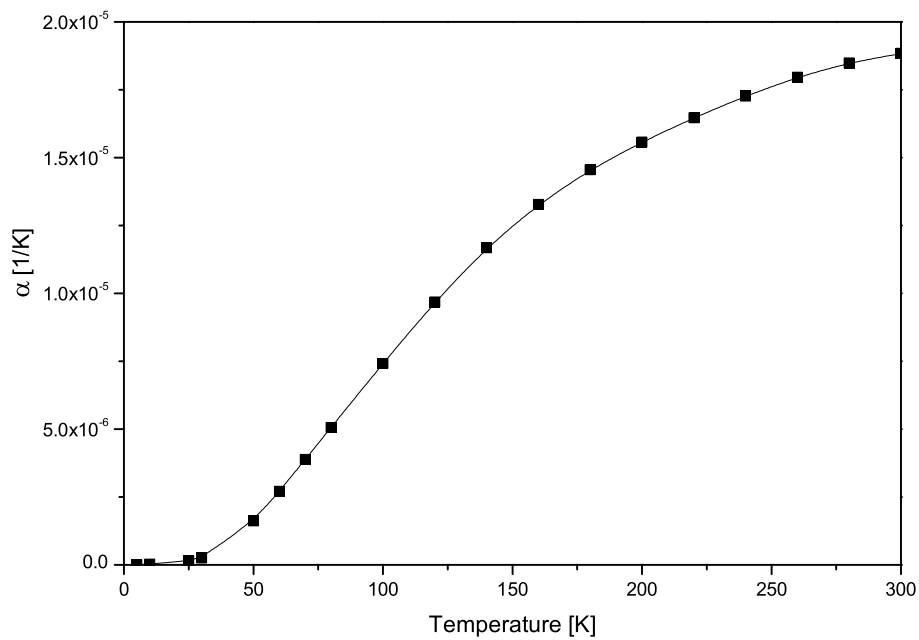


Fig. A.10: Linear thermal expansion coefficient of calcium fluoride [7, 8].

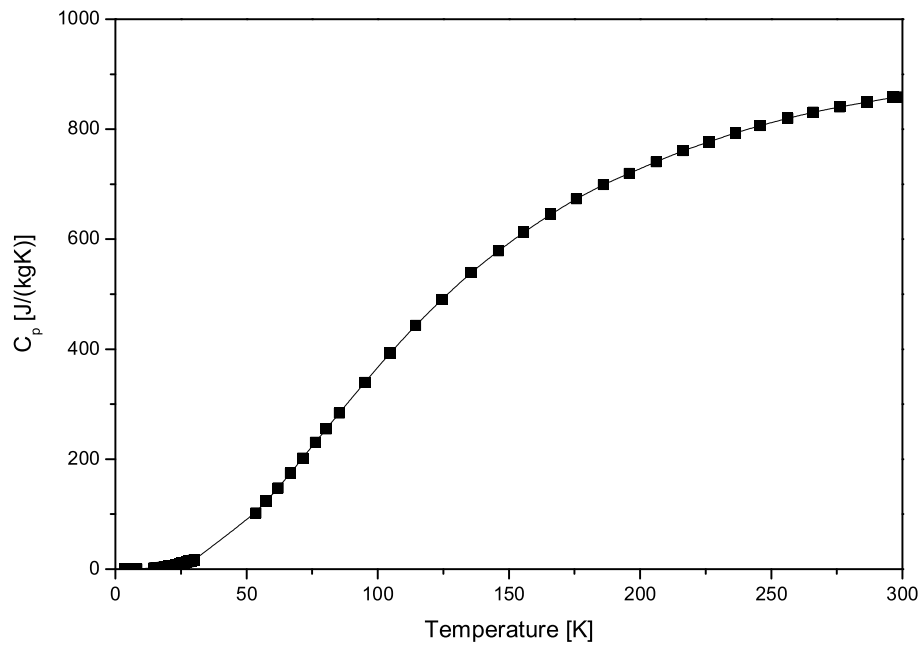


Fig. A.11: Specific heat capacity of calcium fluoride [5, 9].

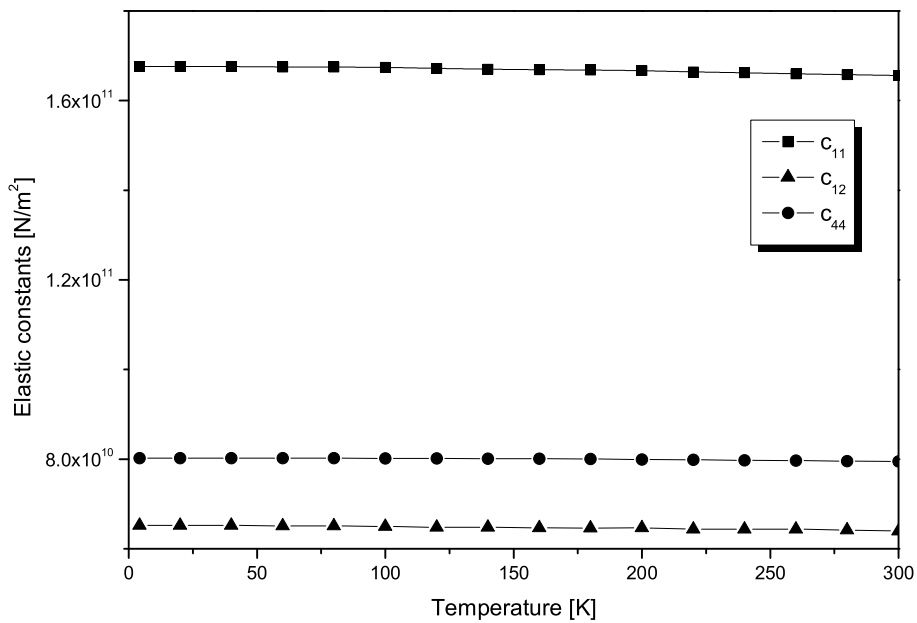


Fig. A.12: Elastic constants of pure silicon [10].

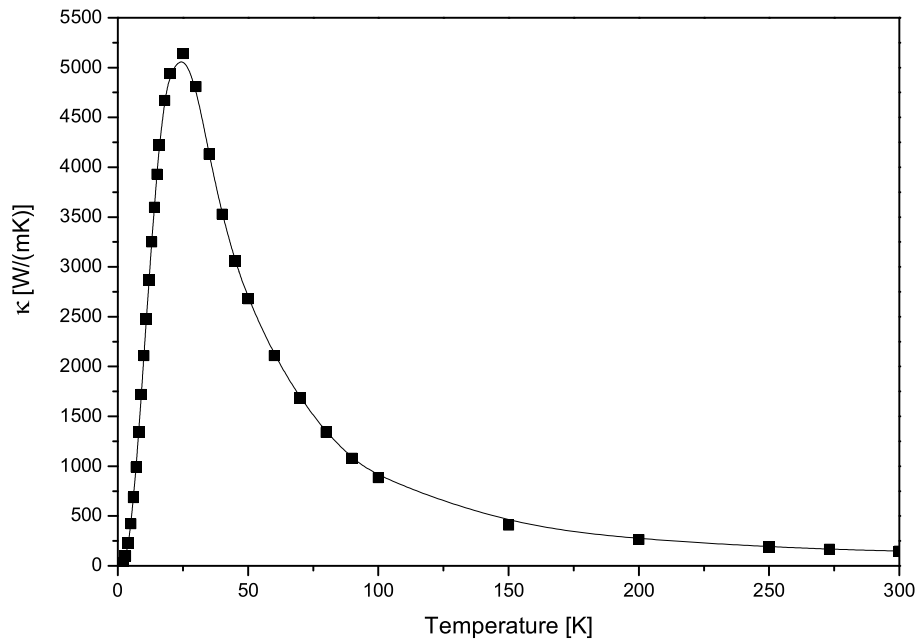


Fig. A.13: Thermal conductivity of high purity silicon [11].

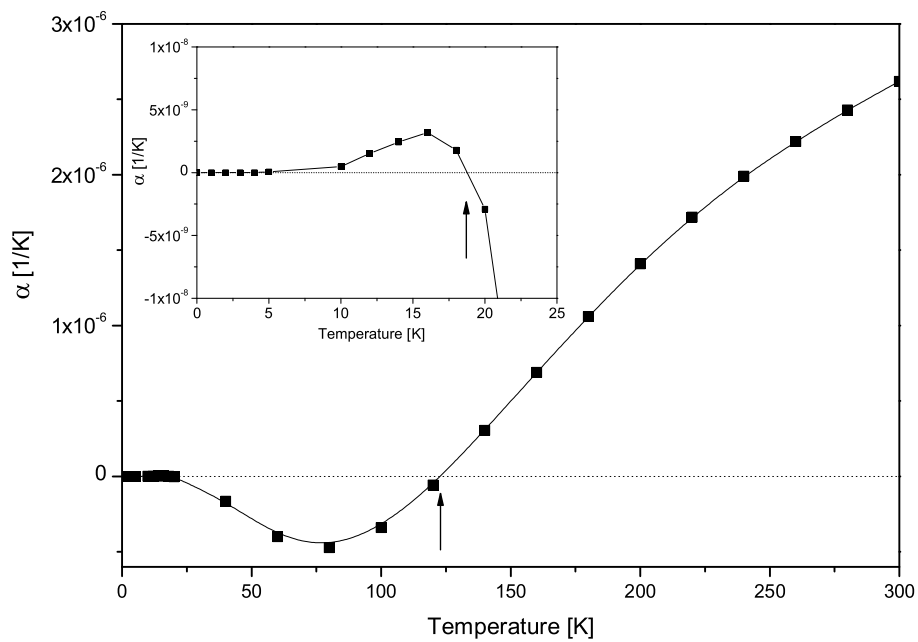


Fig. A.14: Linear thermal expansion coefficient of silicon [12].

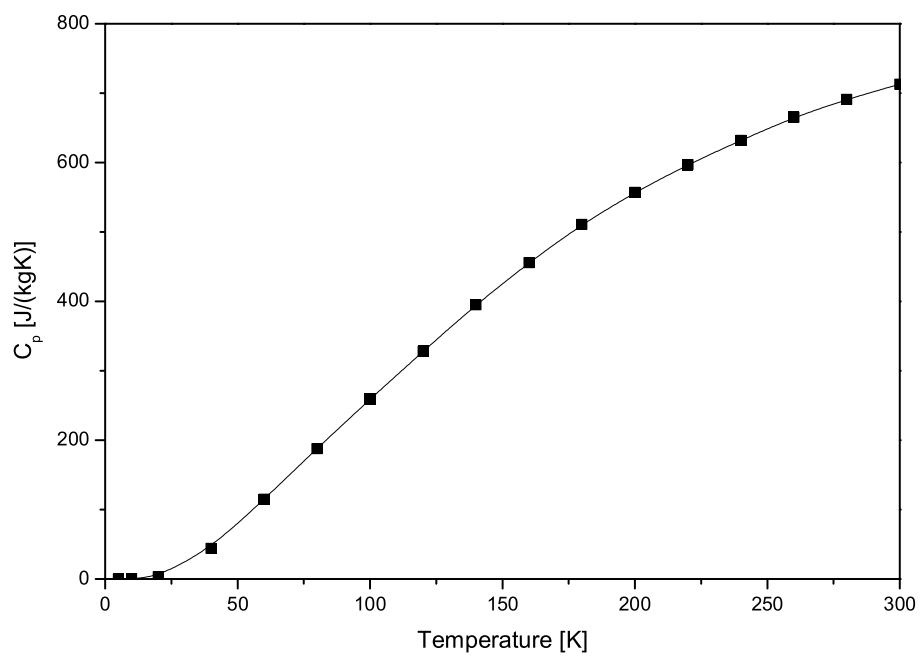


Fig. A.15: Specific heat capacity of silicon [12].

References Appendix

- [1] G. K. White, *J. Phys. D: Appl. Phys.* **6**, 2070–2078 (1973).
- [2] Y. S. Touloukian, R. W. Powell, C. Y. Ho *et al.* (eds.), *Thermophysical properties of matter (Thermal Conductivity, Nonmettalic Solids)*, Vol. 2 (New York - Washington: IFI/Plenum, 1970).
- [3] Y. S. Touloukian and E. H. Buyco (eds.), *Thermophysical properties of matter (Specific Heat, Nonmetallic Solids)*, Vol. 5 (New York - Washington: IFI/Plenum, 1970).
- [4] T. H. K. Barron, J. F. Collins, T. W. Smith *et al.*, *J. Phys. C: Solid State Phys.* **15**, 4311–4326 (1982).
- [5] D. R. Huffman and M. H. Norwood, *Phys. Rev.* **117**, 709–711 (1960).
- [6] G. A. Slack, *Phys. Rev.* **122**, 1451–1461 (1961).
- [7] Y. S. Touloukian, R. K. Kirby, R. E. Taylor *et al.* (eds.), *Thermophysical properties of matter (Thermal Expansion, Nonmetallic Solids)*, Vol. 13 (New York, NY: IFI/Plenum, 1977).
- [8] D. N. Batchelder and R. O. Simmons, *J. Chem. Phys.* **41**, 2324–2329 (1964).
- [9] S. S. Todd, *J. Am. Chem. Soc.* **71**, 4115–4116 (1949).
- [10] J. J. Hall, *Phys. Rev.* **161**, 756–761 (1967).
- [11] Y. S. Touloukian, R. W. Powell, C. Y. Ho *et al.* (eds.), *Thermophysical properties of matter (Thermal Conductivity, Metallic Elements and Alloys)*, Vol. 1 (New York - Washington: IFI/Plenum, 1970).
- [12] R. Hull (ed.), *Properties of crystalline silicon* (INSPEC, 1999).

Acknowledgements

First of all I would like to thank the Deutsche Forschungsgemeinschaft for their financial support, thus making our project 'Cryogenic Q-factor measurements of interferometer components' possible. My thanks also go to all people involved in the foundation of the Sonderforschungsbereich / Transregio 7 'Gravitational Wave Astronomy'. Without them, the project might not have existed in this form.

Further, I wish to thank Prof. Paul Seidel for giving me the opportunity to work on such an exciting research topic and his confidence in Ronny Nawrodt and me, giving us the opportunity to learn establishing and managing a project.

Special thanks go to Ronny Nawrodt, my team-mate. Since for one person alone the whole project work would have been unbearable, the present thesis would not have existed in this form without him. Also as a team-mate I could not have wished for anyone better. The close collaboration was that fruitful that the project which started from zero is now among the international established groups.

For the lively atmosphere I want to thank 'our' diploma students during the last year. I am grateful to Christian Schwarz for the good collaboration and communication concerning measurements and data analysis and his cheerful manner and especially to Daniel Heinert for soaking up every knowledge upon mechanical losses like a sponge and the following helpful discussions, besides being a good-humoured office-mate anytime.

For the nice atmosphere I thank all 'penguin' colleagues of the low temperature group. Especially, Matthias Thürk for his clever advices and support in touchy matter and Ralf Neubert for his patience in computer problems, particularly during the time of being every second day at Redlich's. Not at least the 'heart of the group', our secretary Sylvia Stender is named as a person to whom I am very thankful. Her friendly and caring manner always brought light into the days.

Many thanks go to the colleagues in the SFB / TR7 for the nice atmosphere at the project meetings. Especially to Prof. Gerhard Schäfer for his imperturbable friendly manner and the kindly introduction into gravitational wave detection.

For the good cooperation my thanks go to the people from Hannover, especially to the following persons. I am grateful to Joshua Smith for introducing us to the measurement of Q factors, the ever motivating meetings and the nice talks in the evening. To Prof. Roman Schnabel I am very obliged for the positive discussions and critical questions on mechanical losses and his pleasant serene and humorous manner. Further, I want to thank Alexander Bunkowski and Oliver Burmeister for the discussions on the

nice meetings and their lab survey. Many thanks go to Prof. Karsten Danzmann for his advice and his impressive thinking in “challenges”. I wish to thank Prof. Andreas Tünnermann representatively for the close cooperation with several people from the IAP and IOF. Many thanks go to the people from Glasgow, especially to Stuart Reid, Iain Martin, Prof. Sheila Rowan and Prof. Jim Hough. The exchange of knowledge and cooperation have been of great benefit for the Q factor measurements. I hope that the cooperation will continue and even will be extended in the future since the understanding of mechanical losses is such a comprehensive work that is best carried out by an international collaboration. I enjoyed their visits in Jena very much and even more our stay in Glasgow. Scottish humour is great! To Geppo Cagnoli from Glasgow / Italy I am very obliged - as an excellent scientist as well as a great person. I appreciate his extensive knowledge, his exceptional ideas and his talent to organize and keep the community together very much, which often is a thankless task. I am also very thankful that he introduced us to the STREGA community. I hope for an extension of the first contacts with his Italian group to a close cooperation in the future. For taking the time for discussions on phonons and defect induced mechanical losses I wish to thank Prof. Friedhelm Bechstedt.

For the nice contacts at the PHONONS 2007 conference I would like to thank Andreas Hüttel, Kurt Laßmann and Steven Hepplestone. Special thanks go to Astrid Netsch for the enjoyable meetings at several conferences and for always being helpful in any enquiries.

Many thanks go to Jürgen Kräußlich for the x-ray based measurements on a crystalline quartz sample. For the determination of the sodium ion concentration in the same material I thank Alexander Steppke very much.

During the literature research I became a regular customer of the physics library and lugged one book after the other into my office. For the guiding assistance in interlibrary lending I would like to thank Margrit Knorr. I am much obliged to Udo Tödter from the computer centre of the FSU Jena. I would never have hit on using an old kernel for operating the Linux workstation with the RAID 10. At this point it should be said that I am very glad about the existence of google as the Linux newbie that I have been had never bring the workstation into life without it. For her kind support in providing software and license files I thank Ilse Friede from the computer centre of the FSU Jena. Thanks go also to the workshops for their technical support.

To Matthias Büenfeld I am very grateful, since without him I would never have taken the opportunity of learning Spanish that soon. Finally, I thank him and all persons who made altruistic contributions to the welfare of the low temperature group and its social life.

Ehrenwörtliche Erklärung

Ich erkläre hiermit ehrenwörtlich, daß ich die vorliegende Arbeit selbständig, ohne unzulässige Hilfe Dritter und ohne Benutzung anderer als der angegebenen Hilfsmittel und Literatur angefertigt habe. Die aus anderen Quellen direkt oder indirekt übernommenen Daten und Konzepte sind unter Angabe der Quelle gekennzeichnet.

Weitere Personen waren an der inhaltlich-materiellen Erstellung der vorliegenden Arbeit nicht beteiligt. Insbesondere habe ich hierfür nicht die entgeltliche Hilfe von Vermittlungs- bzw. Beratungsdiensten (Promotionsberater oder andere Personen) in Anspruch genommen. Niemand hat von mir unmittelbar oder mittelbar geldwerte Leistungen für die Arbeiten erhalten, die im Zusammenhang mit dem Inhalt der vorgelegten Dissertation stehen.

Die Arbeit wurde bisher weder im In- noch im Ausland in gleicher oder ähnlicher Form einer anderen Prüfungsbehörde vorgelegt.

Die geltende Promotionsordnung der Physikalisch-Astronomischen Fakultät ist mir bekannt.

Ich versichere ehrenwörtlich, dass ich nach bestem Wissen die reine Wahrheit gesagt und nichts verschwiegen habe.

Anja Schröter

Lebenslauf

Name: Anja Schröter, geb. Zimmer

Geburtsdatum: 25.06.1976

Geburtsort: Berlin

Schule:

1983 - 1989 Grundschule: "Am Weinmeisterhorn" in Berlin

1989 - 1996 Gymnasium: "Herder-Oberschule" in Berlin

Juni 1996 Abitur

Studium:

WS 96 - SS 01 grundlagenorientiertes Physik-Studium an der TU-Berlin

WS 01 - WS 02 Physik-Studium an der Friedrich-Schiller-Universität Jena

März 2003 Diplom

Berufliche Tätigkeit:

seit März 2003 Wissenschaftliche Mitarbeiterin
am Institut für Festkörperphysik
der Friedrich-Schiller-Universität Jena

seit August 2003 Doktorandin ebenda

Anja Schröter